Electronic States of High-k Oxides in Gate Stack Structures

by

Chiyu Zhu

A Dissertation Presented in Partial Fulfillment
of the Requirements for the Degree
Doctor of Philosophy

Approved July 2012 by the
Graduate Supervisory Committee:

Robert Nemanich, Chair
Ralph Chamberlin
Tingyong Chen
Fernando Ponce
David Smith

ARIZONA STATE UNIVERSITY

August 2012

ABSTRACT

In this dissertation, *in-situ* X-ray and ultraviolet photoemission spectroscopy have been employed to study the interface chemistry and electronic structure of potential high-k gate stack materials. In these gate stack materials, HfO_2 and La_2O_3 are selected as high-k dielectrics, VO_2 and ZnO serve as potential channel layer materials. The gate stack structures have been prepared using a reactive electron beam system and a plasma enhanced atomic layer deposition system. Three interrelated issues represent the central themes of the research: 1) the interface band alignment, 2) candidate high-k materials, and 3) band bending, internal electric fields, and charge transfer. 1) The most highlighted issue is the band alignment of specific high-k structures. Band alignment relationships were deduced by analysis of XPS and UPS spectra for three different structures: a) $HfO_2/VO_2/SiO_2/Si$, b) HfO_2-$La_2O_3/ZnO/SiO_2/Si$, and c) HfO_2/VO_2/ $HfO_2/SiO_2/Si$. The valence band offset of HfO_2/VO_2, ZnO/SiO_2 and HfO_2/SiO_2 are determined to be 3.4 ± 0.1, 1.5 ± 0.1, and 0.7 ± 0.1 eV. The valence band offset between HfO_2-La_2O_3 and ZnO was almost negligible. Two band alignment models, the electron affinity model and the charge neutrality level model, are discussed. The results show the charge neutrality model is preferred to describe these structures. 2) High-k candidate materials were studied through comparison of pure Hf oxide, pure La oxide, and alloyed Hf-La oxide films. An issue with the application of pure HfO_2 is crystallization which may increase the leakage current in gate stack structures. An issue with the application of pure La_2O_3 is the presence of carbon contamination in the film. Our study shows that the alloyed Hf-La oxide films

exhibit an amorphous structure along with reduced carbon contamination. 3) Band bending and internal electric fields in the gate stack structure were observed by XPS and UPS and indicate the charge transfer during the growth and process. The oxygen plasma may induce excess oxygen species with negative charges, which could be removed by He plasma treatment. The final HfO_2 capping layer deposition may reduce the internal potential inside the structures. The band structure was approaching to a flat band condition.

DEDICATION

To the vacuum.

ACKNOWLEDGMENTS

First of all, I would like to express my gratitude to my advisor Dr. Robert Nemanich for his support and guidance through my Ph.D. study. His expertise in the physics and material science impressed me. He always gave me the best advice for my Ph.D. research. He is always available for discussions. His technical and editorial advice was essential to my papers and this dissertation. His dedication and enthusiasm in research are inspiring me for my future life.

I would like to thank all of my group members and my friends that helped me make my success in Ph.D. study. Especially, I am grateful to Franz Koeck who built up the whole lab, trained me for all systems and taught me all the knowledge about vacuum techniques. I appreciate Dr. Fu Tang's help very much for building up the ALD system and discussing with any research questions. Their guidance has lasted since I was a fresh Ph.D. student. I would like to extend my appreciation to Dr. Yang Sun, Dr. Gary Hembree for their supports and to all my colleagues Xin Liu, Tianying Sun, Brianna Eller, Jialing Yang and Manpuneet Kaur who help me with any questions I got. It is really a great experience to work with them.

I would like to thanks to all my committee professors, Dr. David Smith, especially for his expertise of TEM images, Dr Fernando Ponce, Dr.Ralph Chamberlin and Dr. Tingyong Chen for their assistance towards my Ph.D. degree.

Finally, I would like thank my parents for their understanding, support and love.

TABLE OF CONTENTS

Page

CHAPTER Page

CHAPTER Page

CHAPTER Page

LIST OF TABLES

Table Page

LIST OF FIGURES

Figure Page

Figure Page

Figure Page

Chapter 1

INTRODUCTION

1.1 CMOS scaling and leakage current

"The number of transistors incorporated in a chip will approximately double every 24 months." —Gordon E. Moore.[1] This is Moore's law, which was introduced in 1965. For decades, essentially, it described the pace of technology development for the semiconductor industry. For a planar technology, the dimension of a transistor will be scaled down by a factor of 0.7 every two years. While there have been many challenges met by fundamental and applied research, the most serious current problem is the FET 'gate stack' which includes the gate electrode and the dielectric layer on the silicon channel.

For a typical Metal Oxide Semiconductor Field Effect Transistor (MOSFET), the drive current is an important parameter, which determines the on/off status of the device. A high drive current means a fast switching time. The FET drive current I_D can be expressed with following equation:

$$I_D = \mu C_{ox} \frac{W}{L}((V_{GS} - V_{th})V_{DS} - \frac{V_{DS}^2}{2}), \quad (1.1)$$

where μ is the charge-carrier effective mobility, W is the gate width, L is the gate length and C_{ox} is the gate oxide capacitance, V_{GS} is the voltage applied between the transistor gate and source, V_{DS} is the voltage applied between the drain and source, and V_{th} is the threshold voltage. To obtain the necessary improved performance, the C_{ox} must be increased.

The MOSFET can be treated as a parallel plate capacitor, and the capacitance can be given as: $C_{ox} = \frac{k\varepsilon_0 A}{t_{ox}}$, (1.2)

Where k is the relative dielectric constant (relative permittivity), ε_0 is the permittivity of free space (8.85 × 10-12 F/m), A is the area of the capacitor plate and t_{ox} the thickness of the dielectric, which usually is an oxide. According to the equation, there are three ways to obtain a higher capacitance: 1) increase the area A, 2) decrease the thickness of oxide layer t_{ox}, and 3) increase the dielectric constant k. However, since the transistor size is scaled down in each future generation, the area A is always decreasing, which results in a decreased capacitance. To maintain the required capacitance, the thickness of dielectric oxide t_{ox} has been reduced in past generations. Nowdays, as the thickness of oxide is at the nanometer scale, the leakage current due to the quantum tunneling effect has become large. The tunneling possibility T for a single particle:

$$T \propto \exp(-2\int_{x1}^{x2} dx\sqrt{\frac{2m(V(x)-E)}{\hbar^2}}) , (1.3)$$

Where V(x) is the barrier height due to the oxide layer, E is the carrier energy, x1 and x2 are the oxide layer position, and for simplicity, V(x) is considered as a constant. Then rewriting Eq. 1.3:

$$T \propto \exp(-2Ct_{ox}) , (1.4)$$

Where $C = \sqrt{2m(V-E)/\hbar^2}$ is constant, and t_{ox} is the thickness of the oxide. As indicated in the equation, the tunneling leakage current increases exponentially as the oxide thickness is reduced. As, the thickness of SiO_2 is reduced to below 2

nanometers, the gate leakage current due to electrons tunneling electrons the SiO_2 layer has become large. Consequently, the power dissipation increases to unacceptable values [2-4]. Therefore, reducing the thickness of the oxide (SiO_2) is no longer an option for future technology. An alternate approach is to replace SiO_2 with other oxides that have a higher dielectric constant than the SiO_2 which is 3.9. These oxides are called high-κ dielectrics.

1.2 High-k dielectrics

Silicon dioxide is the crucial material that enabled adoption of Si as the basic material in the semiconductor industry. Some of the advantages of SiO_2 include: it is a very good insulator; it can be prepared by the thermal oxidation of Si; it is amorphous with few defects; and it is compatible with Si with a low interface state density. However, the major issue is the tunneling leakage current has exceeded allowed values for the very thin SiO_2 which has a dielectric constant of 3.9. Consequently, it is necessary to find a new material to replace SiO_2 as a gate dielectric. Generally, the materials which are typically metal oxides, with a dielectric constant higher than the 3.9 value of SiO_2, are termed high-k materials.

The requirements for candidate oxide as high-k materials include:

1. The dielectric constant (k value) is the key parameter, which must be high enough to accommodate years of the scaling down the transistor dimensions.

2. The material is a good insulator with a large band gap. It has a reasonable band offsets with Si which can confine the electrons and holes inside the channel layer and prevent carrier injection into its own bands.

3. It has a smooth interface with Si, with a low density of interface states.

4. It is thermally compatible with required high temperature processes.

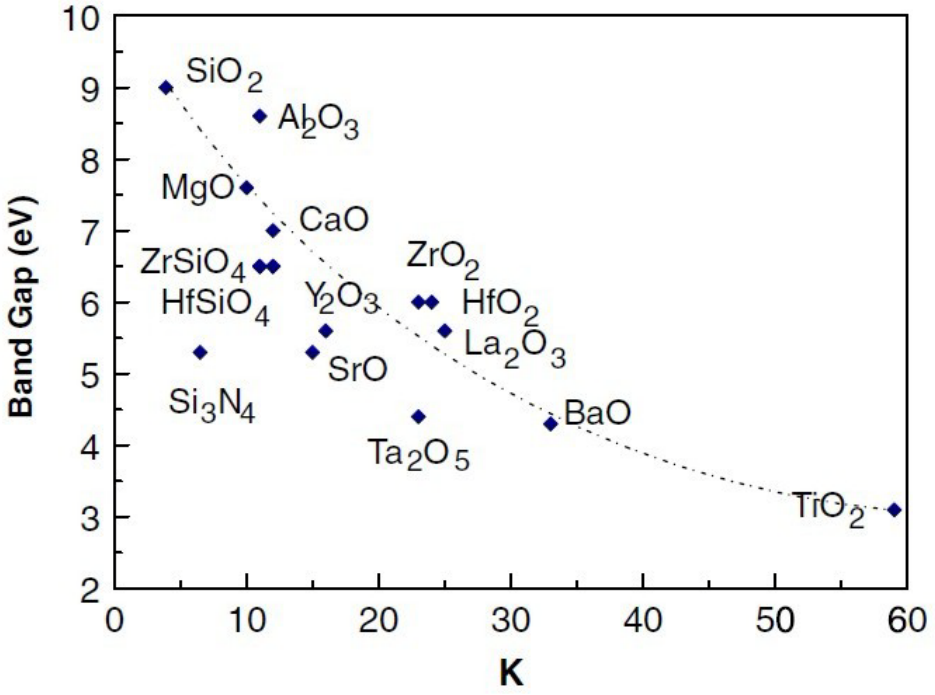

Figure 1.1. Dielectric constant versus band gap for candidate gate oxides [5]

Figure 1.1 shows the band gap and dielectric constant of several candidate high-k dielectric materials [5]. As indicated in the figure, the candidate materials with a higher k value, tend to exhibit a lower band gap. If the band gap is too low, the band offset of this material with Si will be small. Table 1.1 lists candidate high-k oxide materials and their reported conduction band offset on Si, their band gap and k values. The conduction band offset is required to be more than 1 eV, otherwise the electrons within the channel layer can tunnel through the gate dielectric resulting in a large leakage current. For example TiO_2, has a high k value of ~ 100, but it is still not a good candidate as the band gap of TiO_2 is low and the conduction band offset is almost zero to Si. Considering the balance

between relative high k value and acceptable band gap, the preferred high-k oxide candidates have a k-value between 20-30. So ZrO_2 HfO_2 and La_2O_3 are the most studied candidates. In addition, Al_2O_3 with a high band gap, and good insulating property, though it has lower k value of 9.

Table 1.1. Dielectric constant (k), experimental band gap and conduction band (CB) offset on Si of gate dielectics candidates. [6]

	K	Band Gap (eV)	CB Offset (eV)
Si		1.1	
SiO_2	3.9	9	3.2
Al_2O_3	9	8.8	2.8
Ta_2O_5	22	4.4	0.35
TiO_2	80	3.5	0
$SrTiO_3$	2000	3.2	0
ZrO_2	25	5.8	1.5
HfO_2	25	5.8	1.4
$HfSiO_4$	11	6.5	1.8
La_2O_3	30	6	2.3
a-$LaAlO_3$	30	5.6	1.8

ZrO_2 and HfO_2 have similar properties as they are in the same column of the periodic table. However, HfO_2 is preferred as more stable since ZrO_2 may form a silicide Zr_2Si during high temperature processes [7-10]. La_2O_3 another candidate material, has a slightly higher k value than HfO_2, but La_2O_3 absorbs water and carbon dioxide when exposed to air, which forms LaO(OH) and carbonate structures. [11-13] It has been reported that HfO_2 may form crystalline domains which can lead to rough surfaces and electrical leakage. These problems have been addressed by alloying other glass forming oxides, like SiO_2. Our results

reported that HfO_2 alloyed with La_2O_3 may solve this crystallization problem. [14]

1.3 Oxide channel layer material

Today, single crystalline semiconductor materials such as Si, GaAs and GaN and semiconductor related oxides like SiO_2, dominate the electronic industry. Some oxides such as indium tin oxide (ITO) have wide application as conducting oxides. In the future, oxides may have increased applications. In our study, we will discuss two oxides for future applications. One is zinc oxide (ZnO), which may have potential application in thin film transistors for displays. The other is vanadium oxide (VO_2), which may have future application in switching or memory devices.

1.3.1 Zinc oxide

ZnO is a semiconductor material with a direct band gap of 3.4 eV at room temperature [15]. Compared to hydrogenated amorphous silicon (a-Si:H) which is the active channel layer material of conventional thin film transistors (TFTs) with a low mobility of less than 1.0 cm^2/Vs [16], ZnO has a room temperature mobility of ~100 $cm^2/V{\cdot}s$ [17]. As-grown, undoped, ZnO films typically exhibit n-type semiconductor characteristics with an electron concentration from 10^{17} to 10^{21} cm^{-3}. [18, 19] This high carrier concentration has been attributed to defects such as zinc interstitials or oxygen vacancies. [20, 21] ZnO, as a transparent conducting semiconductor material, has been proposed for the channel layer of transparent thin film transistors (TFTs) for flexible transparent display.

TFT's in flexible transparent displays require a process temperature of less than 180 °C, and plasma enhanced atomic layer deposition (PEALD) has been considered to achieve a ZnO deposition temperature in the range of 25~120 °C. High mobility zinc oxide thin films have been successfully grown by thermal ALD at temperatures ranging from 200 to 350 °C. [22-24]. Recently, low temperature (100~200 °C) thermal ALD growth of ZnO has also reported. [25] Diethyl zinc (DEZn) and dimethyl zinc (DMZn) have been employed as precursors for this process, and PEALD ZnO thin films have exhibited mobilities of 1.0 to 6.0 $cm^2/V{\cdot}s$ [26, 27]. In PEALD, the activated oxygen species generated by the plasma can significantly reduce the deposition temperature and produce a denser film with a potentially lower defect concentration. In order to minimize the effects of defects and excess species, studies up to now have focused on high temperature deposition or post deposition annealing. [28-30] However, both are high temperature processes , which do not meet the low temperature processing requirement for flexible substrates. Thus, incorporation of ZnO into a TFT process, requires and approach that has a low deposition temperature and low defect density along with identification of dielectric layers to confine carriers in the channel.

1.3.2 Vanadium dioxide

Vanadium dioxide (VO_2) is a narrow band gap material (Eg = 0.7eV) [31], with a well known Metal to Insulator Transition (MIT) property. This MIT transition can be affect by temperature, [31,32] strain[33] and electric field. [34-38] The insulator to metal transition temperature for VO_2 is ~70°C (343K),

[31,32] with an abrupt three order magnitude change of resistivity. Figure 1.2 shows the resistance vs temperature transition hysteresis during heating and cooling. The other two common vanadium oxides, V_2O_3 and V_2O_5, show IMT at 160K [39] and 530K, respectively [40]. This transition temperature can be affected by the strain on the VO_2 and substrate. Some studies of VO_2 on TiO_2 show that the transition temperature can be as low as 300K due to strains. [33] Recently, it has been found that the MIT transition can be achieved by applying an external electric field at a constant temperature. [34-38] Figure 1.3 shows the I-V curve of a VO_2 film under the effect of an external electric field. The results indicate a critical electric field for MIT transition of ~10^7 V/m. The large resistivity change and the abrupt MIT of VO_2, makes it a strong candidate for a variety of optical and electrical switching applications. [41,42]

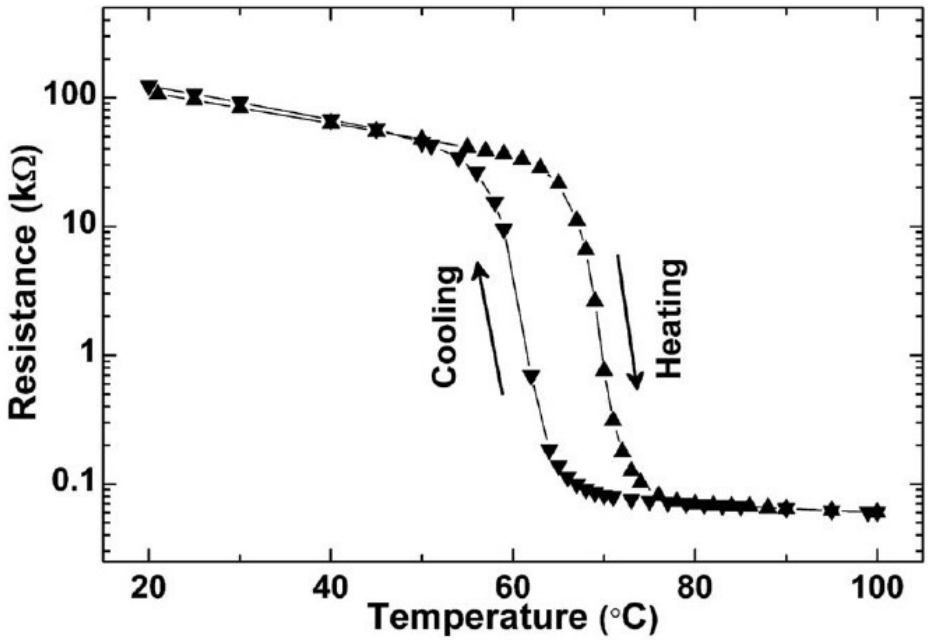

Figure 1.2. Resistance vs Temperature for a VO_2 film showing the abrupt change in resistance and thermally induced phase transition. [37]

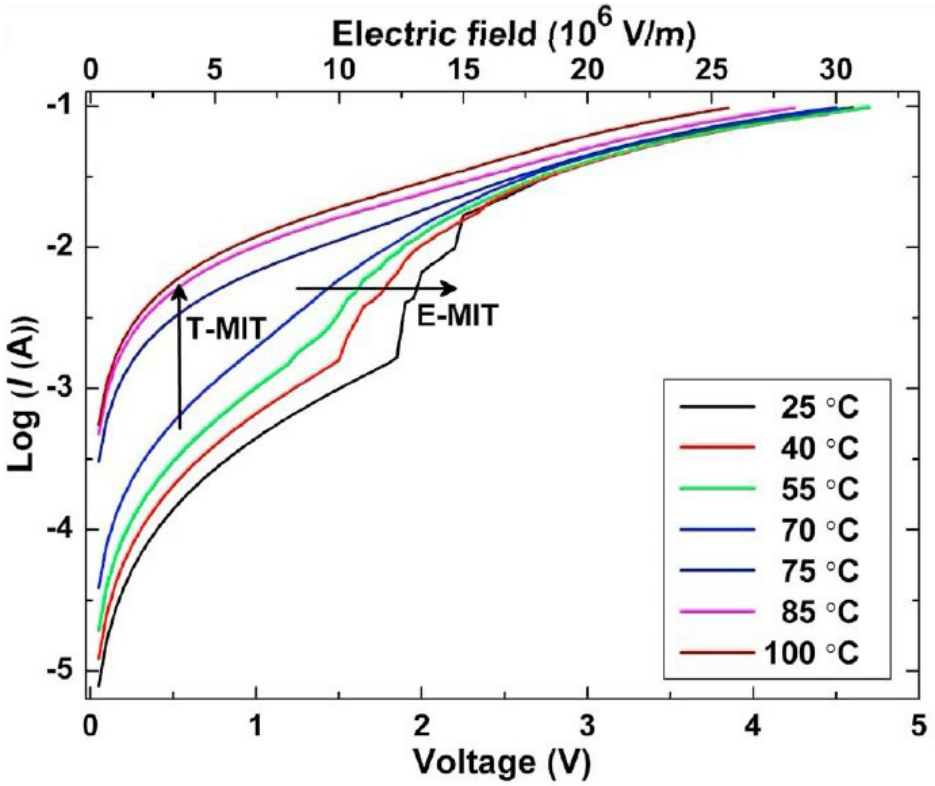

Figure 1.3. log(I) vs V curves for a VO_2 film at particular temperatures. [37]

The mechanism of this MIT has been the subject of numerous papers and is still under debate. Researchers have proposed two explanations for the MIT transition. The thermally induced MIT has been explained by a structure phase transition. When VO_2 is heated from low to high temperature through the MIT temperature, the VO_2 crystal structure changes from the insulating monoclinic phase to the metallic tetragonal phase. The results indicated that the MIT is attributed to the structure phase transition. [32, 33] More recently, as the electric field assisted MIT has been studied, it has been argued that the Mott transition

may be the main reason for this MIT. [35-38, 42] Other researchers have presented calculations which suggested that Joule heating can not be the main reason for MIT. [38] This Mott transition hypothesis argues that when the carrier density in VO_2 is beyond a critical value a Mott transition occurs independent of a structural change. The Mott transition would occur at a critical electron concentration given by $(N_C)^{1/3}\ \alpha_H \sim 0.25$ where, N_C is the critical carrier density and α_H is the Bohr radius.[41] The results indicate a critical electric field of $\sim 10^7$ V/m and a critical density of $\sim 10^{19}$ cm^{-3}.

However, device structures with VO_2 will require integration with high-k material which has not beed studied to date. In our study, we investigate a gate stack structure of VO_2 with HfO_2, and understand the band relationship of this new structure.

1.4 Band alignment

In a CMOS structure, the oxide layer, which is usually SiO_2, is the insulating layer between channel layer and gate electrode. In our studies the semiconductor Si served as the channel layer. Transition metal oxides with high dielectric constant are investigated for the insulator layer. In this study HfO_2 or HfO_2-La_2O_3 alloyed oxide with reasonable dielectric constant ~ 20 were explored as possible dielectric materials. Also for the channel layer, we are proposing VO_2 and ZnO as channel layer materials for future application of oxide devices, such as switching and memory storage. One of the most important characteristics of any new gate stack structure is the barrier height (band offset) between the high-k insulator layer and the new oxide channel layer. The band offset is required to be

high enough to block the carriers (electrons or holes) in the transistor channel. The band alignment of these oxides layers with Si substrate need to be determined.

Currently, two models are often considered to describe the interface band alignment of oxide and semiconductor. One is the electron affinity (EA) model, which originated from the Schottky-Mott model that describes the barrier between a metal and a semiconductor. When a metal and a semiconductor are in contact, the *n-type* Schottyky barrier (Φ_b) is described as follows:

$\Phi_b = \Phi_M - \chi$, (1.5)

Where the Φ_M is the work function of the metal and χ is the electron affinity of the semiconductor. In the case of higher the work function than semiconductor electron affinity, as shown in Fig. 1.4, electrons from the semiconductor side will flow into the metal side, and align the Fermi level with the metal. This will leave a depletion layer inside the semiconductor near the interface. Consequenty, the vacuum levels of the metal and semiconductor are aligned. When applied to the insulator and semiconductor interface, this model has been termed as the electron affinity (EA) model. In the EA model, the Fermi level and vacuum levels are aligned at the interface of the insulator and the semiconductor.

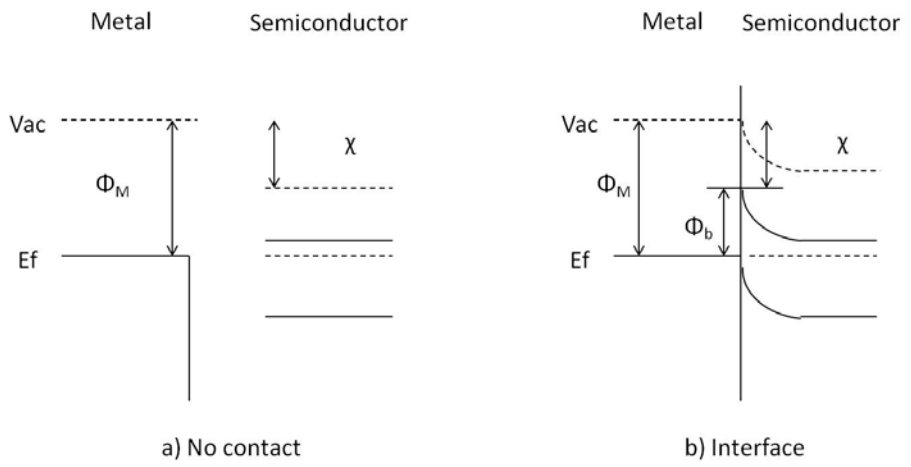

Figure 1.4 Schematic illustration of an *n*-type Schottky barrier. a) metal and semiconductor are separated. b) Metal and semiconductor are in contact. A Schottky barrier is formed.

The Schottky-Mott model is successful in the metal semiconductor systems where thet two vacuum levels at the interface are well aligned. However, when the vacuum levels are not aligned, which means an interface dipole is present at the interface, the Schottky model is not an accurate description. A model has been proposed by Bardeen and Heine that when dealing with surface or interface, localized states are present in the band gap [43, 44] These states could be called as “metal-induced gap states” (MIGS). [45] These virtual states could be thought as the dangling band state dispersed into the semiconductor band gap or the metal wave functions decaying exponentially into the semiconductor band gap. These states are derived from conduction or valence band states. The cross-over point or branch point represents the charge neutrality point for the semiconductor. This branch-point energy has been termed the charge neutrality level (CNL). Consequently, the Fermi level at the interface is pinned near the

charge neutrality level. These charge neutrality levels have been calculated for Si, Ge some III-V and II-VI compound by Tersoff [45]. J. Robertson also applied this model to calculate the CNL for oxides [5] and Mönch calculated the CNLs for diamond, zincblende and wurzite structured semiconductors [46].

The band alignment between two semiconductors (a and b) depends on the interface dipoles [47, 48]. The band alignment is described as matching the CNLs and also modified by an S factor, as shown as below:

$\Phi_n = (\chi_a - \Phi_{CNL,a}) - (\chi_b - \Phi_{CNL,b}) + S(\Phi_{CNL,a} - \Phi_{CNL,b})$, (1.6)

Where Φ_n is the conduction band offset, χ and $\Phi_{CNL,}$ are the electron affinity values and CNLs of semiconductor a and b. S is the Fermi level pinning factor. Mönch found an empirical equation to determine the S value [49], where ε_∞ is the dielectric constant.

$$S = \frac{1}{1 + 0.1(\varepsilon_\infty - 1)^2}, \quad (1.7)$$

a) When S = 1, substitution into Eq. 1.6, the CNLs canceled each other. The band offset is the difference of the electron affinities of the two materials, which is described by the EA model.

b) When S = 0, the Fermi levels are pinned at the CNLs. In the band alignment the CNLs are well aligned. This is the CNL model.

In our study, the band alignment relationships are experimentally determined for these new gate stack structures. The two band alignment models are then considered to characterize the nature of the electronic states at the interface.

1.5 Thesis approach

The gate stack structures are becoming more complicated for today's and future electronic applications. High-k materials are widely employed as insulator dielectrics. Also new channel layer materials are being investigated to replace the traditional channel layer materials. In this thesis, we focus on gate stack structures with high-k dielectrics and new oxide channel materials, with a particular focus on the interface electronic structure.

In chapter 2, essential information about the instruments is introduced, including: a) growth equipment, oxide molecular beam deposition (MBD) and plasma enhanced atomic layer deposition (PEALD); b) characterization equipments, X-ray photoelectron spectroscopy (XPS) and ultraviolet photoelectron spectroscopy (UPS). The band alignment analysis method is also described.

In chapter 3, a gate stack structure has been prepared with a HfO_2 capping layer and an ultra thin VO_2 interlayer on oxidized Si substrates. The 2nm thick films of each layer were grown by oxide molecular beam deposition on oxidized *n*- and *p*-type substrates. This chapter addresses two issues: 1) development of a high quality gate stack structure with high-k dielectrics and an oxide channel material; 2) the determined the band set off of HfO_2/VO_2 and the interface charges in the processing. TEM analysis confirmed the layer structure and indicated sharp interfaces without evidence of interdiffusion. From the *in-situ* XPS and UPS spectra, the valence band offset between the HfO_2 and VO_2 is measured to be 3.4 ± 0.1 eV. The interfacial charge transfer during the processing

are discussed. The band alignment for this gate stack structure was deduced. We propose that the charge neutrality level model describes this gate stack structure.

In Chapter 4, the focus is on the candidates high-k materials. In this chapter, three high-k materials, pure Hf oxide, pure La oxide, and alloyed Hf-La oxide films were prepared by using remote plasma enhanced atomic layer deposition (PEALD). The relative composition and atomic bonding structure of the films were determined by *in-situ* X-ray photoelectron spectroscopy (XPS). Atomic force microscopy (AFM) and transmission electron microscopy (TEM) were implemented to characterize the morphology and crystalline structure. The main issue of the HfO_2 is the formation of nanocrystalline domains in the film which may increase the leakage current. Our result show that alloyed Hf-La oxide has an amorphous structure with a smooth surface. This alloyed oxide could be an alternative for pure HfO_2 as a possible candidate of high-k dielectrics. We also observed that the oxygen plasma treatment may induce excess oxygen species in the deposited film. This excess oxygen species could be partially removed by a He plasma treatment.

In chapter 5, we extend our study to new channel layer material ZnO which has a relatively high mobility and combine it with our previous study of alloyed Hf-La oxide. ZnO is adopted as a channel layer material and integrated into a gate stack structure with an alloyed HfO_2-La_2O_3 (11% HfO_2 and 89% La_2O_3) layer, which are both grown by PEALD. The band alignment of this structure was established for an *n*-type Si substrate, based on characterization of *in-situ* x-ray and ultraviolet photoemission spectroscopy. A valence band offset of

1.5 ± 0.1 eV was measured between a thin ZnO layer and a SiO_2 layer. The valence band offset between HfO_2-La_2O_3 and ZnO was almost negligible. High resolution electron microscopy indicated an amorphous structure of the deposited layers. A significant amount of excess oxygen was also observed in the as-deposited ZnO and (HfO_2-La_2O_3) layers. A helium plasma post-deposition treatment can partially remove the excess oxygen in both layers. Our results demonstrate confinement of electrons in the ZnO film as a channel layer for thin film transistors.

In chapter 6, we modified the gate stack structure into a quantum well structure. This quantum well structure is prepared as an ultra thin VO2 layer between two layers of HfO2. The band alignment relationship is studied by analysis of in-situ XPS and UPS. The band offset between the HfO_2 and VO_2 is 3.4 ± 0.1 eV, which is consistent with our previous result. A band offset of the HfO_2 layer and the SiO_2 layer was measured as 0.7 ± 0.1 eV, which is comparable to the value predicted by CNL model. The results demonstrate this well structure could contain both electrons and holes, and may have potential applications for charge storage in the embedded VO_2 layer.

In chapter 7, the most important results of this dissertation are summarized, and future studies based on current work are proposed.

.

REFERRENCES

[1] Gorden E. Moore, Electronics, Vol. 38, No. 8, April 19, (1965).

[2] Wilk G, Wallace R M, Anthony J M, J. Appl. Phys. 89, 5243 (2001).

[3] Wallace R M and Wilk G D, Crit. Rev. Solid State Mater. Sci. 28, 231 (2003).

[4] Robertson J, Eur. Phys. J. Appl. Phys. 28, 265 (2004).

[5] Robertson J, J. Vac. Sci. Technol. B, 18, 1785 (2000).

[6] Robertson J,Rep. Prog. Phys. 69, 327–396 (2006).

[7] Copel M, Gribelyuk M and Gusev E, Appl. Phys. Lett. 76, 436 (2000).

[8] J. P. Chang and Y.S. Lin, Appl. Phys. Lett., Vol. 79, No. 23, 3 December (2001).

[9] Y.S. Lin, R. Puthenkovilakam, and J. P. Chang, Appl. Phys. Lett., Vol. 81, No. 11, 9 September (2002).

[10] M. C. Zeman, C. C. Fulton, G. Lucovsky, and R. J. Nemanich and W.C. Yang, J. Appl. Phys. 99, 023519 (2006).

[11] M. Suzuki, M. Kagawa, Y. Syono and T. Hirai., J. Cryst. Growth, 112, 621 (1991).

[12] A.M. De Asha, J.T.S. Critchley, R.M. Nix, Surface Science 405, 201–214 (1998).

[13] M. Nieminen, M. Putkonen, and L. Niinisto, Appl. Surf. Sci. 174, 155 (2001).

[14] Fu Tang, Chiyu Zhu, David J. Smith, and Robert J. Nemanich, J. Vac. Sci. Technol. A, Vol. 30, No. 1, Jan/Feb (2012).

[15] Mang A, Reimann K and Rubenacke St, Solid State Commun. 94, 251 (1995).

[16] K. Nomura, H. Ohta, A. Takagi, T. Kamiya, M. Hirano, and H. Hosono, Nature, Vol 432, 488 (2004).

[17] E. Guziewicz, M. Godlewski, T. Krajewski, Ł. Wachnicki, A. Szczepanik, K. Kopalko, A. Wójcik-Głodowska, E. Przeździecka, W. Paszkowicz, E.

Łusakowska, P. Kruszewski, N. Huby, G. Tallarida, and S. Ferrari, J. Appl. Phys. 105, 122413 (2009).

[18] S. Keun Kim, C. H. Hwang, S. H. Ko Park, and S. J. Yun, Thin Solid Films 478, 103 (2005).

[19] S. H. Ko Park, C. S. Hwang, H. S. Kwack, J. H. Lee, and H. Y. Chu, Electrochem. Solid-State Lett. 9, G299 (2006).

[20] K.G. Saw, K. Ibrahim, Y.T. Lim, M.K. Chai, Thin Solid Films 515, 2879 (2007).

[21] G. Neumann, Curr. Top. Mater. Sci. 7, 143 (1981).

[22] A. Wójcik, M. Godlewski, E. Guziewicz, R. Minikayev, and W. Paszkowicz, J. Cryst. Growth 310, 284 (2008).

[23] Vesa Lujala, Jarmo Skarp, Markku Tammenmaa, Tuomo Suntola, Appl. Surf. Sci. 82/38, 34 (1994).

[24] S.J. Lim, Soonju Kwon, H. Kim, Thin Solid Films, 516, 1523 (2008).

[25] E. Guziewicz, I. A. Kowalik, M. Godlewski, K. Kopalko, V. Osinniy, A. Wójcik, S. Yatsunenko, E. Łusakowska, W. Paszkowicz, and M. Guziewicz, J. Appl. Phys. 103, 033515 (2008).

[26] Y. Kawamura, N. Hattori, N. Miyatake, M. Horita, and Y. Uraoka, Jpn. J. Appl. Phys. 50, 04DF05 (2011).

[27] P.C. Rowlette, C.G. Allen, O.B. Bromley, Amy E. Dubetz, and C. A. Wolden, Chem. Vap. Deposition, 15, 15–20 (2009).

[28] P. K. Park, J. S. Roh, B. H. Choi, and S. W. Kang, Electrochem. Solid-State Lett. 9, F34 (2006).

[29] J. S. Park, H. S. Park, and S. W. Kang, J. Electrochem. Soc. 149, C28 (2002).

[30] Y. Won, S. Park, J. Koo, S. Kim, J. Kim, and H. Jeon, Appl. Phys. Lett. 87, 262901 (2005).

[31] C. N. Berglund and H.J. Guggenheim, Phys. Rev. 185, 1022-1033 (1969).

[32] F.J. Morin, Phys. Rev. Lett. 3, 34-36 (1959).

[33] K. Nagashima, T. Yanagida, H. Tanaka, and T. Kawai, J. Appl. Phys. 101, Art Number 026103-3 (2007)

[34] H-T. Kim, B.-G Chae, D.-H. Youn, G. Kim, and K.-Y. Kang, Appl. Phys. Lett. 86, 242101-3 (2005).

[35] H-T. Kim, Y.-W. Lee, B.-J. Kim B.-G Chae, S.-J. Yun, K.-Y. Kang, K.-J. Han K.-J. Yee, and Y.-S. Lim, Phys. Rev. Lett. 97, 266401-4 (2006).

[36] C. Ko and S. Ramanathan, Appl. Phys. Lett. 93, Art Number 252101-3 (2008).

[37] G. Stefanovich, A. Pergament, D. Stefanovich, J. Phys.: Condens. Matter 12, 8837-45 (2000).

[38] G. Gopalakrishnan, D. Ruzmetov, S. Ramanathan, J. Mater. Sci. 44, 5345-53 (2009).

[39] Koji Kousge, J. Phys. Chem. Solids Pergamon Press, Vol. 28, pp. 1613-1621 (1967).

[40] G.S. Nadkarni and V.S. Shirodkar, Thin Solid Films, 105,115-129 (1983).

[41] S. Hormoz, S. Ramanathan, Solid-State Electronics 54, 654-659 (2010).

[42] A.L. Pergament, P.P. Boriskov, A.A. Velichko, N.A. Kuldin, J. Phys. Chem. Solids 71, 874-879(2010).

[43] J. Bardeen, Phys.Rev. 71, 717 (1947).

[44] V. Heine, Phys. Rev. 138A, 1689 (1965).

[45] J. Tersoff, Phys. Rev. Lett. 52, 465 (1984).

[46] W. Mönch, J. Appl. Phys. 80, 5076 (1996).

[47] J. Tersoff, Phys. Rev. B 30, 4874 (1984).

[48] J. Tersoff, Phys. Rev. B 32, 6968 (1985).

[49] W. Mönch, Phys. Rev. Lett. 58, 1260 (1986).

Chapter 2

INSTRUMENTS AND ANALYSIS METHOD

2.1 Introduction

The experiments are mainly accomplished *in-situ* using an integrated ultrahigh vacuum (UHV) system, as shown in Fig. 2.1, with other *ex-situ* facilities and equipments.

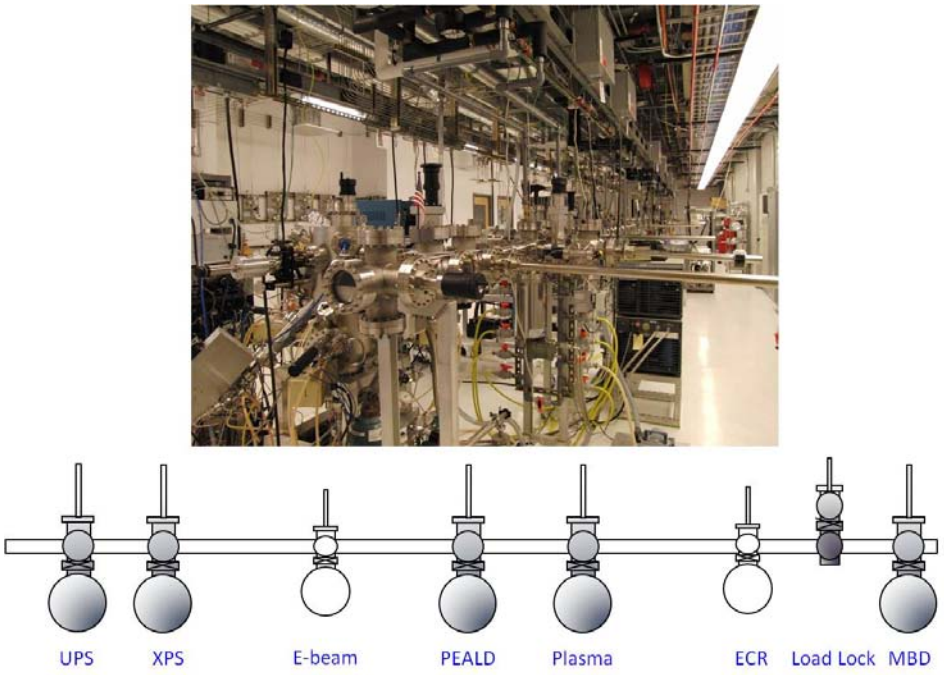

Figure 2.1 Actual view and schematic illustration of the transfer line with integrated ultrahigh vacuum (UHV) systems.

This integrated UHV system involves a linear ~20 m UHV transfer line chamber that connects different processes and characterization chambers. The UHV transfer line can reach the base pressure of 5×10^{-10} Torr with 5 cryogenic pumps. The sample can be loaded into a loadlock chamber connecting to the transfer line. In this study, the following systems are employed, reactive

molecular electron beam deposition system (MBD) for oxide growth, remote oxygen plasma enhanced atomic layer deposition system (PEALD) which also serves as a remote oxygen plasma system for surface cleaning, remoted plasma system with H_2, N_2, He and Ar plasma processes, X-ray photoelectron spectroscopy (XPS) for core level analysis, and ultraviolet photoelectron spectroscopy (UPS) for valence band spectra.

The other *ex-situ* facilities and equipment include: chemical cleaning in a cleaning room, typically, an acetone and methanol sonicating cleaning of wafers. An Agilent 5500 AFM was used to characterize the morphology of the deposited films. A JEOL JEM 4000EX high-resolution electron microscope, operated by Dr. David Smith, to observe cross-section image of representative samples. The electrical properties of the oxide films were investigated by capacitance voltage (C-V) and current voltage (I-V) measurements.

2.2 Molecular Electron Deposition (MBD) for oxide growth

2.2.1 Overview of MBD

The MBD system is based on an electron beam deposition source with an oxygen gas delivery system, as shown in Fig. 2.2. The system is pumped by a 10 inch flange size cryopump and a turbo-molecular drag pump. The base pressure can reach ~ of 6×10^{-9} Torr after baking. Three independent electron beam sources are installed with three different metals: hafnium, titanium and vanadium. This system is employed to deposit metal oxide films.

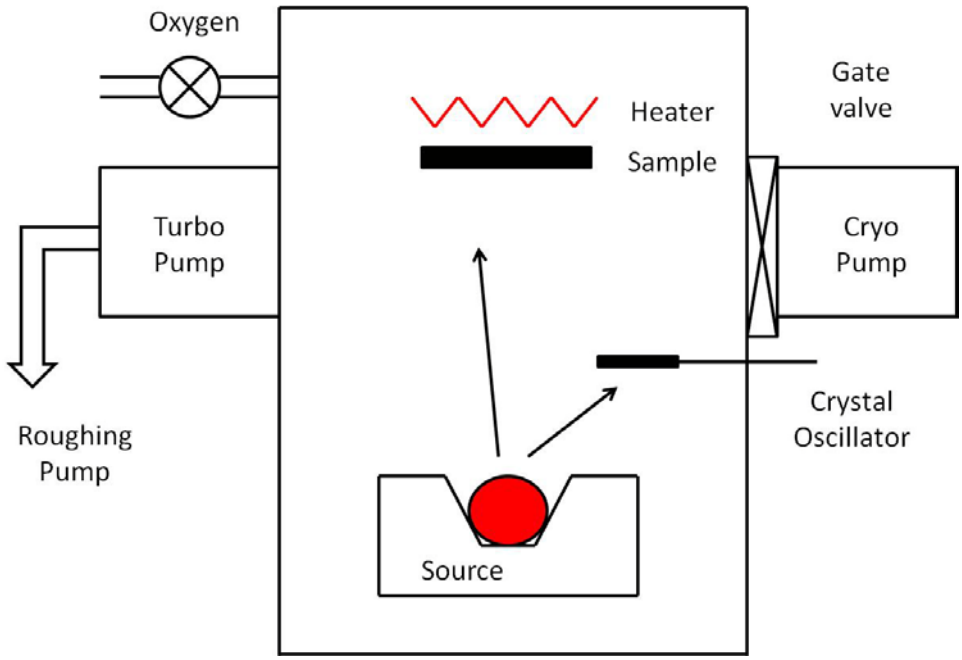

Figure 2.2 Schematic illustration of molecular electron deposition (MBD) system.

2.2.2 Electron beam deposition source

The electron beam deposition source installed on the MBD system was obtained from MDC and is operated with an MDC e-Vap CVS emission current source controller and a MDC e-Vap CVS 10, 10kW power supply. A typical electron gun includes two parts: an electron emitter and the source, shown in Fig. 2.3. A current (filament current) passing through the emitter filament, generates the electron beam (emission current) by the thermionic emission effect. The electron beam is accelerated by an electric field and confined by a magnetic field to focus on the center of the source. The emission current, which can be adjusted by the filament current, is typically 50 ~ 300 mA. The electron beam position can be adjusted by the high voltage applied between the filament and the source or the magnetic field across the source. The high energy electron beam strikes the source

and heats the metal source to the vaporization temperature. Usually, the local temperature of the focused spot is above the melting point of the source. Beyond the critical temperature, the metal source at the hot spot starts to evaporate. The growth rate which is measured by a crystal thickness monitor can be controlled by adjusting the emission current.

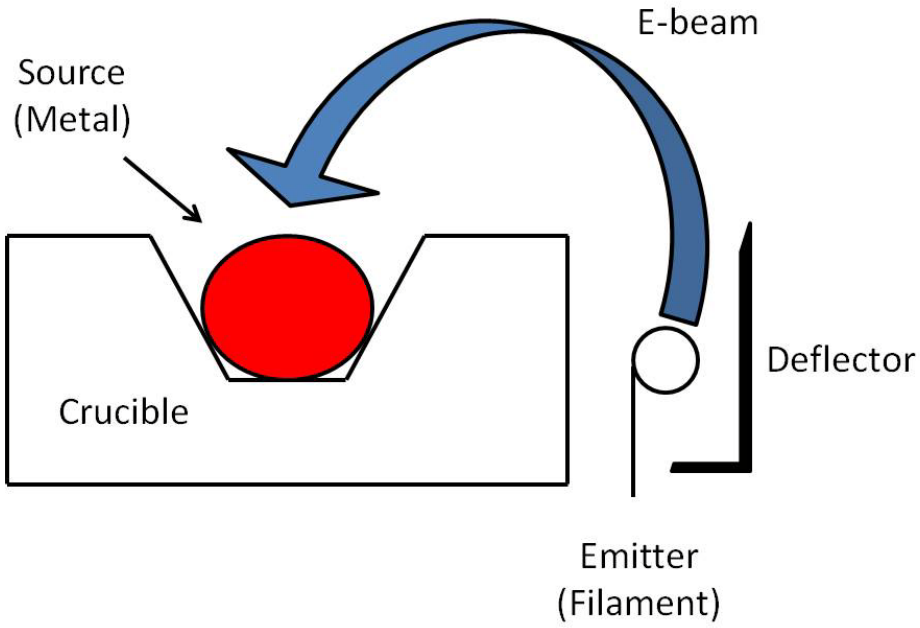

Figure 2.3 Schematic illustration of the electron beam source used for molecular beam deposition (MBD) system. The electron emitter and deposition source are shown and the electron beam path is marked in blue.

2.2.3 Oxide growth procedure

After loading the substrate into the chamber, high voltage (HV) is applied between the filament and the selected metal source. Typically, the HV is 6.5 kV for the hafnium oxide growth and 5.0 kV for vanadium oxide growth. Then the emission current is increased to the critical point when deposition is measured on

the crystal oscillator monitor. Typical deposition rates are ~0.01 nm/s. Before oxide deposition, the gate valve to the cryopump is closed, and the chamber is only pumped by the turbo-molecular pump. The oxygen inlet valve is then opened, and high purity oxygen (research grade) gas is delivered into the chamber. The oxygen pressure during the growth is 2.0×10^{-6} Torr for the hafnium oxide growth and 6×10^{-4} Torr for vanadium oxide growth, respectively. Even though the oxygen flow rate is maintained at a constant value, the oxygen pressure decreases during the growth apparently due to reaction with species deposited on the chamber walls. The oxygen flow is adjusted to keep the pressure constant.

2.2.4 Growth of vanadium oxide

As vanadium oxide is grown under relatively high oxygen pressure ~ 6×10^{-4} Torr, problems may occur due to the high oxygen pressure.

One problem for vanadium oxide growth, is electric arcing occurs at the electron beam source. During growth, kilovolts potential is applied between the emitter and the metal source. The emitter is at a high negative potential, and other parts are grounded. The smallest gap between the negative high voltage emitter and grounded parts are around 3-4 mm. If the chamber pressure is less than 1×10^{-4} Torr then arcing is not detected. However, if the chamber pressure is increased to mTorr range, since this is the case for vanadium oxide growth condition, arcing was often detected. Approaches often considered to avoid this arcing problem include: 1) Reducing the value of the high voltage. However,

when the high voltage is changed, the beam spot on the source also changes. The magnetic field can be adjusted to move the beam spot back to the center of the source. 2) The gas molecules around the e-gun parts are desorbed since the emitter is hottest part of the average chamber. The local pressure is considerably higher than the whole chamber pressure. Furthermore, oxides may condense around the emitter and decompose or evaporate due to the high temperature. To avoid these problems, the e-gun can be turned on and the emission current increased for 15 min prior to deposition. This pre-deposition heating has been adopted to out gas the emitter which may help to reduce this local high pressure effect.

Another problem is concerned with the emitter filament lifetime. The emitter filament is made of tungsten wire. Usually, the tungsten filaments can work for years in high vacuum conditions. However, if the deposition occurs with a relatively high oxygen pressure environment, the filament is degraded due to oxidation and evaporation of the oxide. This is evident when a degraded filament is replaced, and the aged filament is much thinner than the new one. The tungsten oxide can evaporate and deposit around the emitter parts, and contribute to the local high pressure. This yellowish deposited tungsten oxide should be cleaned when the filament is replaced.

2.3 Plasma Enhanced Atomic Layer Deposition (PEALD)

Atomic layer deposition (ALD) is a self-limiting deposition method, where growth is achieved by alternatively pulsing precursors and reactants into the deposition chamber.[1-3] ALD is similar to chemical vapor deposition (CVD),

however, ALD separates the precursors in the gas phase. The precursor is delivered to the chamber until a saturated molecular monolayer is adsorbed on the substrate surface. The remaining precursor is purged with a non-reactive gas and another precursor or oxidant is delivered into the chamber. This oxidant reacts with the previous precursor at the surface of substrate.

Conventional oxide ALD employs thermal activation to initiate the reaction with water molecules as the oxidizer. This thermal ALD process can deposit films, in general, between 100 ~ 600 °C. For examples: Growth temperature varies from 150 to 600 °C for TiO_2 ALD [4] and from 100 to 160 °C for ZnO ALD. [5,6] Recently, plasma enhanced ALD (PEALD) has been developed, using oxygen plasma as the oxidizer. Compared to thermal ALD, PEALD has further advantages including: an ultra low growth temperature, a shorter cycle and higher density films. [7-9] Fig. 2.4 shows a schematics of a working cycle of plasma enhanced ALD. A pulse of precursor is delivered to the reactor using argon as a carrier gas, which is followed by a nitrogen gas purge step. In an ideal process one layer of precursor remains on the surface of the substrate. In the PEALD process, the oxygen plasma is used as the oxidizer, generating oxygen radicals that insert into the precursor ligands which then evolve from the surface. The oxygen also reacts with the metal at the surface to form the oxide. Due to the nature of the self-limiting process, each cycle results in a constant thickness increase and the coating is typically conformal regardless of the morphology of the substrate surface.

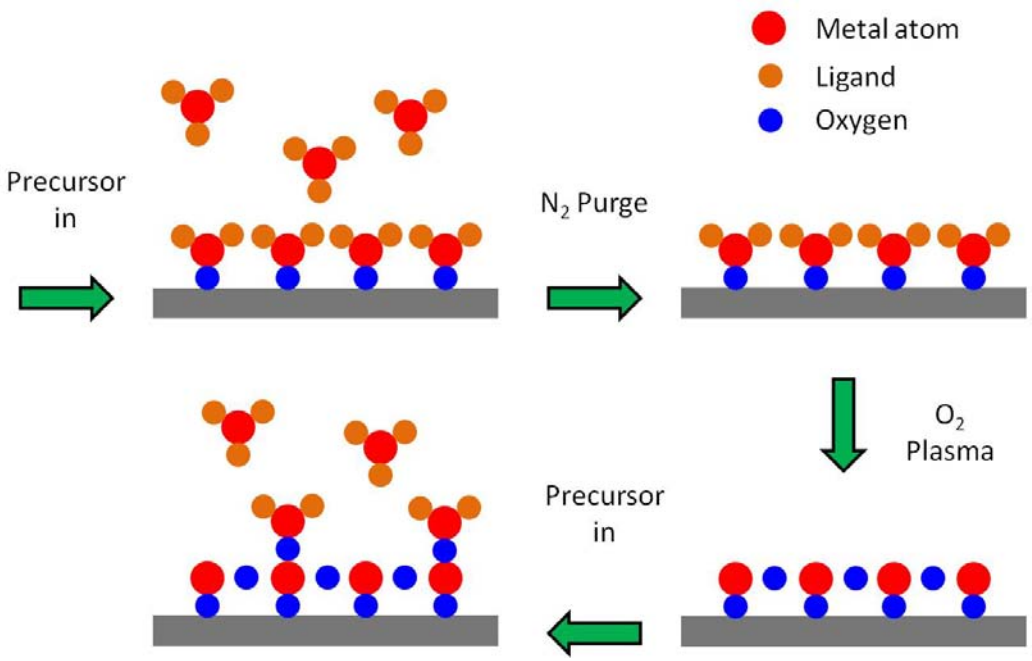

Figure 2.4 Schematic illustration of a working cycle of oxygen plasma enhanced atomic layer deposition (PEALD).

The key parameter of ALD growth is the ALD processing window, which is dependent on the growth temperature. Within the ALD growth temperature window (T1-T2), the growth rate per cycle (GPC) is constant. However, if the growth temperature is out of the temperature window, the growth rate will change. Fig. 2.5 shows the growth rate at different temperature regions.

a) Below the low growth temperature limit (T1): a1) precursor condensation at low temperature may result in thicker film deposition. In this case more than one monolayer of precursor molecules stick on the surface by both chemisorption and physical adsorption. a2) Alternatively the low temperature may result in incomplete reaction which will lower the growth rate. The precursors cannot

proceed efficiently due to insufficient thermal energy to activate the surface reactions.

b) Above the high growth temperature limit (T2): b1) the precursor may thermally decompose at the surface which results in a thicker film. b2) alternatively, the precursor may desorb and not adhere to the surface, which may reduce the growth rate. The precursor molecules adsorbed on the surface of the sample can re-evaporate due to the high temperature.

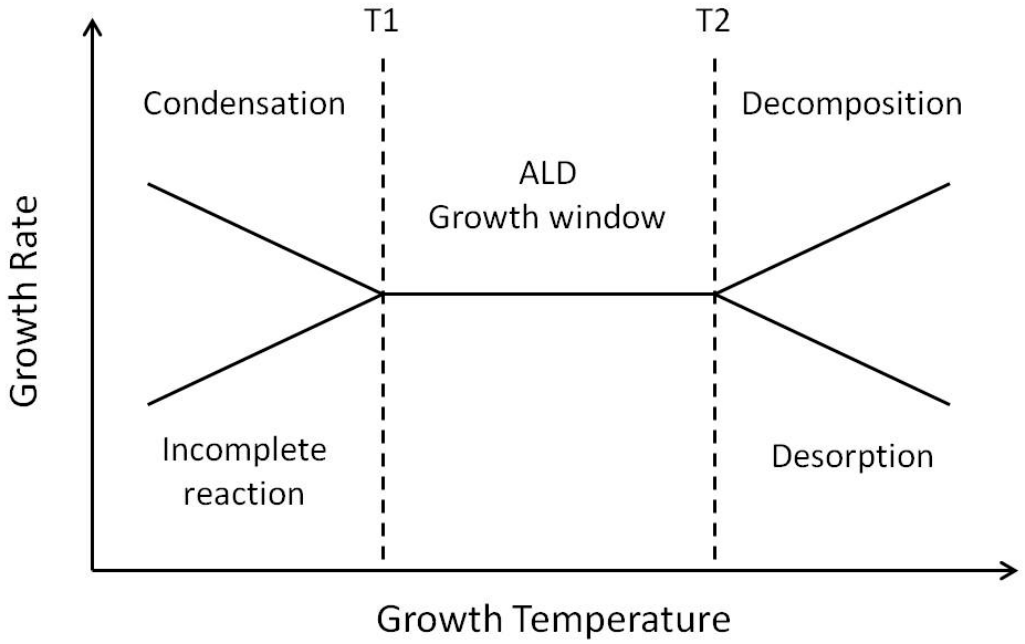

Figure 2.5 ALD growth rate at different temperature regions. The growth window is between T1 and T2.

Our plasma enhanced atomic layer deposition (PEALD) system was developed from an oxygen plasma enhanced chemical vapor deposition (PECVD) system. This system also serves as an oxygen plasma treatment system. Fig. 2.6 shows a schematic of the PEALD system. The base pressure of the chamber can

reach to 5.0×10^{-9} Torr, pumped by a turbo-drag pump, backed by a roughing pump. The remote plasma was excited with 13.56 MHz rf power applied to a helical copper coil wound around a 32mm diameter quartz tube that opens toward the sample. In these oxygen plasma treatments or ALD growth experiments, the forward plasma power was varied from 20 to 200 W, with a low reverse power of less than 30 W. During an ALD growth cycle, after the 0.1 s precursor pulse, nitrogen gas was introduced for 10 s to purge excess precursor. After the nitrogen gas purge, oxygen was introduced into the chamber 6 s before the plasma ignition, and the plasma was sustained by rf-power for another 8 s. Subsequently, the chamber was pumped for 2 s and purged by nitrogen gas for 8 s before the next cycle of growth. The pressure in the chamber during deposition was controlled by a throttle valve to a value of 100 mTorr. The Fig. 2.7 shows a schematic of the gas pulse sequence for one deposition cycle.

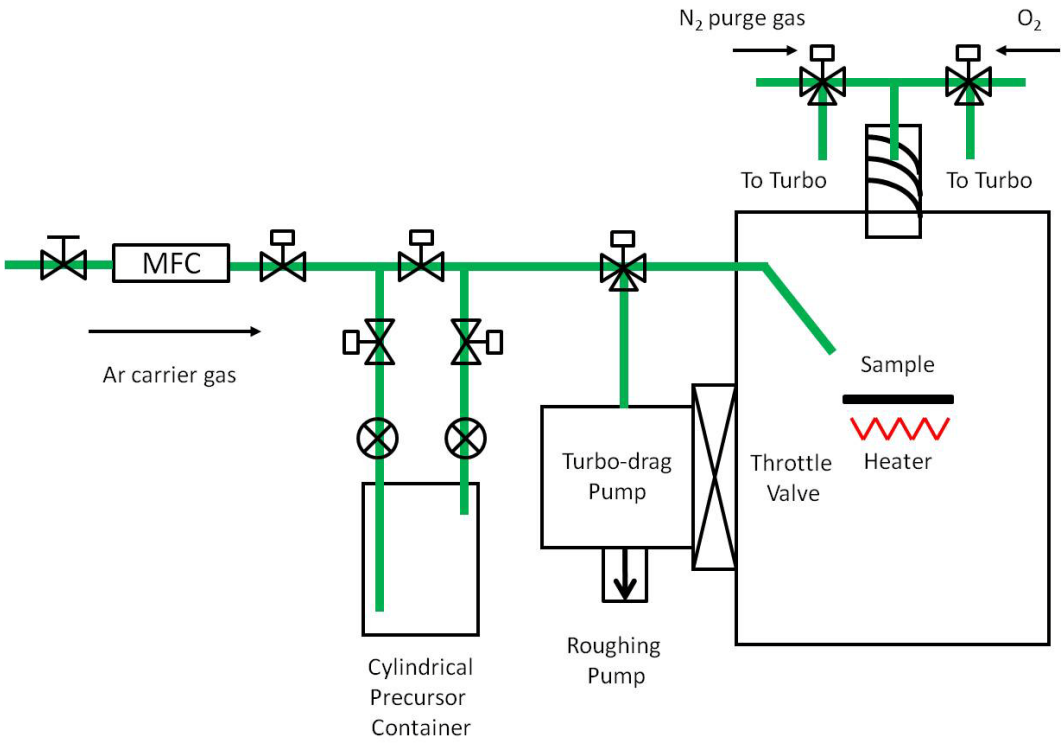

Figure 2.6 Schematic drawing of the PEALD system.

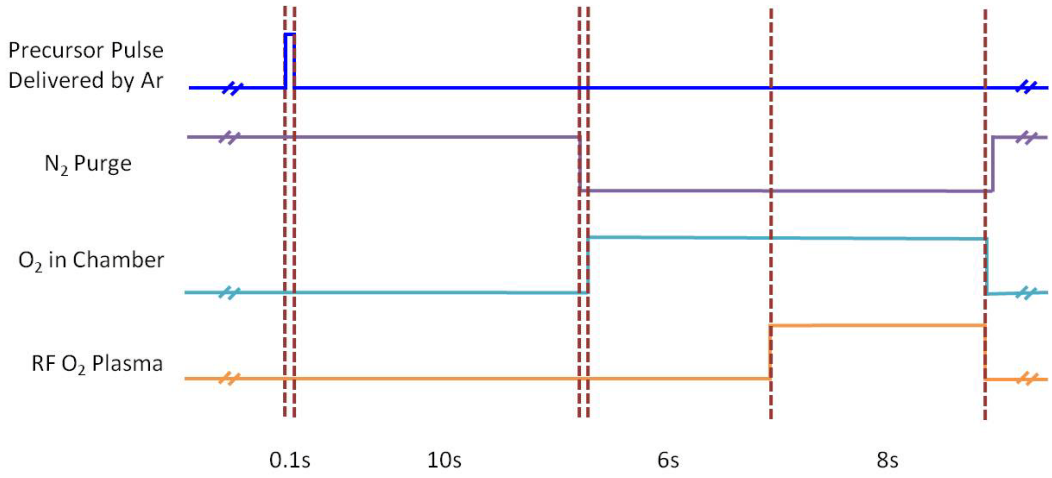

Figure 2.7 Schematic illustration of the processing sequence in one cycle deposition.

2.4 Photoemission spectroscopy

Photoemission spectroscopy system includes a light source, electron optics, an electron analyzer, and an electron detector in a vacuum environment. Incident photons strike the sample and excite the electrons from relatively deeply into (~ micrometers) the sample. However, most of the electrons which are excited in the deep region of the sample are not emitted due to scattering and recombination. Only excited electrons near the surface can escape from the sample. The dependence of the average electron escape depth vs kinetic energy is presented in Fig. 2.8.[1] The electrons which are generated near the sample surface will be emitted to the vacuum if they still have enough kinetic energy to overcome the work function of the material. Many scattered electrons are also emitted, but these electrons show up as secondaries in the spectrum and cannot be directly related to the valence band electronic states.

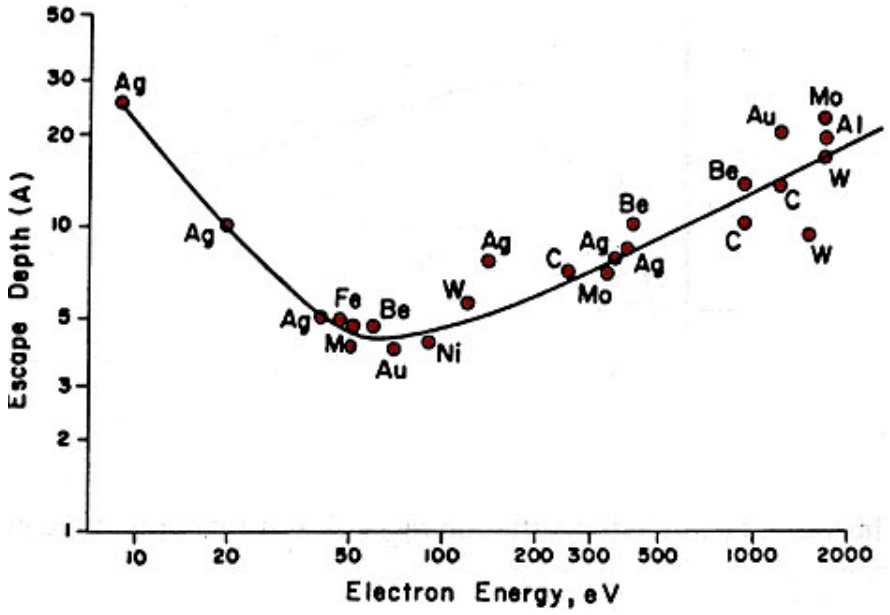

Figure 2.8 Electrons average escape depth vs kinetic energy. [10]

Two main photoemission spectroscopy systems, X-ray photoelectron spectroscopy (XPS) and Ultraviolet photoelectron spectroscopy (UPS) have been employed in our studies. The main difference between XPS and UPS is the light source. XPS employs X-ray as the light source, and for our system a twin anodes X-ray gun is installed with Mg and Al sources. The photon energies of these two sources are Mg $K_{\alpha 1}$ (= 1253.6eV) and Al $K_{\alpha 1}$ (= 1486.6eV). UPS employs Ultraviolet light as the light source, which can be generated by a gas plasma discharge. Usually, noble gases like helium and argon serve as the discharge gas. In our system, research grade purity (99.9999%) He gas serves as the discharge gas. In the series of He emitting lines, two of the strongest lines are commonly used, He I with a photon energy of 21.2 eV and He II with a photon energy of 40.8 eV. The He I line is more widely employed as it is the strongest emitting line. The other main difference is the energy of the emitted electrons. The electrons in the atomic core levels can be excited by the high energy, X-ray photons. However, the lower energy UV light photons (He I) are employed to excite the electrons in the valence band. Other differences such as analyzer and chamber, are based on the emitted electron energy range. Fig. 2.9 shows a comparison of XPS and UPS.

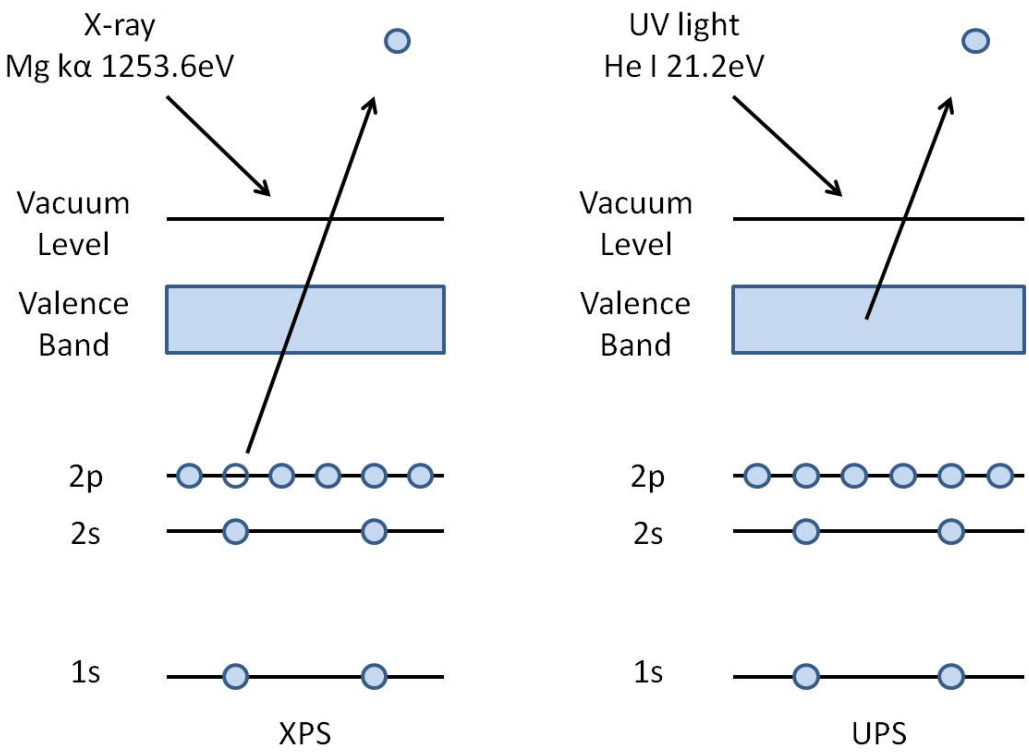

Figure 2.9 Schematic comparison of the photoemission process for X-ray photoemission spectroscopy (XPS) and ultraviolet light photoemission spectroscopy (UPS).

2.4.1 X-ray Photoemission Spectroscopy

The electrons are excited by X-ray photons, emitted out of the sample, and collected and dispersed by an electron spectrometer. The spectrometer records the number of electrons by their kinetic energies, usually from 0 ~ 1keV. The kinetic energy is typically converted into the binding energy using the following relation:

$$BE = h\nu - KE - W, \quad (2.1)$$

where BE is the electron binding energy, hν is X-ray photon energy, KE is the detected kinetic energy, and W is the work function of the spectrometer. The kinetic energy is referred to the vacuum level, and the work function is the energy

between vacuum level and Fermi level. Thus, the binding energy is referred to Fermi level. The Fermi level is defined as a zero binding energy.

2.4.2 Ultraviolet light Photoemission Spectroscopy

The electrons are excited by UV photons, emitted out of sample, and collected and dispersed by the electron spectrometer. The spectrometer also records the number of electrons according to their kinetic energies, typically in a range of 0 to 50 eV. The kinetic energy is usually converted into binding energy using the following relation:

$$BE = h\nu - KE - W + V, \quad (2.2)$$

where BE is the electron binding energy, hν is the UV photon energy, KE is the kinetic energy, and W is the work function of the spectrometer. V is the bias between the sample and analyzer which is grounded. Usually, the sample is negatively biased to improve the electron collecting efficiency of the analyzer. The kinetic energy is referred to the vacuum level, and the work function is the energy between the vacuum level and Fermi level. Thus, the binding energy is referred to the Fermi level. The Fermi level is then defined as the zero binding energy.

2.4.3 Calibration of XPS and UPS

The XPS and UPS spectra are usually presented in binding energies rather than kinetic energies. However, the real value measured by the analyzer is the kinetic energy of the electrons. When the kinetic energy is converted into the binding energy by Equations 2.1 or 2.2, it is necessary to determine the work function of the analyzer to calibrate the work function.

Usually, for calibration of XPS and UPS, the sample is a clean metal surface without an oxide. Oxide samples often display charging related shifts which would limit the calibration accuracy. The photons exciting electrons out of the sample results in positive charge accumulation at the surface of sample. If the sample is an insulator, the accumulated positive charges cannot be compensated by electrons, which results in a shift of the whole photoemission spectra to higher binding energy. The conducting samples, usually metals, can be achieved by in-situ growth and characterization without exposure to air. Noble metals, such as Au, Pt and Ag, can also serve as calibration samples due to their inherent resistance to oxidation.

There are two common ways to determine the work function of the analyzer. One is to measure a core level and compare the peak value to a known value. The other way, is to determine the Fermi level of the spectrum, and set this value as zero in the binding energy scale. For XPS calibration, the first way, peak position comparison, is typically employed. The reason is that XPS signal at Fermi level (~ zero binding energy) is relative weak. However, for UPS calibration, the second way, Fermi level determination, is preferred. The Fermi level obtained by UPS is clear for metal surface spectra. But the peak features of the valence band spectra are typically broad and asymmetric, due to the electron states distribution.

Fig. 2.10 shows an XPS calibration spectrum with Au 4f peaks. The Au 4f peaks are the strongest lines in the Au photoemission spectrum. From curve fitting, the Au 4f 7/2 peak position is determined as 83.9 eV with a full with at

half maximum (FWHW) of 1.0 eV. Comparing to the standard value of the Au 4f 7/2 peak position at 84.0 eV, results in a correction of the binding energy by + 0.1 eV. Also the FWHW can be treated as a resolution parameter of the XPS.

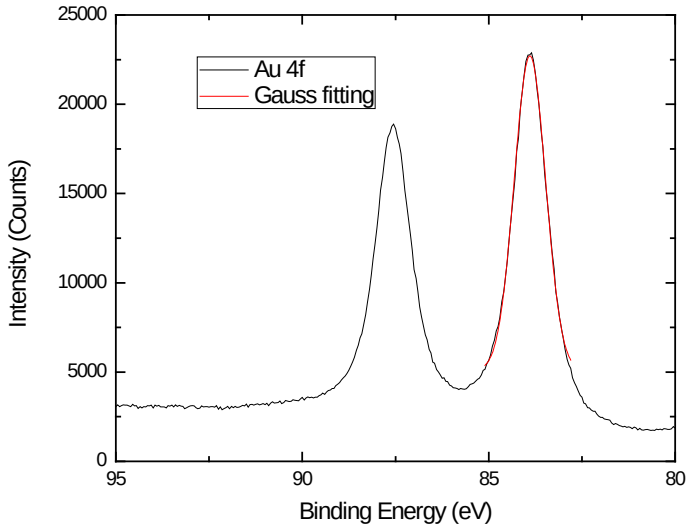

Figure 2.10 X-ray photoemission spectra of Au 4f peaks.

Fig. 2.11 shows a UPS calibration spectra of a Au film for calibration. Both the He I and He II lines are employed and a 4 volts bias was applied to the sample. The front cutoff of the UPS spectrum, which is contributed by the electrons with the highest kinetic energy, indicates the Fermi level of a conducting sample or the valence band maximum (VBM) of an insulator sample. The back side cutoff of a UPS spectrum, which is contributed by the electrons with the lowest kinetic energy, indicates the work function of the sample. For this gold film, the Fermi level is regarded as the reference point or zero point. In the Fig. 2.11 (a), the front side cutoff shows a value of 20.8 eV, indicating the electrons at the Fermi level excited by He I UV photons have a kinetic energy of 20.8 eV. According to equation 2.2, with $h\nu$ = 21.2 eV, KE = 20.8 eV, V = 4 eV,

and BE = 0.0 eV as the zero point, the work function of the analyzer, W, is calibrated as 4.4 eV.

Fig. 2.11(b) and (c) shows the Au film UPS spectra with He II excitation. Fig. 2.11 (b) displays whole spectrum and Fig. 2.11 (c) is enlarged to display the high kinetic energy part. The UPS He II mode can be obtained by decreasing the He pressure of the lamp. Initially, the He lamp is ignited at normal He I pressure. In that mode, the lamp is bright with an orange color. Then the pressure of He lamp is decrased, until the lamp is close to the extinguishing point. In the He II mode, the lamp is dim with a lilac (light purple) color. However, even in the He II mode, the He I line (21.2 eV) is still stronger that the He II line. As shown in Fig. 2.11(b), the signal at low kinetic energies is mostly contributed by He I photons and the signal at high kinetic energies which is larger than 21 eV is contributed by He II photons. Comparing the intensity of these two parts of the signal, shows that the signal from He II line is weaker than the He I line component, even when the lamp is operated in the He II mode. Fig. 2.11(c) focuses on the high kinetic energy part of spectrum. The front side cutoff is determined as 40.4 eV. According to equation 2.2, with $h\nu$ = 40.8 eV, KE = 40. eV, V = 4 eV, and BE = 0.0 eV as the zero point, the work function of analyzer W is calibrated as 4.4 eV, which is consistent with the value under the He I mode.

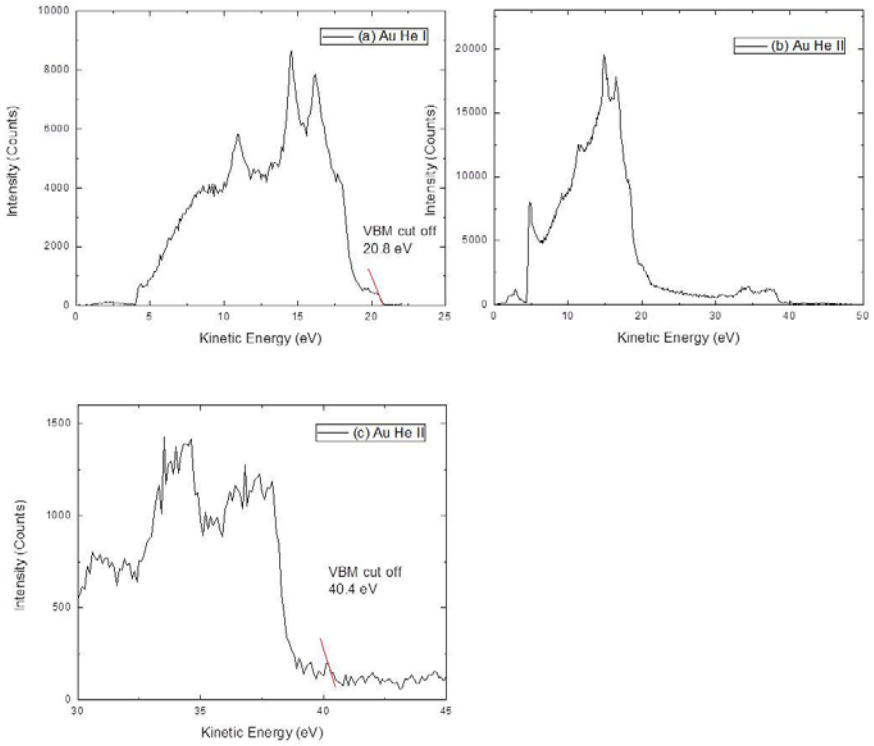

Figure 2.11 Ultraviolet photoemission spectra of (a) Au foil operated in He I mode , (b)) Au foil operated in He II mode and (c) enlarged high kinetic energy part of (b).

2.5 Band alignment analysis method

The band alignment analysis used in this dissertation is based on the XPS and UPS measurements. In our study, the typical sample structures were thin oxide layers on top of a doped Si wafer with a native oxide. The thickness of each thin oxide layer is 1~2 nm and the total thickness of the oxide layers is 4~5 nm. The valence band maximum is determined by the front side cutoff of the UPS spectra. As the UPS measurement is very sensitive to the surface, we presume the VBM determined by UPS is the value at the surface of the layer. For XPS, we measured the core level of the elements in the sample. We presume the energy

separation between the core level and the VBM is characteristic of the material and does not change during the process. Thus, the shifting of XPS core levels reflects a change of the VBM. Considering the XPS detecting depth is 5~6 nm, the XPS signal has contributions from all the oxide layers and a portion of the Si bulk region near the surface.

2.5.1 Insulator layer

Thin oxide layers, typically 1~2 nm thick, are grown on the Si substrate. During the processes, charges may transfer between the oxide layers and the Si substrate. We presume the charges are trapped at or near the interface of the oxide layers, and not inside of the oxide layers. According to Poisson's equation, the electric potential varies linearly across the oxide layer. Thus the core level binding energy is also linearly distributed across the oxide layer. Previous study proposes that the observed XPS peak position is characteristic of the center of the oxide layer. [11] The electric potential across the oxide layer can then be calculated from the shifts of the XPS peak positions. When the core level of the material measured by XPS shifts by $\Delta 1$ during the process, it indicates the VBM of the oxide is also shifted by $\Delta 1$ eV at the center of an oxide layer. If this shift is not affected by other band shifts, the electric potential across this oxide layer is calculated as $2\times\Delta 1$ eV, as shown in Fig. 2.12 (a). If this shift $\Delta 1$ has contributions from other band shifts, as shown in the Fig. 2.12 (b), the whole band is shifted up by $\Delta 2$ at the interface 2. The electric potential across this oxide layer is calculated as $2 \times (\Delta 1 - \Delta 2)$ eV.

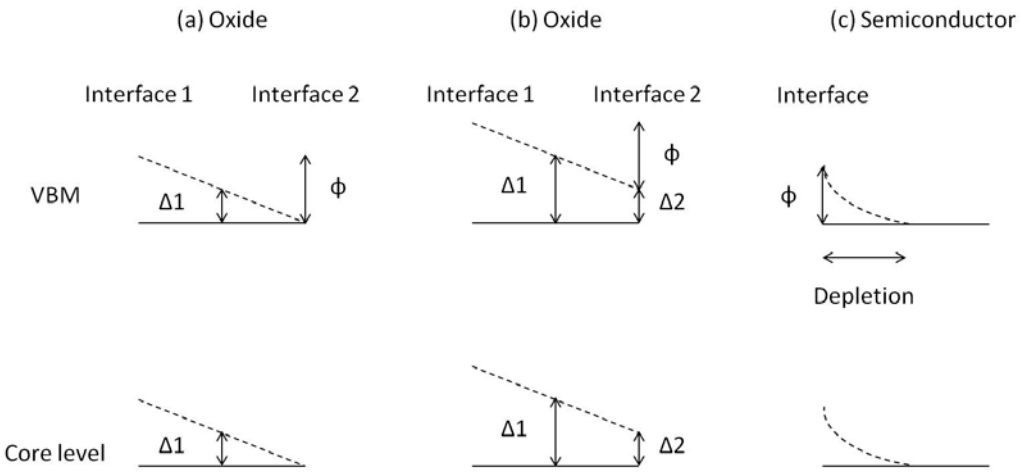

Figure 2.12 Relationship between the XPS peak shift and the VBM shift, (a) a shift of an oxide layer without affected the other layers, (b) a shift of an oxide layer which does affect other layers, and (c) band bending in the semiconductor substrate.

2.5.2 Semiconductor substrate

In this study, doped Si wafers were employed as sample substrates. During the process, the trapped charges at the oxide layers can induce a depletion region in the Si near the surface. Since the charges in depletion region are uniformly distributed, according to Poisson's equation, the electric potential has a parabolic dependence across this depletion region, as shown in Fig. 2.12 (c). As the width of the depletion layer is usually tens to above one hundred nanometers, the XPS signal is mostly contributed by the interface of the SiO_2 and Si. Thus, the Si band bending is the same as the XPS peak shifting $\Delta 1$, as shown in Fig. 2.12 (c). However, if the Si substrate is heavily doped, (the doping concentration is more than 1×10^{19} cm^{-3}), the width of the depletion layer is less than 10 nm, which is

comparable with the XPS detection depth. In that case, the XPS peak position cannot be treated as the value at the interface of oxide and Si.

The following describes the approach to account for this correction and to determine the band bending at the Si/SiO_2 interface from a measured shift of a core level peak. The photoelectron signal intensity, I, will be attenuated for increased depths in the film. The intensity from any thickness is given by

$$I = I_0 e^{-z/\lambda}, \quad (2.3)$$

where I_0 is the signal intensity for the atoms at the surface, z is the depth from which the photoelectron originates, and λ is the photoelectron inelastic mean free path.

The band bending can be calculated using Poisson's equation:

$$\nabla^2 \varphi = -\frac{\rho_f}{\varepsilon}, \quad (2.4)$$

where φ is the electric potential, ρf is the charge density and ε is the dielectric permittivity.

The band bending E can be described by

$$E(z) = \frac{1}{2}\frac{ne}{k\varepsilon_0}(w-z)^2, \quad (2.5)$$

where n is the doping concentration of p-type Si wafer, ~1×10^{19} cm^{-3}, e is the electron charge, ~1.6×10^{-19} C, k is the dielectric constant of Si ~11.9, ε_0 is the vacuum permittivity, ~8.85×10^{-12} F/m, w is the depletion layer width, and z is the depth form the Si/SiO_2 interface.

In this case the band bending that corresponds to the observed XPS core level shift, E_{ob}, can be described using the following expression:

$$E_{ob} = \frac{\int_0^w E(z)e^{-z/\lambda}dz}{\int_0^w e^{-z/\lambda}dz} = \frac{\int_0^w \frac{1}{2}\frac{ne}{k\varepsilon_0}(w-z)^2 e^{-z/\lambda}dz}{\int_0^w e^{-z/\lambda}dz}, \quad (2.6)$$

where λ is 2.7 nm, the photoelectron inelastic mean free path in Si for Mg kα X-ray source [12]. Table 1 lists the calculated core level shift for the different bending conditions. The calculation is based on a doping concentration of ~1 × 10^{19} cm^{-3}, and the XPS peak shift is regarded as the observed band bending. The band bending at the interface is calculated with different width of the depletion layer, as listed in Table 2.1.

Table 2.1. The calculated results of band bending at the Si/SiO_2 interface and observed band bending for XPS measurement, based on the varied width of the depletion layer.

Width of depletion (nm)	Band Bending (observed) (eV)	Band Bending (interface) (eV)
5	0.09	0.19
6	0.14	0.27
7	0.20	0.37
8	0.28	0.49
9	0.36	0.62
10	0.47	0.76
11	0.58	0.92

REFERENCES

[1] T. Suntola, Thin Solid Films 216, 84 (1992).

[2] George, S. M., Ott, A. W., and Klaus, J. W. J. Phys. Chem., 100, 13121 (1996).

[3] M. Leskela and M. Ritala, Thin Solid Films 409, 138 (2002).

[4] Ritala, M., Leskela, M., Nykanen, E., Soininen, P., and Niinisto, L. Thin Solid Films, 225, 288 (1993).

[5] Yamada, A., Sang, B. S., and Konagai, M. Appl. Surf. Sci., 112, 216 (1997).

[6] Yousfi, E. B., Fouache, J., and Lincot, D. Appl. Surf. Sci., 153, 223 (2000).

[7] Heil, S. B. S., Kudlacek, P., Langereis, E., Engeln, R., van de Sanden, M. C. M., and Kessels, W. M. M. Appl. Phys. Lett., 89, 131505 (2006).

[8] Langereis, E., Creatore, M., Heil, S. B. S., Van de Sanden, M. C. M., and Kessels, W. M. M. Appl. Phys. Lett., 89, 081915 (2006).

[9] Lim, J. W., and Yun, S. J. Electrochem. Solid-State Lett., 7, F45 (2004).

[10] C. B. Drake. J. Vac. Sci. Tech. 13, 761 (1976).

[11] C. C. Fulton, G. Lucovsky, and R. J. Nemanich, J. Appl. Phys. 99, 063708 (2006).

[12] S. Tanuma, C. J. Powell, and D. R. Penn, Surf. Interface Anal., 17, 911 (1991).

Chapter 3

BAND ALIGNMENT OF VANADIUM OXIDE AS AN INTERLAYER IN A HAFNIUM OXIDE-SILICON GATE STACK STRUCTURE

3.1 Abstract

Vanadium oxide (VO_2) is a narrow band gap material (Eg = 0.7 eV) with a thermally induced insulator-metal phase transition (IMT) at ~343 K and evidence of an electric field induced transition at T< 343 K. To explore the electronic properties of VO_2, a sandwich structure was prepared with a 2 nm VO_2 layer embedded between an oxidized Si(100) surface and a 2 nm HfO_2 layer. The layer structure was confirmed with high resolution transmission electron microscopy (TEM). The electronic properties were characterized with x-ray and ultraviolet photoemission spectroscopy, and the band alignment was deduced on both *n*-type and *p*-type Si substrates. The valence band offset between VO_2 and SiO_2 is measured to be 4.0 eV. The valence band offset between HfO_2 and VO_2 is measured to be ~3.4 eV. The band relation developed from these results demonstrates the potential for charge storage and switching for the embedded VO_2 layer.

3.2 Introduction

Vanadium dioxide (VO_2) is a narrow band gap material (Eg = 0.7eV). [1] The narrow band gap could enable vanadium dioxide films to act as charge storage sites if embedded in a gate stack structure. [2] Other studies have shown that vanadium dioxide nanostructures can be embedded in an oxide layer which

can be considered for optical data storage. [3] Vanadium dioxide displays an insulator to metal transition (IMT) at ~ 343 K with an abrupt three order magnitude change of resistivity, which is typically accompanied by a structural phase transition.[4-6] The other two common vanadium oxides, V_2O_3 and V_2O_5, show IMT at 160 K[7] and 530 K, respectively[8]. It has also been proposed that the application of an electric field to a VO_2 film may increase the carrier density which could drive the transition to the metallic phase. This electric field induced phase transition could lead to a new class of electric switching devices,[9] which could enable oxide based electronics.[10, 11]

To develop efficient charge storage or switching devices based on the electronic properties of VO_2, we need to understand the band alignment relative to dielectric interfaces and the Si substrate. In this study, we have prepared a thin VO_2 layer as an interlayer inserted between the adjoining high-k dielectric material (HfO_2), and oxidized n- and p-type Si substrates. The layer structure was confirmed with high resolution transmission electron microscopy (TEM). The measurements on *n*- and *p*-type substrates explore charge transfer between the layers. Hafnium oxide (HfO_2) is one of the most used high-k gate dielectric materials with a dielectric constant of 20-25 and band gap of 5.6 eV[12]. In this structure the VO_2 layer is able to accept charge through tunneling from the substrate. With the high-k upper layer an applied gate voltage would control the potential of the VO_2 layer relative to the substrate. The band relations for HfO_2, VO_2, and the oxidized *n*- and *p*-type Si substrate are determined from *in-situ*

photoemission measurements, and the interfacial charge transfer during the growth is discussed.

3.3 Experiment

The experiments were accomplished *in-situ* using an integrated ultrahigh vacuum (UHV) system. This system involves a linear ~20 m UHV transfer line chamber with a base pressure of 5×10^{-10} Torr that connects different process and characterization chambers. In this study, the following systems are used: remote oxygen plasma for cleaning, reactive electron beam deposition system for HfO_2 and VO_2 growth, x-ray photoelectron spectroscopy (XPS) for core level analysis, and ultraviolet photoelectron spectroscopy (UPS) for valence band spectra.

The samples are grown on 25mm dia. *n*-type, phosphorous doped, (100) silicon wafers with a resistivity of 0.05-0.09 Ω·cm and *p*-type, boron doped, (100) silicon wafers with resistivity of 0.006-0.01 Ω·cm. Before loading into the UHV chamber, wafers are cleaned in an ultrasonic acetone bath for 15 min, an ultrasonic methanol bath for another 15 min., and dried in ultra high purity nitrogen gas. After transfer into the UHV system, the Si(100) surfaces are cleaned and oxidized by a remote oxygen plasma. The plasma exposure conditions are as follows: substrate at room temperature, 60 mTorr oxygen pressure, gas flow of 10 standard cubic centimeters per minute (sccm), and rf power of 30W to excite the plasma. The remote oxygen plasma can effectively remove hydrocarbon contamination and passivate the Si surface with a thin SiO_2 layer [13]. After in situ cleaning, the sample was annealed at 500°C for 5 min. for defect reduction

and removal of adsorbed oxygen. The surfaces were then characterized by XPS and UPS.

The VO_2 and HfO_2 films were deposited in the reactive electron beam deposition system which has a base pressure of 7×10^{-9} Torr. A 2 nm thick VO_2 film was deposited onto the cleaned Si wafer at 550 ºC with an oxygen gas pressure of 6×10^{-4} Torr. Another 2 nm HfO_2 film was directly deposited over the VO_2 layer at room temperature with an oxygen pressure of 2×10^{-6} Torr. For each layer a growth rate of 0.01 nm/s was maintained with a quartz crystal thickness rate meter.

The sample was characterized by XPS and UPS at each step. XPS characterization is performed at a base pressure of 6×10^{-10} Torr using the 1253.6 eV Mg Kα line of a VG XR3E2 dual anode source and a VG microtech Clam II analyzer operated at a resolution of 0.1 eV. The resolution of the analyzer was determined from the full width at half maximum (FWHM) of a gold 4f 7/2 spectral peak to be approximately 1.0 eV; however, through curve fitting, the centroid of spectral peaks can be resolved to ± 0.1 eV. Ultraviolet photoemission spectra are obtained at a base pressure of 8×10^{-10} Torr using the He I line at 21.2 eV and a VSW 50 mm mean radius hemispherical analyzer and VSW HAC 300 controller operated at an electron energy resolution of 0.15 eV. A negative 4.00 V bias was applied to the substrate to overcome the work function of the analyzer. A representative sample was observed in cross-section geometry using a JEOL JEM 4000EX high-resolution electron microscope operated at 400 kV.

3.4 Results

The *in-situ* experiments consisted of the following process: 1) remote oxygen plasma cleaning, 2) XPS and UPS characterization, 3) deposition of ~2 nm vanadium oxide, 4) XPS and UPS characterization, 5) deposition of ~2 nm of hafnium oxide, 6) XPS and UPS characterization. The results of XPS and UPS spectra of each step are shown in Figs. 3.1- 3.4. The XPS observation "windows" were set for the Si 2p, O 1s, V 2p and Hf 4f core levels. The carbon XPS peaks were below the detection limit before and after deposition.

3.4.1 Si substrate with native oxide layer

The Si 2p core level is shown in Fig. 3.1. The initial SiO_2 layer thickness can be determined from the ratio of the bulk (~99 eV) and SiO_2 (~104 eV) Si peaks. The SiO_2 thickness was determined using the following equation [14]: $t_{ox} = \lambda_{SiO2} \ln \{[(1/\beta) (I_{SiO2}^{exp}/ I_{Si}^{exp})] + 1\}$, where λ_{SiO2} is the attenuation length of the Si 2p photoelectrons in SiO_2, $\beta = (I_{SiO2}^{\infty}/ I_{Si}^{\infty})$ is the ratio of the Si 2p intensity from thick SiO_2 and a Si wafer, and $I_{SiO2}^{exp}/ I_{Si}^{exp}$ is the measured ratio of normal incident XPS Si 2p intensities. For our XPS instrument configuration, the analyzer is normal to the sample. We take λ_{SiO2} to be 2.8±0.02 nm, an average from five references [15-19], and β to be 0.83[19]. With these values and the measured intensities ratio, the thickness of the initial SiO_2 layer on the Si wafer is determined to be 0.8±0.1 nm.

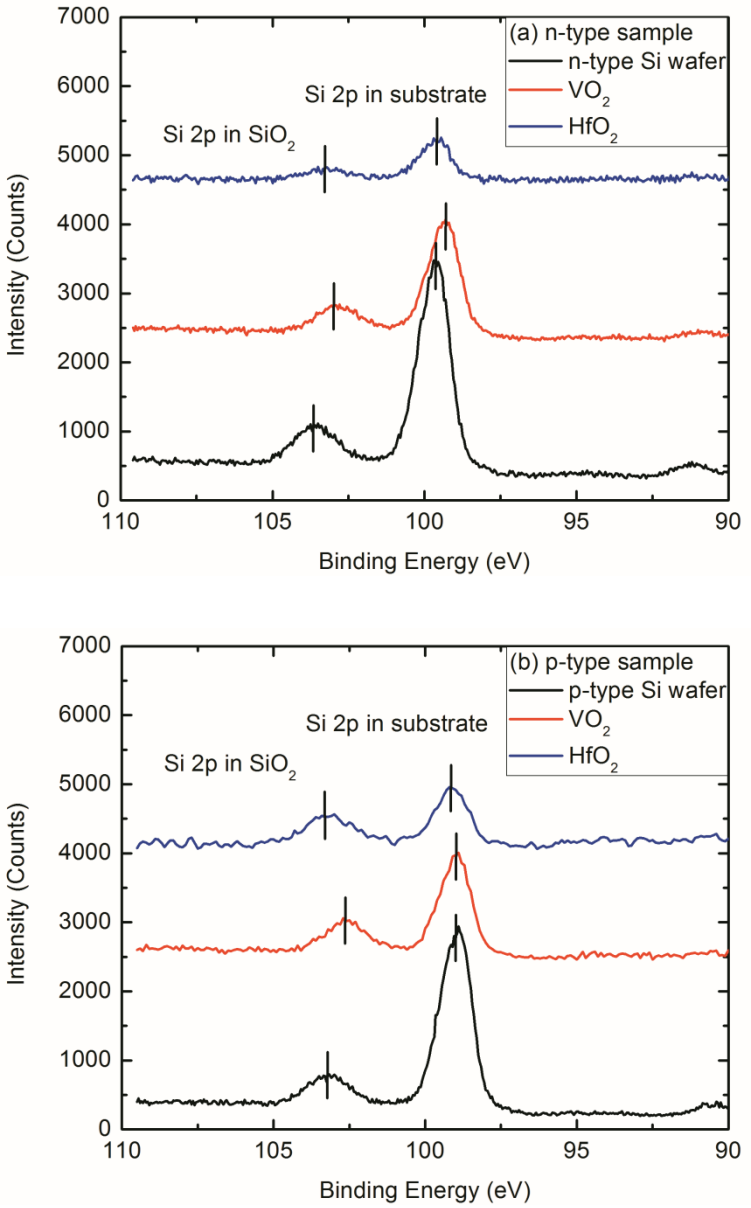

Figure 3.1 X-ray photoemission spectra of Si 2p peaks for (a) plasma oxidized *n*-type Si(100) and (b) *p*-type Si(100) sample. The curves are for the oxidized Si wafer, after deposition of VO_2 on Si and after deposition of HfO_2.

For the *n*-type sample, the XPS binding energies of the Si 2p, O 1s, V 2p3/2 and Hf 4f 7/2 are summarized in Table 3.1. The initial Si 2p peaks are at 99.7 and 103.6 eV, respectively, corresponding to bulk Si near the surface and the

SiO_2 layer of the oxidized Si. Results have established that the Si 2p core level is 98.8eV below the valence band maximum (VBM) [20]. For the heavily doped *n*-type Si wafer, the Fermi level is at 0.9-1.0eV above the VBM. Therefore, the initial *n*-type Si substrate displays a flat band condition as the Si 2p peak is at 99.7 eV (98.8 + 0.9 eV). After VO_2 deposition, the Si bulk and SiO_2 related peaks are shifted to lower binding energies of 99.4 and 103.0 eV, respectively. After 2 nm HfO_2 deposition, the Si peaks shift back to 99.6 and 103.2 eV, respectively. The shifts in the Si bulk feature are attributed to a change of the band bending in the Si substrate, and the differential shifts between the Si substrate and Si oxide features are attributed to an electric potential across the SiO_2 layer.

Table 3.1 XPS Si 2p, O1s, V2p 3/2 and Hf 4f 7/2 core level results for HfO_2/VO_2/oxidized *n*-type Si(100). Values have an uncertainty of ± 0.1 eV.

n-sample	Si 2p (eV)		O 1s (eV)		V 2p3/2 (eV)	Hf 4f7/2 (eV)
Process	Si bulk	SiO_2	Main	Shoulder		
Substrate	99.7	103.6	532.6	/	/	/
2nm VO_2	99.4	103.0	530.6	532.0(SiO_2)	516.0	/
2nm HfO_2	99.6	103.2	530.9	530.3(VO_2)	515.6	17.9

For the *p*-type sample, the XPS binding energies of the Si 2p, O 1s, V 2p3/2 and Hf 4f 7/2 core levels are summarized in Table 3.2. The bulk Si 2p peak is at 99.0 eV. Assuming that the Fermi level is 0.1 eV above the VBM for the heavily doped *p*-type Si wafer, and the Si 2p core level is 98.8 eV below the

valence band maximum (VBM), the results indicate the initial *p*-type Si substrate is at a flat band condition.

Table 3.2 XPS Si 2p, O1s, V2p 3/2 and Hf 4f 7/2 core level results for HfO_2/VO_2/oxidized *p*-type Si(100). Values have an uncertainty of ± 0.1 eV.

p-sample	Si 2p (eV)		O 1s (eV)		V 2p3/2 (eV)	Hf 4f7/2 (eV)
Process	Si bulk	SiO_2	Main	Shoulder		
Substrate	99.0	103.2	532.2	/	/	/
2nm VO_2	99.0	102.6	529.9	531.6(SiO_2)	516.2	/
2nm HfO_2	99.1	103.2	530.8	529.7(VO_2)	/	17.9

After VO_2 deposition, the Si bulk and SiO_2 related peaks are shifted to lower binding energies of 99.0 eV and 102.6 eV, respectively. After 2.0 nm HfO_2 deposition, the Si bulk and SiO_2 related 2p peaks shift to higher binding energies of 99.1 and 103.2, respectively.

3.4.2 2 nm VO_2

The O 1s and V 2p core levels are shown in Fig. 3.2. For the *n*-type substrate, the peak at 532.6 eV is the O 1s signal of the oxygen in the SiO_2 layer. After VO_2 deposition, the peak at 530.6 eV is attributed to the O 1s signal corresponding to the VO_2 layer. Also a shoulder peak at the left-hand side of the 530.6 eV peak is attributed to the O 1s in the SiO_2 layer. This shoulder peak is located at 532.0 eV, which is 0.6 eV lower than the initial state. This shift is consistent with the shift of the Si peak in the SiO_2 layer which is also 0.6 eV lower after VO_2 deposition. After the HfO_2 capping layer, the O 1s peak is

mostly due to oxygen in the HfO_2. After the initial 2.0nm VO_2 deposition, the V 2p3/2 peak is located at 516.0 eV. After the HfO_2 deposition, the V 2p3/2 peak is shifted to a lower binding energy of 515.6 eV, which may be due to the extraction of oxygen from the VO_2 layer during HfO_2 deposition. The V 2p3/2 peak at 513.3 eV may be due to other vanadium oxides [21] or vanadium-hafnium interface oxides.

For the *p*-type substrate, (Fig. 3.2(b)), the peak at 532.2 eV is the O 1s signal of the oxygen in the SiO_2 layer. After VO_2 deposition, the peak at 529.9 eV is attributed to the O 1s signal of oxygen in the VO_2 layer. Also, a shoulder peak at the left-hand side of the 531.6 eV peak is attributed to the O 1s from the SiO_2 layer. This shoulder peak is located at 531.6 eV, which is 0.6 eV lower than the initial state. This shift is comparable with the Si peak shift in the SiO_2 layer which is also 0.6 eV lower after VO_2 deposition. The V 2p3/2 peak is located at 516.2 eV. After the 2.0 nm HfO_2 layer deposition, the intensity of the V 2p3/2 peak due to VO_2 is significantly decreased. Again a peak located around 513.5 eV is detected, which may be other vanadium oxides or a vanadium-hafnium complex oxide. The main O1s peak, located at 530.8 eV after the 2.0 nm HfO_2 capping layer, represents the oxygen signal from the HfO_2 layer.

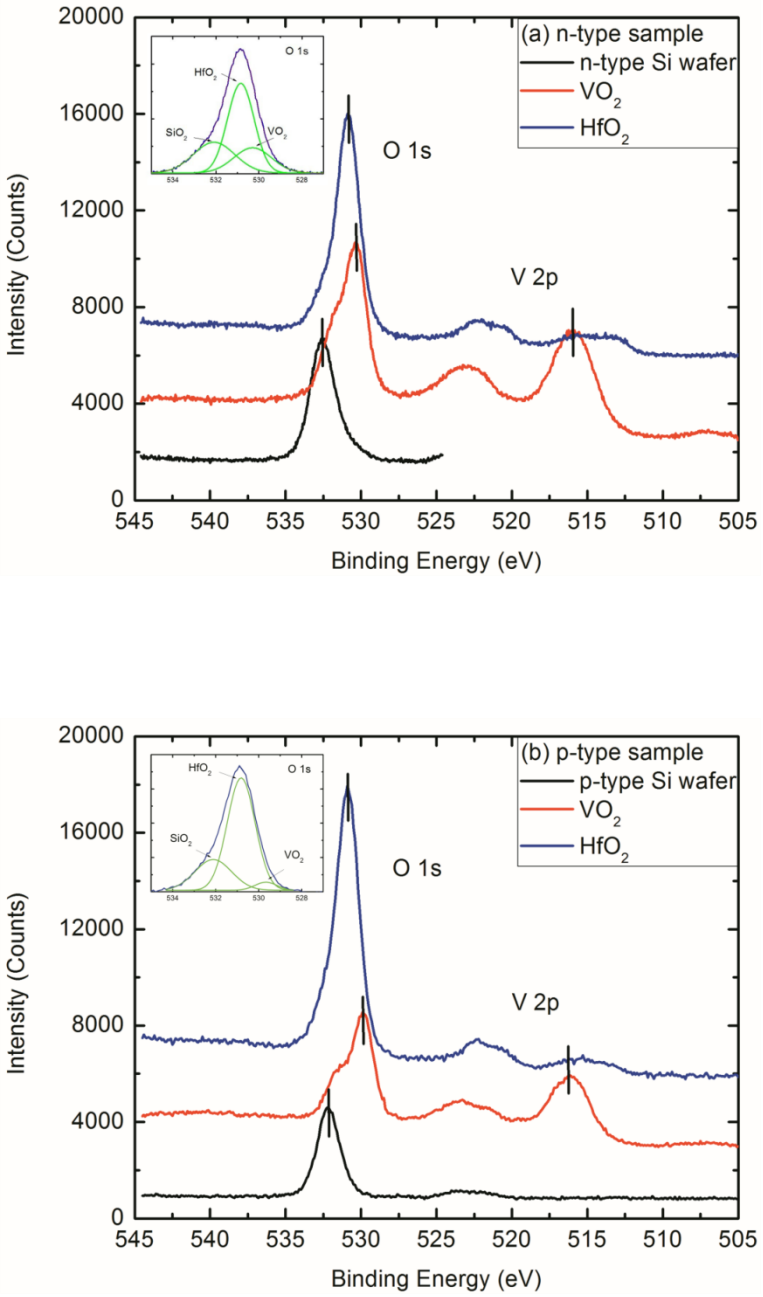

Figure 3.2 X-ray photoemission spectra of O 1s and V 2p peaks for (a) plasma oxidized *n*-type Si(100), (b) vanadium oxide on oxidized *n*-type Si(100) and (c) HfO_2 and VO_2 on oxidized *n*-type Si(100). The figure inset shows the O1s curve fitting peaks for 2 nm HfO_2 on *n*-type and *p*-type Si.

3.4.3 2 nm HfO_2

Fig. 3.3 presents the Hf XPS 4f peaks as evidence of the HfO_2 layer. For the 2.0 nm HfO_2 layer on *n*-type Si, the Hf 4f 7/2 and 4f 5/2 peaks are located at 17.9 and 19.4 eV, respectively. For the 2.0 nm HfO_2 layer on *p*-type Si, the Hf 4f 7/2 and 4f 5/2 peaks are located at 17.9 and 19.4 eV, respectively.

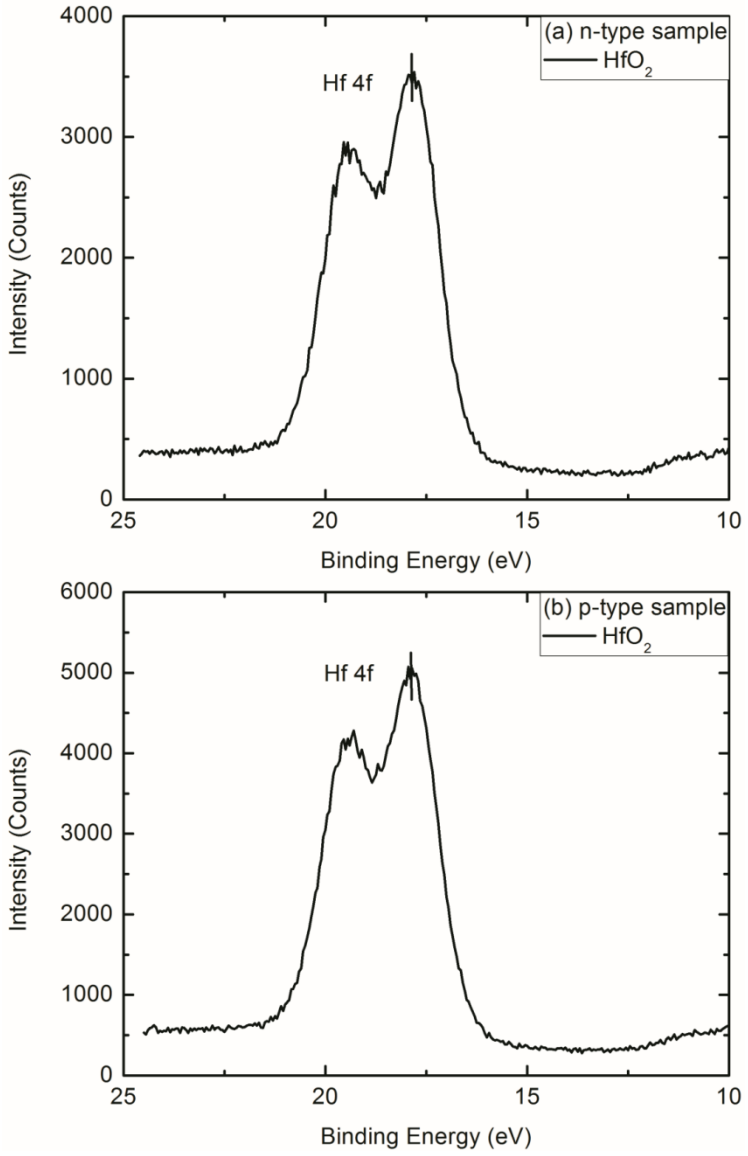

Figure 3.3 X-ray photoemission spectra of Hf 4f peaks for HfO_2 and VO_2 on (a) oxidized *n*-type Si(100) substrate and (b) *p*-type Si(100) substrate.

3.4.4 Ultraviolet photoemission spectra

The ultraviolet photoemission spectra of the cleaned, oxidized substrate, after VO_2 deposition, and after HfO_2 deposition for both *n*- and *p*-type substrates are shown in Fig. 3.4. The UPS spectrum of the initial clean SiO_2 layer on *n*-type and *p*-type Si substrates show the valence band maximum (VBM) at 5.5 eV and 5.0 eV below the Fermi level. The valence band offset between Si and SiO_2 is then 4.5 eV for the *n*-type Si substrate, which agrees with previous results for the Si-SiO_2 band offset [22]. These results are consistent with a low interface state density and negligible band bending for the *n*-type substrate. For the *p*-type substrate, there is an ~0.4 eV inconsistency between the XPS and UPS results for the determination of the VBM of the SiO_2. Given the sensitivity of UPS measurements, we have used the XPS results to determine the relative band positions for the SiO_2. For the VO_2 film, the V 3d peak is close to the Fermi level, and the cutoff of this peak gives the valence band maximum at 0.6 eV below the Fermi level for both *n*- and *p*-type substrates, respectively. After the 2.0 nm HfO_2 layer deposition, the front cutoff of the UPS spectra indicates the valence band maximum relative to the Fermi level at 4.0 eV for both of the *n*-type and *p*-type sample.

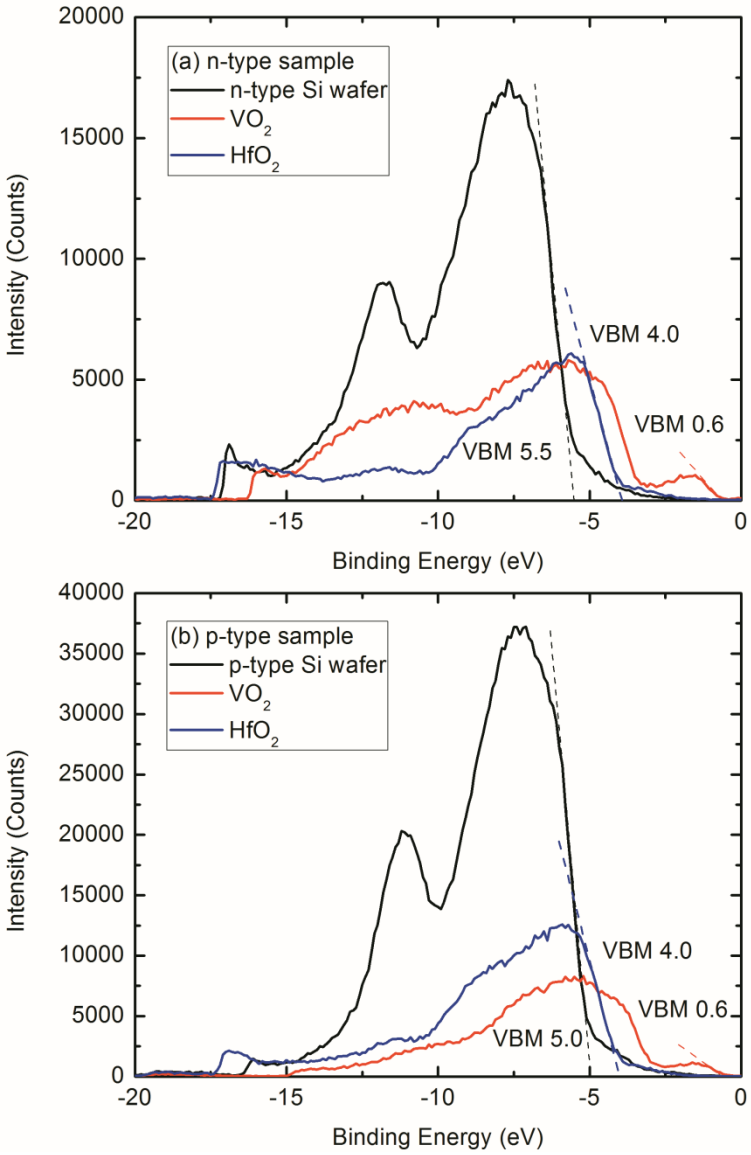

Figure 3.4 Ultraviolet photoemission spectra of (a) plasma oxidized *n*-type Si(100), (b) vanadium oxide on oxidized *n*-type Si(100) and (c) HfO_2 and VO_2 on oxidized *n*-type Si(100).

3.4.5 Transmission electron microscopy

Fig. 3.5 displays a cross-sectional electron micrograph of the *n*-type sample structure. The VO_2 and HfO_2 layers are ~ 1.6 nm and 1.9 nm in thickness,

respectively. The final SiO_2 layer is ~1.3 nm suggesting that the thickness increased due to substrate oxidation during the higher temperature growth of the VO_2 layer. This is also consistent with the XPS results. From Fig 3.1, the ratio (I_{SiO2}^{exp}/ I_{Si}^{exp}) of XPS intensities is calculated as 26% for the initial oxidized *n*-type substrate which increases to 41% for the final *n*-type sample. The corresponding values are 21% for the initial oxidized *p*-type substrate which increases to 73% for the final *p*-type sample. Both results indicate that the SiO_2 layer became thicker after deposition of the oxide layers. There is no evidence of crystalline order or domains in any of the oxide layers. The contrast of each oxide layer is uniform and changes sharply at the Si/SiO_2, SiO_2/VO_2, and VO_2/HfO_2 interfaces. The results indicate an amorphous structure and sharp interfaces without evidence of intermixing.

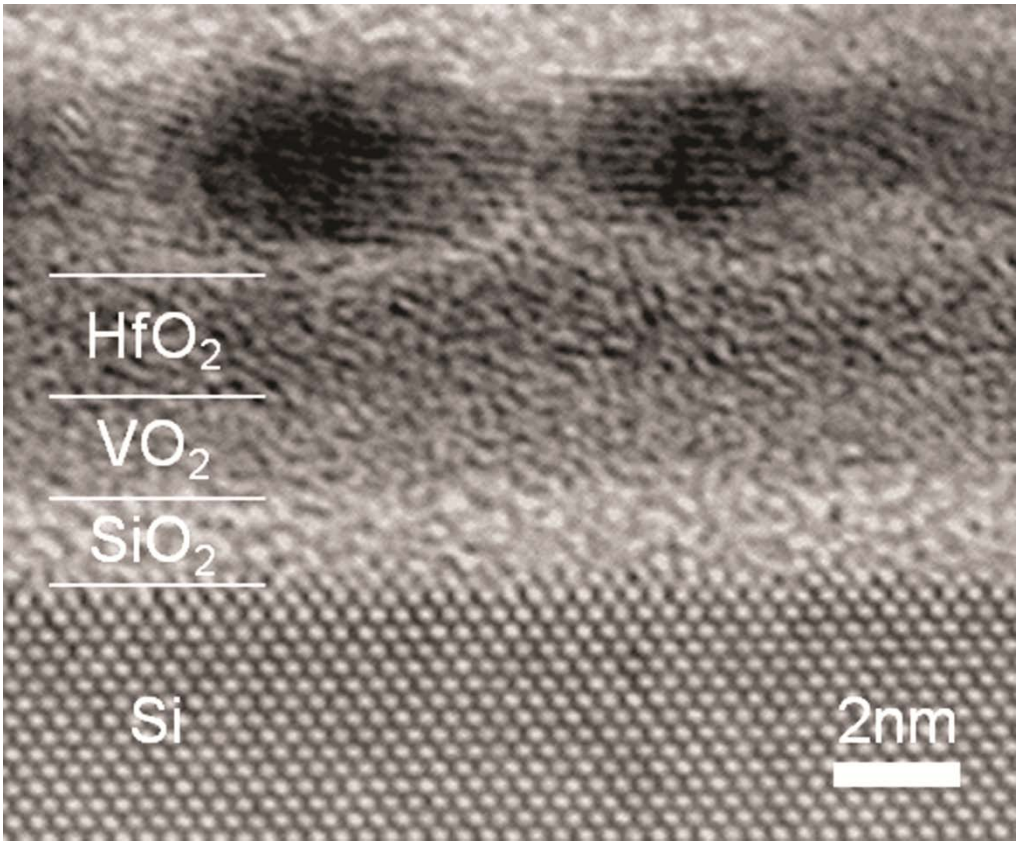

Figure 3.5 Cross sectional TEM image of the $HfO_2/VO_2/SiO_2$ structure on *n*-type Si. A Pt capping layer was employed to protect the surfaces during specimen preparation.

3.5 Discussion

3.5.1 Valence band offset

In our study, we employ UPS to determine the VBM and XPS to measure the core level energies both with respect to the Fermi energy. For the *p*-type sample, we adopt the value derived from XPS data for the initial band conditions. The valence band offset (VBO) of VO_2 and SiO_2 can be expressed in method (3.1) as:

$$VBO = E_{VBM}^{SiO2} - E_{VBM}^{VO2} - \Delta^{Si} - \Delta^{SiO2}, \quad (3.1)$$

where E_{VBM}^{SiO2} and E_{VBM}^{VO2} are the VBM (relative to the Fermi level) of the initial clean oxidized Si substrate (SiO_2 layer) and the VO_2 layer obtained by UPS, respectively. The Δ^{Si} is the change of band bending of the Si substrate, and Δ^{SiO2} is the change of electric potential across the SiO_2 layer both after VO_2 layer deposition. From Equation 3.1 and Table 3.3(a), the VBO of VO_2/SiO_2 is calculated as 4.0 ± 0.1 eV and 4.0 ± 0.1 eV for films on the *n*- and *p*-type Si substrate, respectively.

The band offset (VBO) of VO_2 and SiO_2 can also be expressed in method (3.2) as:

$$VBO = (E_{2p3/2}^{VO2} - E_{VBM}^{VO2}) - (E_{2p}^{SiO2} - E_{VBM}^{SiO2}) - \Delta1(E_{2p3/2}^{VO2} - E_{2p}^{SiO2}) - \Delta2(SiO_2), \quad (3.2)$$

where $(E_{2p3/2}^{VO2} - E_{VBM}^{VO2})$ is the V 2p3/2 core level to VBM of VO_2, $(E_{2p}^{SiO2} - E_{VBM}^{SiO2})$ is the Si 2p core level to VBM of SiO_2, $\Delta1(E_{2p3/2}^{VO2} - E_{2p}^{SiO2})$ is the energy separation between the V 2p3/2 of VO_2 and Si 2p of SiO_2, and $\Delta2(SiO_2)$ is the electrical potential across the SiO_2 layer. From Equation 3.2 and Table 3.3(b), the VBO of VO_2/SiO_2 is calculated as 4.0 and 4.0 eV for the *n*-type and *p*-type Si substrates, respectively. The values of the VBO of VO_2/SiO_2 calculated from the two methods are then consistent.

Table 3.3. Tabulated electronic structure for VO_2 on Si substrate, including (a) VBM of SiO_2 and VO_2, the change of band bending (Δ^{Si}), the electrical potential change on SiO_2 layer (Δ^{SiO2}), and valence band offset (VBO), (b) V 2p3/2 core

level to VBM of VO_2 ($E_{2p3/2}^{VO2} - E_{VBM}^{VO2}$), Si 2p core level to VBM of SiO_2 ($E_{2p}^{SiO2} - E_{VBM}^{SiO2}$), energy separation between V 2p3/2of VO_2 and Si 2p of SiO_2 ($\Delta 1$), and electrical potential change from the mid of SiO_2 layer to the interface of VO_2/SiO_2, ($\Delta 2$). For the *p*-type sample, we adopt the value derived from XPS data for the initial band conditions.

(a)	VBM SiO_2 (eV)	VBM VO_2 (eV)	Δ^{Si} (eV)	Δ^{SiO2} (eV)	VBO (eV)
n-type	5.5	0.6	0.3	0.6	4.0
p-type	4.6	0.6	0.0	0.0	4.0

(b)	*n*-type	*p*-type
($E_{2p3/2}^{VO2} - E_{VBM}^{VO2}$) (eV)	515.4 (516.0 – 0.6)	515.6 (516.2 – 0.6)
($E_{2p}^{SiO2} - E_{VBM}^{SiO2}$) (eV)	98.1 (103.6 – 5.5)	98.6 (103.2 – 4.6)
$\Delta 1$ ($E_{2p3/2}VO_2$ - $E_{2p}SiO_2$) (eV)	413.0 (516.0 – 103.0)	413.0 (516.2 – 103.2)
$\Delta 2$ (SiO_2) (eV)	0.3	0.0
VBO (eV)	4.0	4.0

The interfacial dipole is calculated as the difference between the vacuum levels of the two adjoining materials, which can be expressed as:

$$\Delta Dipole = (h\nu - W^{SiO2}) - (h\nu - W^{VO2}) - VBO^{SiO2/VO2} = W^{VO2} - W^{SiO2} - VBO^{SiO2/VO2}, \quad (3.3)$$

where $h\nu$=21.2 eV is the He I photon energy, W represents the width of UPS spectra, for SiO_2 as 11.7 eV, VO_2 as 15.6 eV, and HfO_2 as 13.4 eV from the *n*-

type sample measurements, respectively. Because the spectra for the *n*-type sample were of high quality at both the low and high energy cutoffs, these values have been adopted for both the *n*- and *p*-type samples. Here (hν –W) is the energy of the vacuum level relative to the VBM, and $VBO^{SiO2/VO2}$ is the SiO_2/VO_2 valence band offset. The VO_2/SiO_2 interfacial dipole can be calculated as 0.1 eV on the *n*- and *p*-type Si substrate. Similarly, The HfO_2/VO_2 interfacial dipole can be calculated as 1.2 eV on the *n*-type Si substrate and 1.1 eV on the *p*-type Si substrate. This indicates the electron affinity model only describes the band offset of the VO_2/SiO_2 interface well, indicating a small interfacial dipole, but it is less consistent for the whole $HfO_2/VO_2/SiO_2/Si$ bands.

Robertson [23] has developed a model which presumes that the charge will transfer and align the charge neutrality levels (CNL) at the interface. The CNL of HfO_2 as calculated by LDA is 3.7 eV and the CNL of SiO_2 is calculated as 4.5 eV [24]. According to the CNL model, the valence band offset of HfO_2/SiO_2 is expected to be 0.8 eV without a VO_2 interlayer. Considering the valence band offset of VO_2/SiO_2 is measured as 4.0 eV, the valence band offset of HfO_2/VO_2 is predicted as 3.2 eV by the CNL model. Our results show that for the n-type and p-type substrate, the VBM of HfO_2 is 4.0 eV, and the VBM of VO_2 is 0.6 eV. The valence band offset for HfO_2/VO_2 is determined as 3.4 eV, which is comparable to the predicted 3.2 eV value.

We consider now the relative band alignment of HfO_2 on SiO_2 on Si without and with the VO_2 inter-layer. The valence band offset of HfO_2/SiO_2 from previous experimental results was found to be 1.05 ± 0.1 eV [25]. In this study

the relative band offset of the HfO_2/SiO_2 with the VO_2 interlayer is found to be 0.8 eV for the *n*-type substrate and 0.6 eV for the *p*-type substrate. Thus it appears that both the VO_2/SiO_2 and HfO_2/VO_2 interfaces have the same origin of the interface dipole. Robertson has noted that the CNL model would predict a VBO of 0.8 eV for HfO_2/SiO_2 without a VO_2 interlayer. This result indicates that the CNL model describes the band offset of the $HfO_2/VO_2/Si$ substrate system.

3.5.2 Band alignment schematics

Fig. 3.6 shows diagrams of the band alignment for the different stages of development of the *n*-type sample structure. According to the XPS and UPS analysis, the band bending at the SiO_2/Si interface is less than the 0.1 eV resolution limit of the measurement, which indicates the substrate is at a flat band condition. Assuming the 0.1 eV value as a limit, the interface charge density is less than 3.6×10^{11} cm^{-2}. Considering the 1.1 eV band gap of Si and the 8.9 eV band gap of SiO_2, the conduction band alignment for the oxidized *n*-type Si substrate is also shown in Fig. 3.6(a). After deposition of the 2 nm VO_2 layer, the bulk Si core level shifts to lower binding energy by ~0.3 eV, indicating upwards band bending. The Si core level in the SiO_2 layer shifts to lower binding energy by ~0.6 eV, indicating an electric potential across the SiO_2 layer. Subtracting the Si core level shift (band bending), the potential across the SiO_2 layer is 0.6 V (2× (0.6 – 0.3) V). Using 0.8 nm for the thickness of the SiO_2, the electric field across the SiO_2 layer is 7.5×10^8 V/m. It is presumed that there is no significant electric field across the low band gap vanadium oxide layer. According to the UPS results, the VBM of VO_2 is 0.6 eV below the Fermi level. Considering the band

gap of VO_2 as 0.7 eV, the band alignment of the two oxide layer structure is shown in Fig. 3.6(b). It is noted that the CBM for all of the oxides are deduced from the reported values of the band gap, and the CBM are shown as dashed lines in the figures. After deposition of the 2 nm HfO_2 layer, the Si 2p peaks of the Si and SiO_2 shift back to 99.6 eV and 103.2 eV, respectively. A slight upwards band bending is indicated for the Si wafer, and the potential across the SiO_2 is 0.6 V. The V 2p3/2 peak shifts from 516.0 to 515.6 eV, an ~0.4 eV shift. According to the UPS results, the VBM of HfO_2 is 4.0 eV below the Fermi level. Considering the VBM of VO_2 at 0.6 eV below the Fermi level and assuming a negligable field across the VO_2 layer, the VBO of HfO_2/VO_2 is determined as 3.4 eV. Considering the band gap of HfO_2 as 5.7 eV, the band alignment of the final structure is shown in Fig. 3.6(c).

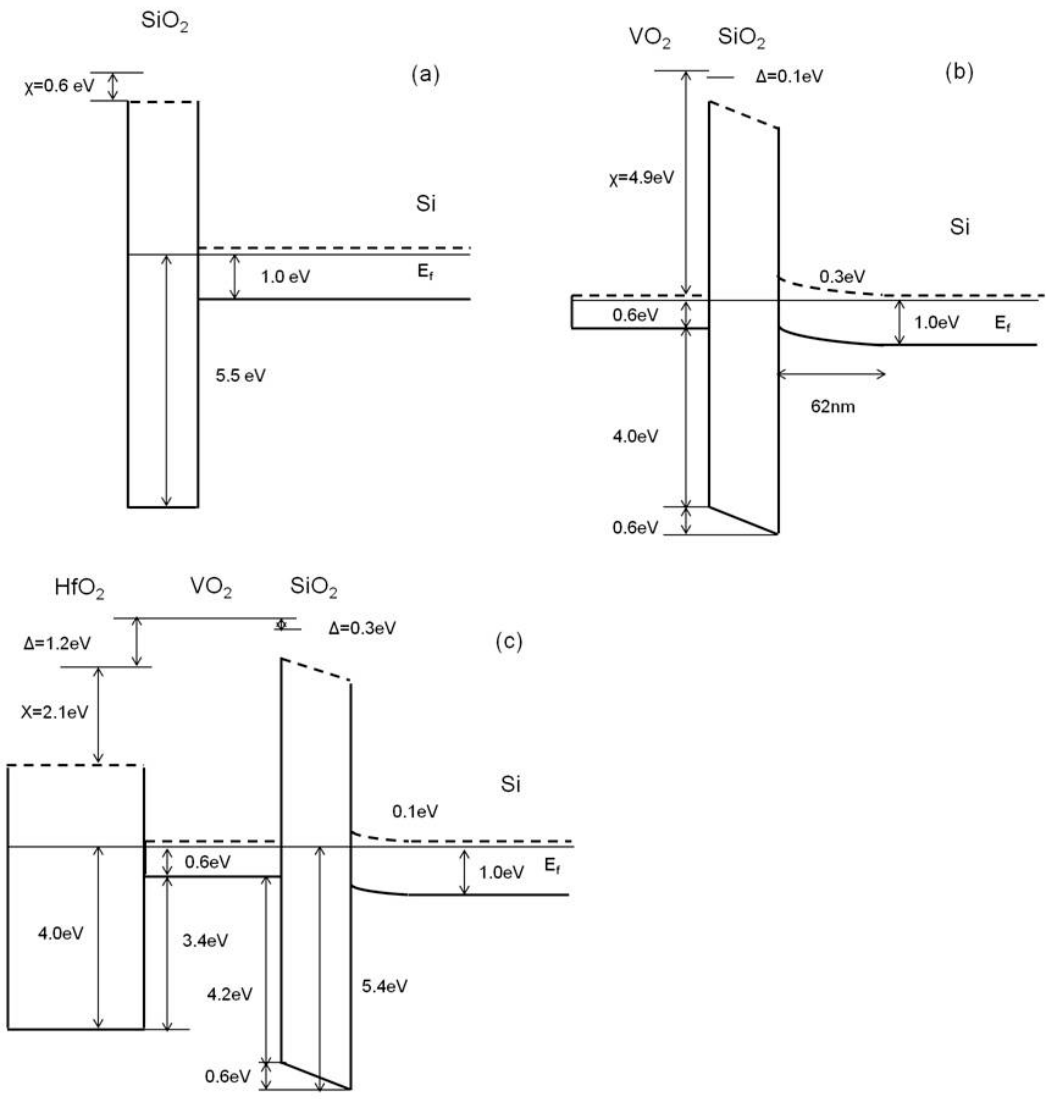

Figure 3.6 Band alignment of (a) plasma oxidized *n*-type Si(100), (b) VO_2 on oxidized *n*-type Si(100) and (c) HfO_2 and VO_2 on oxidized *n*-type Si(100). Dashed lines are used to represent the conduction band minimum of the oxides which are deduced from reported values of the band gap. Distances approximately represent the experimental film thickness except the depletion region in the Si which is compressed as indicated.

Fig. 3.7 shows the band alignment diagrams for the different stages of development of the *p*-type sample structure. Considering the 1.1 eV band gap of Si, the 8.9 eV band gap of SiO_2 and the 4.5 eV band offset at the Si/SiO_2 interface, the band alignment for the oxidized *p*-type Si substrate is shown in Fig. 3.7(a). According to the XPS data analysis, the oxidized *p*-type Si substrate is at a flat band condition. After deposition of the 2 nm VO_2 layer, the bulk Si core level at the SiO_2/Si interface remains at the same position as the oxidized Si substrate. In this case, after the VO_2 deposition, the Si substrate is still at a flat band condition. Again, it is also presumed that there is no significant electric field across the vanadium oxide layer. According to the UPS results, the VBM of VO_2 is 0.6 eV below the Fermi level. The band alignment of these two oxide layers is shown in Fig. 3.7(b). After deposition of the 2 nm HfO_2 layer, the bulk Si core level at the SiO_2/Si interface and the Si core level of the SiO_2 shift to higher binding energies of 99.1 eV and 103.2 eV, respectively. Considering the 0.1 eV uncertainty, the substrate remains at the initial flat band condition. According to the UPS results, the VBM of HfO_2 is 4.0 eV below the Fermi level. Considering the VBM of VO_2 at 0.6 eV below Fermi level and assuming a negligible field across the VO_2 layer, the VBO of HfO_2/VO_2 is determined as 3.4 eV. The band alignment of the final structure is shown in the Fig. 3.7(c).

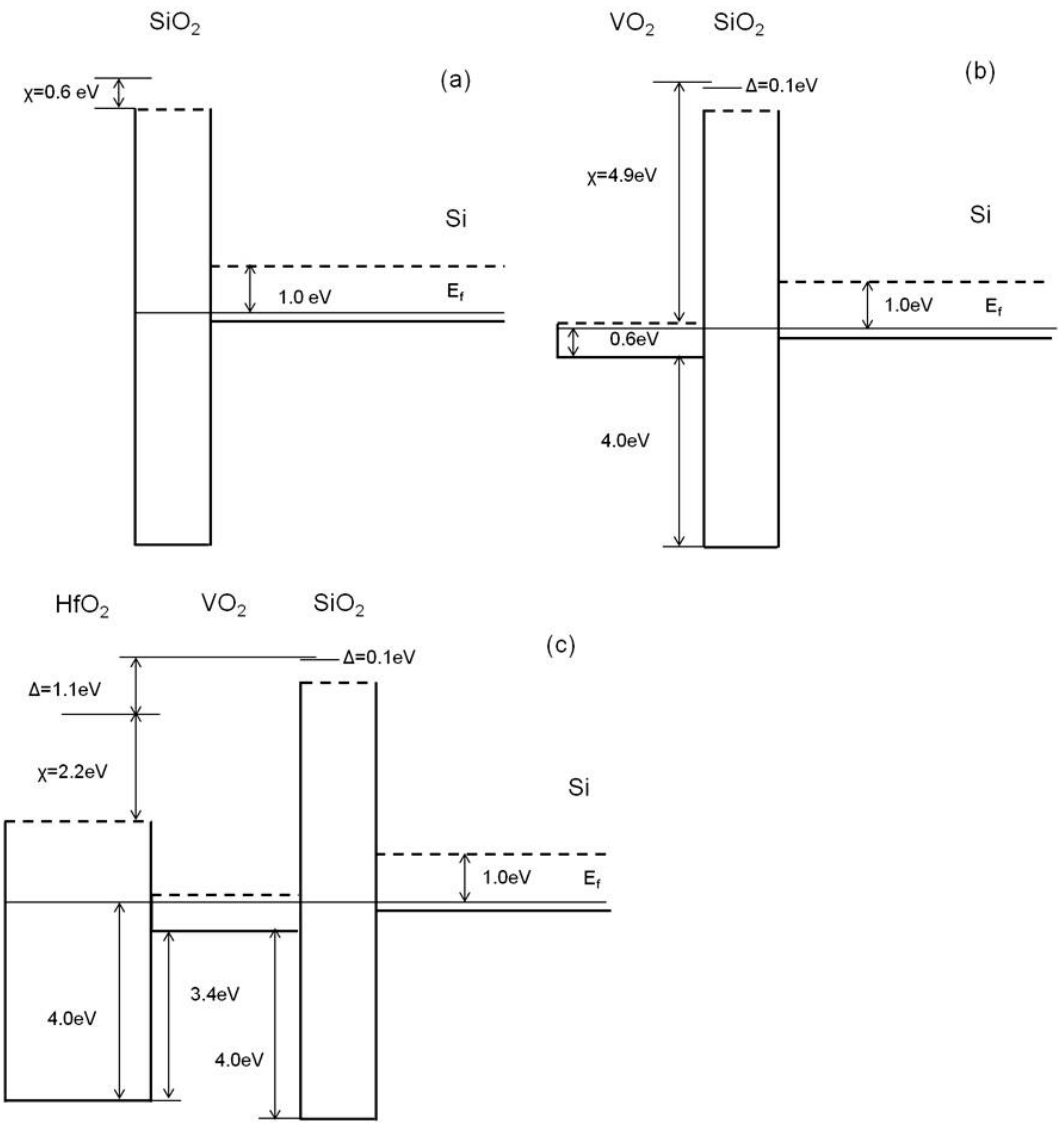

Figure 3.7 Band alignment of (a) plasma oxidized *p*-type Si(100), (b) VO_2 on oxidized *p*-type Si(100) and (c) HfO_2 and VO_2 on oxidized *p*-type Si(100). Dashed lines are used to represent the conduction band minimum of the oxides which are deduced from reported values of the band gap.

The results show the development of the band alignment for the HfO_2, VO_2 and oxidized Si substrate. Charges presumably due to defects in the oxide layers affect the band alignment which changes during growth. The VO_2/SiO_2

interface traps negative charges after the VO_2 deposition for the *n*-type sample. The fact that the VO_2 CBM is near the Fermi level enables accommodation of excess positive or negative charges. The upwards band bending of the *n*-type Si substrate indicates these positive charges accumulate at the depletion region near the interface. For both *n*- and *p*-type substrates, the band offset between the VO_2 layer and SiO_2 layer is measured as 4.0 ± 0.1 eV.

3.6 Conclusions

A gate stack structure has been prepared with HfO_2 and an ultra thin VO_2 layer on oxidized Si substrates. The films were developed by reactive e-beam deposition on oxidized *n*- and *p*-type substrates. The TEM analysis confirmed the layer structure and indicated sharp interfaces without evidence of interdiffusion. The band alignment for this gate stack structure was deduced from *in-situ* XPS and UPS spectra. A band offset of 4.0 ± 0.1 eV was measured between an ultra thin VO_2 layer and the SiO_2 layer. After the HfO_2 capping layer deposition, only small changes in the band alignment are observed. The band offset between the HfO_2 and VO_2 is 3.4 ± 0.1 eV. The relative band offset between the HfO_2 and SiO_2 with a VO_2 interlayer is 0.7 ± 0.1 eV which is comparable to the value without a VO_2 inter-layer. The results also show charge transfer to the VO_2 for growth on the *n*-type substrate. The band diagram for this gate stack structure shows a confined-well band structure, demonstrating the potential for charge storage for the embedded VO_2 layer.

REFERENCES

[1] C.N. Berglund and H.J. Guggenheim, Phys. Rev. 185, 1022 (1969).

[2] S. Ormoz and S. Ramanathan, Solid State Electronics 54, 654-659 (2010).

[3] R. Lopez, L.A. Boatner, T.E. Haynes, R.F. Haglund, and L.C. Feldman, Appl. Phys. Lett. 79, 3161 (2001).

[4] F.J. Morin, Phys. Rev. Lett. 3, 34 (1959).

[5] M.W. Haverkort, Z. Hu, A. Tanaka, W. Reichelt, S.V. Streltsov, M.A. Korotin, V.I. Anisimov, H.H. Hsieh, H.J. Lin, C.T. Chen, D.I. Khomskii and L.H. Tjeng, Phys. Rev. Lett. 95, 196404 (2005).

[6] S. Biermann, A. Poteryaev, A. I. Lichtenstein, and A. Georges, Phys. Rev. Lett. 94, 026404 (2005).

[7] Koji Kousge, J. Phys. Chem. Solids Pergamon Press, 28, 1613-1621 (1967).

[8] G.S. Nadkarni and V.S. Shirodkar, Thin Solid Films, 105, 115-129 (1983).

[9] A. Cavelleri, C. Toth, C.W. Siders, J.A. Squier. Phys. Rev. Lett. 87, 237402 (2001).

[10] Hyun-Tak Kim, Yong Wook Lee, Bong-Jun Kim, Byung-Gyu Chae, Sun Jin Yun, Kwang-Yong Kang, Kang-Jeon Han, Ki-Ju Yee and Yong-Sik Lim, Phys. Rev. Lett. 97, 266401 (2006).

[11] S. Hormoz, S. Ramanathan, Solid State Electronics 54, 654-659 (2010).

[12] G.D. Wilk, R.M. Wallace, J.M. Anthony, J. Appl. Phys, 89, 5243 (2001).

[13] T. Yasuda, Y. Ma, S. Habermehl, and G. Lucovsky, J. Vac. Sci. Technol. B 10, 1844 (1992).

[14] D.A. Cole, J.R. Shallenberger, S.W. Novak, R.L. Moore, M.J. Edgell, S.P. Smith, C.J. Hitzman, J.F. Kirchhoff, E. Principe, W. Nieveen, F.K. Huang, S.Biswas, and K. Jones, J. Vac. Sci. Technol. B 18, 440-444 (2000).

[15] D. Rob and M. Maier, Fresenius J. Anal. Chem. 333, 488 (1989).

[16] M. F. Hochella and A. F. Carim, Surf. Sci. Lett. 197, L260 (1988).

[17] F. Yano, A. Hiraoka, T. Itoga, H. Kojima, K. Kanehori, and Y. Mitsui, J. Vac. Sci. Technol. A 13, 2671 (1995).

[18] Z.H. Lu, J.P. McCaffrey, B. Brar, G.D. Wilk, R.M. Wallace, L.C. Feldman, and S.P. Tay, Appl. Phys. Lett. 71, 2764 (1997).

[19] J. R. Shallenberger, D. A. Cole and S. W. Novak, J. Vac. Sci. Technol. A 17, 1086 (1999).

[20] C.C. Fulton, G. Lucovsky, and R.J. Nemanich, J. Vac. Sci. Technol. B20, 1726 (2002).

[21] J. Mendialdua, R.Casanova, and Y. Barbaux, J. Electron Spectrosc. Relat. Phenom. 71, 249 (1995).

[22] J.W. Keister, J.E. Rowe, J.J. Kolodziej, H. Niimi, T.E. Madey, and G.Lucovsky, J. Vac. Sci. Technol. A 17, 1250 (1999).

[23] J. Robertson, J. Vac. Sci. Technol. B 18, 1785 (2000).

[24] Yee-Chia Yeo, Tsu-Jae King, and Chenming Hu, J. Appl. Phys, 92, 7266 (2002).

[25] S. Sayan, E. Garfunkel and S. Suzer, Appl. Phys. Lett. 80, 2135 (2002).

Chapter 4

LOW TEMPERATURE GROWTH OF HIGH-K HF-LA OXIDES BY REMOTE-PLASMA ATOMIC LAYER DEPOSITION: MORPHOLOGY, STOICHIOMETRY, AND DIELECTRIC PROPERTIES

This work is collaborated with Dr. Fu Tang.

My contribution is the data analysis and the paper writing.

4.1 Abstract

In this work, we investigated the growth of Hf oxide, La oxide, and alloyed Hf-La oxide films using remote-plasma atomic layer deposition (RPALD) at temperatures ranging from ~80°C to ~250 °C. The relative composition and atomic bonding structure of the film were determined by in situ x-ray photoelectron spectroscopy (XPS). Atomic force microscopy (AFM) and transmission electron microscopy (TEM) were implemented to characterize the morphology and crystalline structure. The XPS results indicated that for low temperature Hf oxide growth, a significant amount of excess oxygen species was observed in the deposited film. This oxygen could lead to instabilities and adversely affect the function of thin film transistors (TFTs). We established that a He plasma post deposition treatment can partially remove the excess oxygen. In addition, the pure Hf oxide films show a surface morphology with protruding islands over a smooth surface which reflects the crystallized nature of the Hf oxide domains. In order to suppress the crystallization of the Hf oxide and to obtain a smooth morphology, 1-3 cycles of La-oxide were employed between adjacent Hf-oxide cycles. The Hf-La oxide films showed reduced roughness

compared with that of the pure Hf oxide film. Carbon residue in the alloyed film is also reduced compared with that of the La oxide film. Finally, the electrical properties of the deposited films were characterized by capacitance-voltage (C-V) and current-voltage (I-V) measurement. The I-V curves show that the alloyed Hf-La oxide films have a higher break down field than that of pure Hf oxide films.

4.2 Introduction

High-k oxides have been widely employed in Si-based nanoscale transistors in order to reduce the gate tunneling current and energy consumption.[1, 2] Recently, the application of high-k dielectrics is also emerging in other semiconductor areas including thin film transistors (TFTs) for flexible electronics. A high-k gate dielectric layer can significantly reduce the threshold voltage, increase the on/off current ratio and enhance the mobility of TFTs. [3] One of the limiting factors in implementing high-k materials for flexible electronics is the development of a low temperature deposition process.

Plasma-enhanced atomic layer deposition (PEALD) [4-7] has been considered as a promising approach for deposition of high-k dielectrics at low temperatures. Atomic layer deposition (ALD) is a self-limiting growth method, where growth is achieved by alternatively pulsing precursors into the deposition chamber. [8,9] The advantages of ALD include conformal coating, thickness uniformity, and composition and stoichiometry control. In PEALD, the excess activated oxygen species generated by the plasma can significantly reduce the deposition temperature and produce a denser film and potentially a lower defect concentration. In order to minimize the effects of the defects and excess species,

studies up to now have focused on films deposited at high temperature or treated with high temperature annealing.[4,6,7] Neither process is appropriate for flexible substrates.

In this study, we have systematically investigated the properties of as-deposited Hf oxide, La oxide, and Hf-LaO_x films using remote plasma atomic layer deposition (RPALD) at temperatures ranging from ~80°C to ~250 °C. Ion induced effects can be neglected because of the low ion density of the remote plasma treatment. The film bonding and composition were characterized with in situ X-ray photoemission spectroscopy (XPS); the morphology was characterized with atomic force microscopy; the crystalline structure was determined from cross section transmission electron microscopy (TEM); and the electrical properties were deduced from capacitance-voltage (C-V) and current-voltage (I-V) measurements. We found that a significant amount of excess oxygen species is observed for the Hf oxide film at low deposition temperature, which can be partially removed by a post He plasma treatment. In addition, by alloying with La, the morphology and electrical properties of the oxide film were improved.

4.3 Experiment

The substrates used in this study are ambient oxidized n-type Si (100) wafers. Prior to loading the substrates into the vacuum chamber, the wafers were ultrasonically cleaned in acetone and methanol for ~15 minutes duration for each process. The deposited samples were transferred to an XPS chamber through an ultra high vacuum (UHV) transfer line which enables in situ measurement without introducing contamination. The high-k oxide films were deposited using a custom

computer controlled RPALD system. The base pressure of the chamber was ~1.0 $\times 10^{-8}$ Torr from the turbo-drag pump backed with a dry diaphragm pump. After the 0.1 s precursor pulse, the pressure increases to ~800 - 900 mTorr. Nitrogen gas was introduced for 10s to purge any excess precursor. After the nitrogen purge, oxygen was introduced into the chamber for 6 s, and then excited by rf-power for 2-20 s. The pressure in the chamber during deposition was controlled by a throttle valve to a value of ~110 mTorr. The stainless steel bubbler containing the Hf precursor (Tetrakis(ethylmethylamino)hafnium(IV)) was maintained at ~70 ºC during deposition. For the lanthanum oxide growth, the precursor Tris(isopropylcyclopenta-dienyl)lanthanum was heated to a temperature of ~168 ºC. The chamber and gas lines were heated to ~100 °C to avoid precursor condensation. The remote plasma was excited with 13.56 MHz rf-power applied to a helical copper coil wound around a 32mm dia. quartz tube that opens toward the sample. In these experiments the plasma power was varied from 80 to 200 W. The post-deposition He plasma treatment was excited with 35 W for a typical duration of ~20 minutes. Because of the remote plasma excitation without sample bias, the sample is exposed to free radicals and excited molecules and a very low density of ions.

After deposition, the pressure was reduced in the deposition chamber, and the sample was transferred to the XPS system through the UHV linear transfer chamber. XPS characterization is performed at a base pressure of 6×10^{-10} Torr using the 1253.6 eV Mg Kα line of a VG XR3 source and a VG microtech Clam II analyzer operated at a resolution of 0.1 eV. The films for XPS analysis were

~3-5 nm thick, and our prior studies have established that charging effects can be neglected because of tunneling to the conducting Si substrates.

An Agilent 5500 AFM was used to characterize the morphology of the deposited films under tapping mode with silicon tip. Representative samples were observed in cross-section geometry using a JEOL JEM 4000EX high-resolution electron microscope operated at 400 kV. The electrical properties of the oxide films were investigated by capacitance voltage (C-V) and current voltage (I-V) measurements using a mercury probe station system (MSI Electronics Mercury Probe Hg412-3).

4.4 Results and discussion

4.4.1 Hafnium oxide films

a) Oxygen species

Figure 4.1 shows the XPS scan of the Hf oxide films grown on Si substrates at different temperatures. From the curves, we find that the O 1s features can be fitted with two peaks. The peak at ~530 eV is attributed to oxygen in the Hf oxide. The other peak has a higher binding energy at ~532 eV, which has been attributed to the presence of excess oxygen species.[10,11] These species may include molecular oxygen or bound hydroxyl groups. At lower deposition temperatures the peak from the excess species dominates the spectrum, while at higher temperatures, this peak is significantly reduced.

Figure 4.1(d) presents a quantitative analysis of the oxygen 1s peak area from Hf oxide (I_1) and the excess oxygen (I_2). Here, I_1 or I_2 are obtained from the integrated peak area divided by the atomic sensitivity factor, and each peak area

has been normalized to the integrated area of the Hf 4f peaks. As the deposition temperature increases, I_1 increases, suggesting increased stoichiometric bonding of the Hf and oxygen. Conversely, I_2 from absorbed oxygen is reduced as the temperature is increased. The results suggest that the precursor may be not fully oxidized at low growth temperature. In addition, excess oxygen molecules or OH are weakly bonded in the film which may limit the efficiency of the atomic oxygen in the plasma. At high growth temperature, the excess oxygen species desorb, resulting in a more completely oxidized film, and the XPS is dominated by a single, narrower peak.

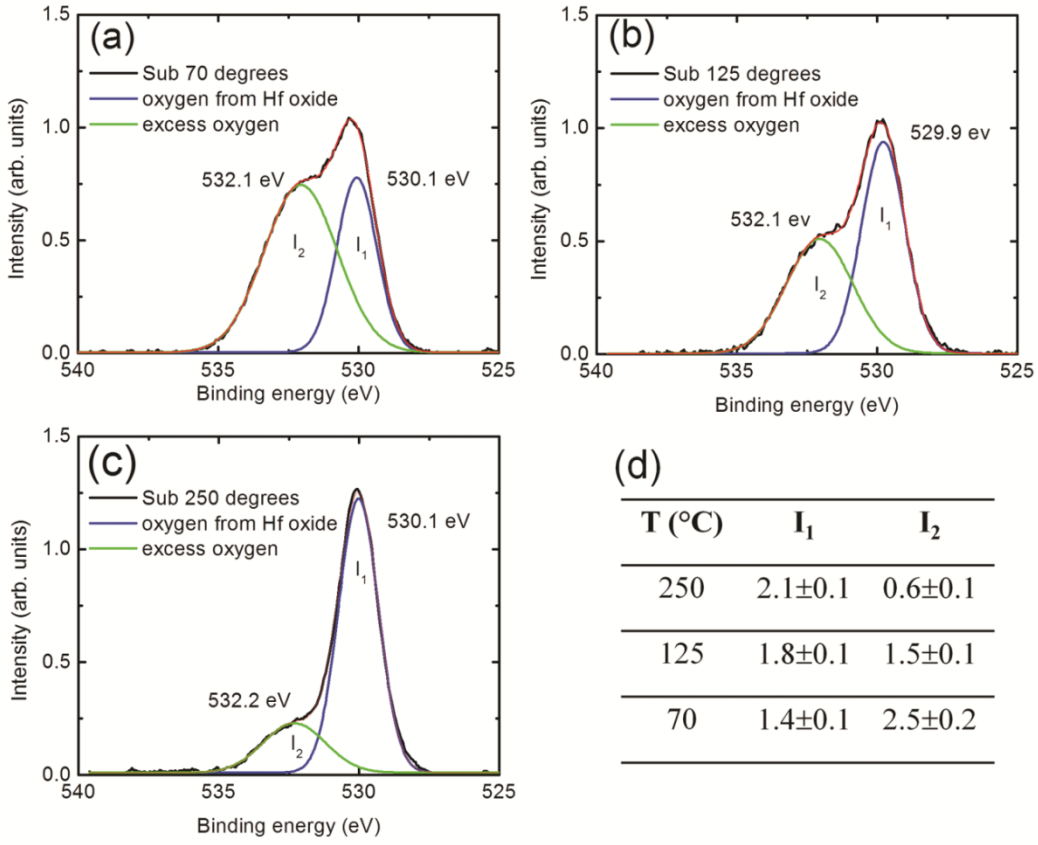

(d)

T (°C)	I_1	I_2
250	2.1±0.1	0.6±0.1
125	1.8±0.1	1.5±0.1
70	1.4±0.1	2.5±0.2

Figure 4.1. XPS O 1s spectra for Hf oxide deposited at substrate temperatures of: (a) 70 °C, (b) 125 °C, and (c) 250 °C. The normalized O peak area (d) from Hf

oxide (I_1) and excess oxygen (I_2) at different temperatures.

b) Post He-plasma treatment

The presence of excess oxygen may adversely affect the stability and function of TFTs. For example, the excess oxygen has been shown to form an electron surface accumulation layer which reduces the mobility of the ZnO channel layer.[12,13] As already noted thermal approaches employed to reduce the excess species include increasing the growth temperature or annealing the film after growth. However, for flexible electronics applications, increased temperature methods are limited because of the substrate thermal stability. An alternative method, which has been demonstrated on zinc oxide, is to expose the film to ultraviolet (UV) light.[14] Here, we have employed a He plasma post-deposition exposure which generates UV light dominated by ~21.2 eV photons. Figure 4.2 shows the Hf and oxygen XPS peaks before and after He plasma treatment. We find that the excess oxygen peak is indeed decreased as most molecular oxygen is removed by He plasma treatment. However, the narrow oxygen peak may come from the oxygen in residue bound hydroxyl groups. Accompanying the oxygen reduction, the binding energies of both the Hf and O peaks shift by ~1.4 eV to higher values. As the thickness of this sample is estimated as ~3 nm, the charging effect can be neglected.

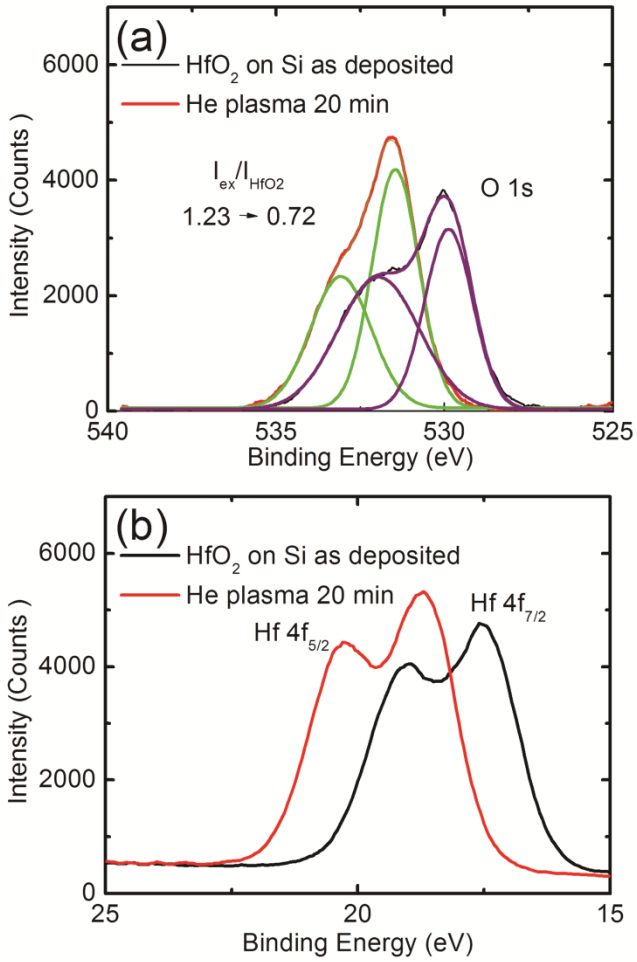

Figure 4.2. XPS spectra of (a) O 1s, and (b) Hf 4f peaks, for as-deposited Hf oxide film and post He-plasma processed film.

Figure 4.3 presents a schematic of the proposed mechanism for photo-induced desorption of the excess species in the oxide films. The presence of the excess oxygen in the film leads to sites which can accept negative charges. Thus, there will be negative charge distributed through the film, which forms a dipole structure with the positive charge in the Si substrate. This charge distribution will produce an electric field across the oxide as has been described in prior work from our laboratory.[15] The UV photons in the He plasma can penetrate ~13nm into

the oxide which can induce desorption through the thickness of the film which reduces the sites available for charge transfer and the electric field across the oxide. This is consistent with the binding energy shift to higher values as observed from the XPS measurements. The XPS measurements also show that the excess oxygen is only partially released. This could be due to the fact that molecular oxygen species can be released through photo-induced desorption while other species such as hydroxyl groups still remain due to stronger bonding with the oxide.

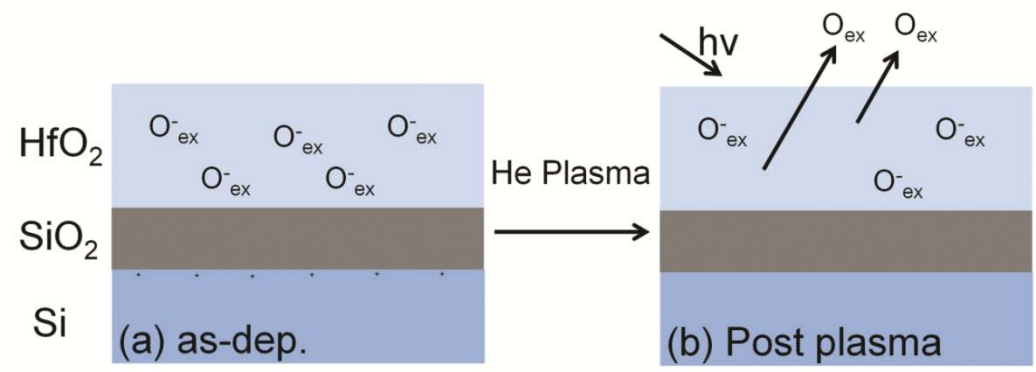

Figure 4.3. Schematic of the proposed mechanism for oxygen desorption induced by the He plasma process: (a) the excess oxygen in the as-deposited Hf oxide film; and (b) oxygen desorbed from the film during ultraviolet light (UV) illumination generated from the He plasma.

c) Morphology

In addition to the excess oxygen species in the Hf oxide films, AFM measurements show that the morphology of the Hf oxide film also has some undesired features. Figure 4.4 presents topography images of films deposited at different plasma conditions (a) 80 W with a 8 s oxygen plasma pulse, and (b) 20

W with a 2 s oxygen plasma pulse. The morphology of both films showed similar features: a number of protruding islands extending beyond the smooth surface. The average thickness of the films is ~10 nm, however, the peak-valley height can reach ~20 nm. In the case of high oxygen plasma power and long plasma exposure, the density of protruding islands was slightly increased. These protruding islands are presumed to be crystallized grains, as found by Hausmann et al.[16] Even with the plasma power reduced to 20 W and a short exposure time of 2 s, significant crystallization was still detected.

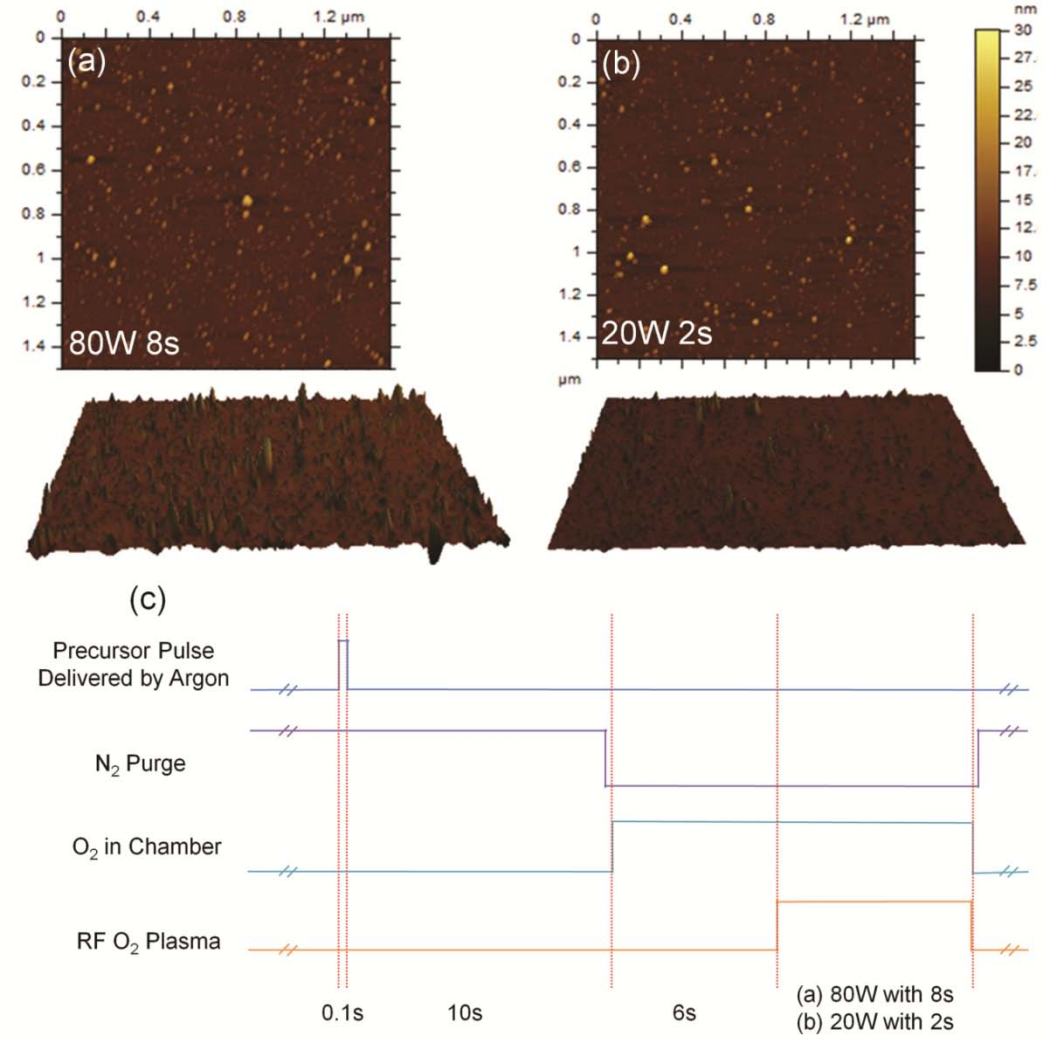

Figure 4.4. AFM topography images of Hf oxide films deposited with O plasma pulse conditions of: (a) 80 W and 8 s exposure, (b) 20 W and 2 s exposure, and (c) the ALD processing sequence.

4.4.2 La oxide films

Figure 4.5 presents AFM and XPS results of La oxide films deposited with different plasma power and oxygen exposure times. Both films have a smooth surface without protruding islands, consistent with the amorphous nature typically obtained for La oxides.[17,18] Although the morphology is improved, the XPS indicates the presence of a significant amount of carbon in the deposited films (see Fig. 4.5). The feature normally associated with adventitious surface carbon at ~284 eV is hardly evident. With higher power or longer oxygen plasma exposure, the carbon concentration can be reduced. The binding energy of the C 1s peak shifts from ~291 eV to ~290 eV depending on the conditions employed for the oxygen plasma step. This range of binding energy is close to the value for carbon bonded in carbonate structure, which indicates the oxidation of the carbon. This detection of carbon oxide could be due to the absorption of CO_2 and formation of $La_2O_2CO_3$ during the growth of La oxide.[19]

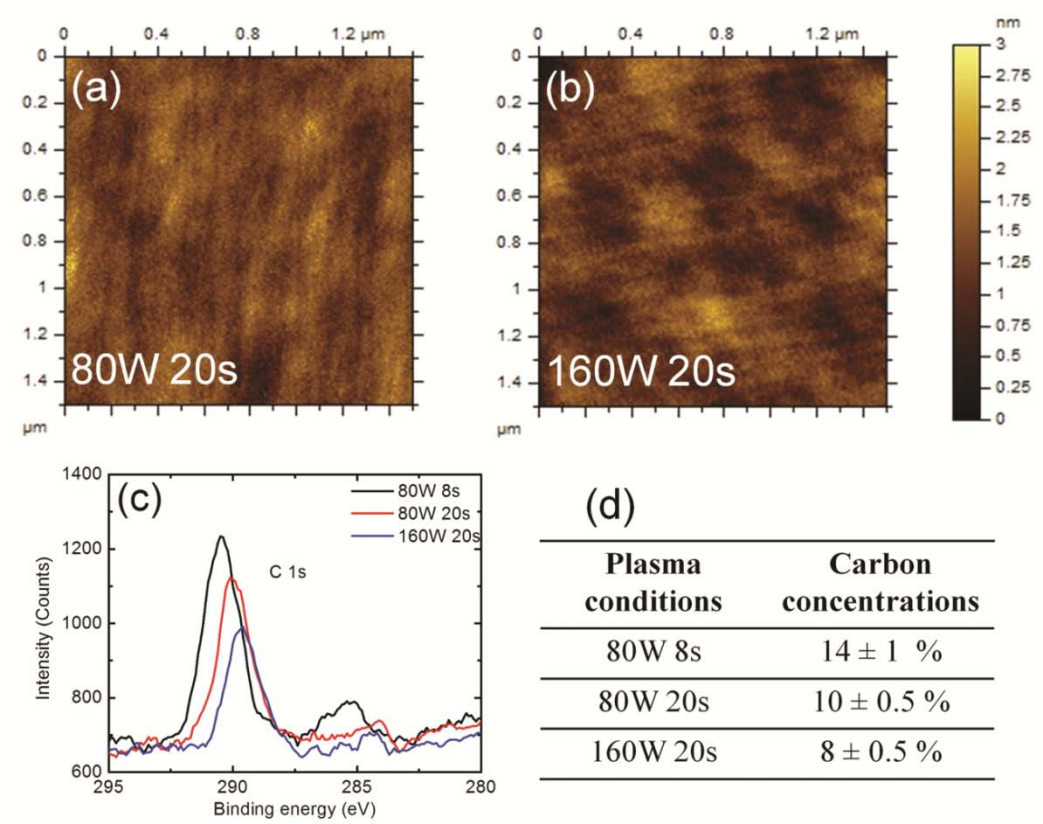

(d)

Plasma conditions	Carbon concentrations
80W 8s	14 ± 1 %
80W 20s	10 ± 0.5 %
160W 20s	8 ± 0.5 %

Figure 4.5. AFM topography images of La oxide films deposited with O plasma pulse conditions of: (a) 80 W and 20 s exposure, and (b) 160 W and 20 s exposure; (c) XPS spectra of the C 1s peak and (d) carbon concentrations of La oxide films deposited with different O plasma pulse conditions.

4.4.3 Hf-La oxide films

In order to suppress crystallization of the Hf oxide film, we deposited alloyed Hf-La oxide films by growing 1-3 cycles of La-oxide between two adjacent Hf-oxide cycles. This approach has also been employed at higher deposition temperatures using thermal ALD.[20-22] The relative percentages of Hf and La in the alloyed films can be controlled by the ratio of the number of Hf and La cycles. As shown in Fig. 4.6, AFM images of the alloyed Hf-La oxide films display a significant reduction in the density of protruding islands compared

with that of pure Hf oxide films. The thickness of the films is ~7 nm. For the film grown with a 1La/1Hf cycle ratio, a number of tall islands are observable protruding from the surface. When the cycle ratio is increased to 2La/1Hf, the density of protruding island is suppressed. In Fig. 4.6(c), an analysis of the element concentration is listed. From the figure, it is evident that carbon in the alloyed films can be controlled to a relatively low value of ~1.6%. This result suggests that the incorporated Hf inhibits the formation of La carbonate ($La_2O_2CO_3$) during the ALD growth.

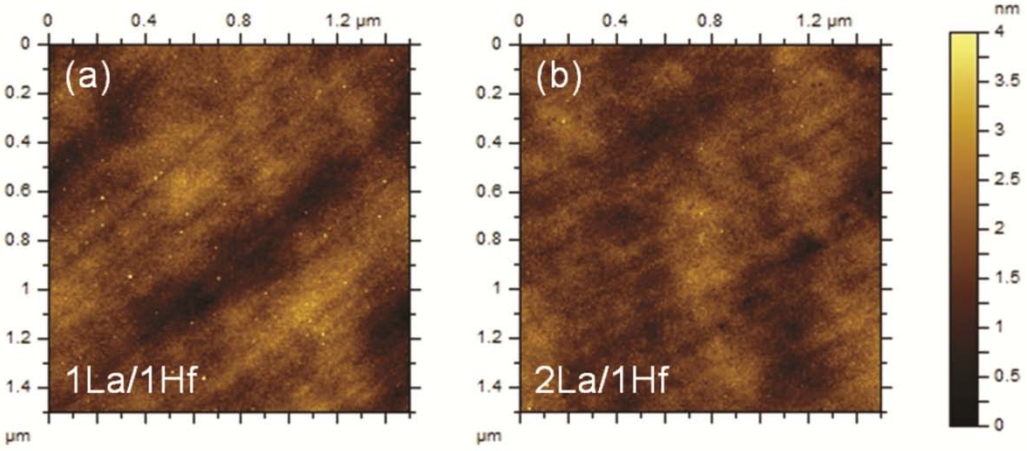

(c)	La (%)	Hf (%)	O (%)	C (%)
255 deg-3La/1Hf	23.6±0.7	13.4±0.2	63±1.2	<1
175 deg-3La/1Hf	23.0±0.5	9.7±0.2	63.9±1.3	3.4±0.8
175 deg-2La/1Hf	15.8±1.1	14.6±0.4	68.0±0.7	1.6±0.2
175 deg-1La/1Hf	14.0±0.6	16.7±0.3	67.7±2.0	1.6±0.3

Figure 4.6. AFM topography images of the oxide film deposited with different cycle ratios: (a) 1La/1Hf and (b) 2La/1Hf; (c) atomic concentrations.

a) Film Crystallinity

Figure 4.7 shows cross-sectional electron micrographs of the pure Hf oxide film and the alloyed Hf-La oxide film. It is evident that micro-crystalline domains extend through the entire thickness of the Hf oxide. The existence of such grain boundaries is often associated with enhanced leakage current. For the alloyed film, electron micrographs did not reveal evidence for distinct crystalline structures, thus indicating an amorphous structure for the alloy. These observations are consistent with the conclusions deduced from the AFM measurements.

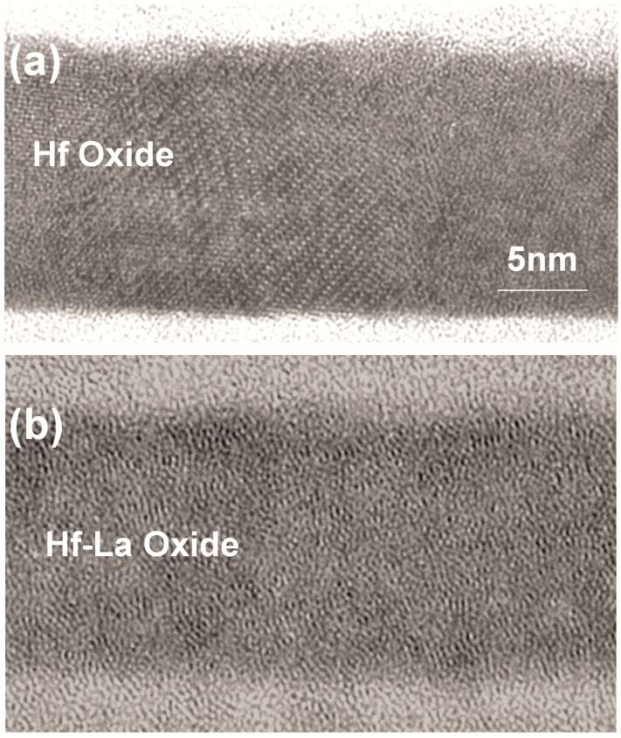

Figure 4.7. Cross sectional TEM images of: (a) pure Hf oxide, and (b) alloyed oxide film with a 2La/1Hf cycle ratio.

b) Electrical properties

A mercury probe was employed to measure the capacitance vs. voltage at

low frequency for the deposited oxide film. Using the low frequency results, we found that the effective dielectric constants of the pure Hf oxide film and alloyed Hf-La oxide films were 18.1±1.2 and 14.2±1.5, respectively. Figures 4.8(a) and 4.8(b) show I-V curves of pure Hf oxide and alloyed Hf-La oxide just before breakdown. We found that the alloyed Hf-La oxide film has a break down strength of 3.0 ± 0.3 MV/cm while the breakdown strength of the pure Hf oxide film is 1.4 ± 0.2 MV/cm. He *et al*[20] also reported a higher breakdown field for alloyed Hf-La oxide than that of pure Hf oxide after the films were annealed to above 500 ºC.

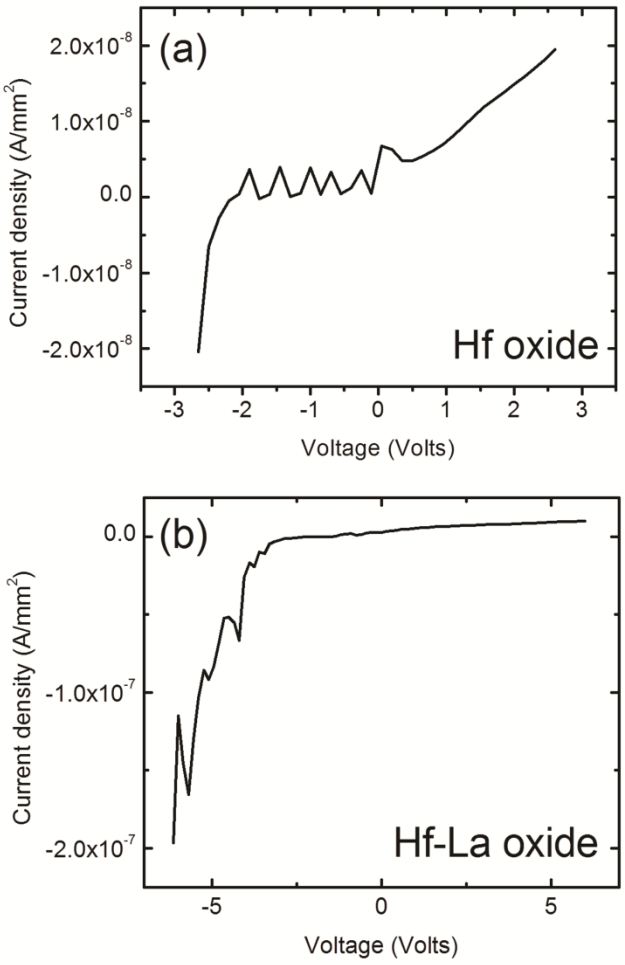

Figure 4.8. I-V curves of: (a) pure Hf oxide, and (b) alloyed oxide film.

4.5 Conclusions

We have found: (1) significant excess oxygen species are present in Hf oxide films deposited at low temperature by RPALD, which can be partially removed by a post He plasma treatment; (2) crystallized grains protrude from the surface of Hf oxide films even when using low rf power to excite the oxygen plasma and a short exposure time; (3) the alloyed Hf-La oxide film displays a smooth surface and low C concentration; (4) the alloyed Hf-La oxide film has a

higher breakdown voltage than that of pure Hf oxide film consistent with an amorphous structure.

REFERENCES

[1] A. I. Kingon, J. P. Maria and S. K. Streiffer, Nature 406, 1032 (2000).

[2] G. D. Wilk, R. M. Wallace and J. M. Anthony, J. Appl. Phys. 89, 5243 (2001).

[3] B. H. Lee, K. H. Lee, S. Im and M. M. Sung, Org. Electron. 9, 1146 (2008).

[4] P. K. Park, J. S. Roh, B. H. Choi and S. W. Kang, Electrochem. Solid State Lett. 9, F34 (2006).

[5] J. S. Park, H. S. Park and S. W. Kang, J. Electrochem. Soc. 149, C28 (2002).

[6] Y. Won, S. Park, J. Koo, S. Kim, J. Kim and H. Jeon, Appl. Phys. Lett. 87, 262901 (2005).

[7] S. Choi, J. Koo, H. Jeon and Y. Kim, J. Korean Phys. Soc. 44, 35 (2004).

[8] M. Leskela and M. Ritala, Thin Solid Films 409, 138 (2002).

[9] T. Suntola, Thin Solid Films 216, 84 (1992).

[10] L. Belau, J. Y. Park, T. Liang and G. A. Somorjai, J. Vac. Sci. Technol. B 26, 2225 (2008).

[11] C. Driemeier, R. M. Wallace and I. J. R. Baumvol, J. Appl. Phys. 102, 024112 (2007).

[12] S. Lee, S. Bang, J. Park, S. Park, W. Jeong and H. Jeon, Phys. Status Solidi A-Appl. Mat. 207, 1845 (2010).

[13] S. Song, W. K. Hong, S. S. Kwon and T. Lee, Appl. Phys. Lett. 92, 263109 (2008).

[14] H. Kind, H. Q. Yan, B. Messer, M. Law and P. D. Yang, Adv. Mater. 14, 158 (2002).

[15] C. C. Fulton, G. Lucovsky, and R. J. Nemanich, J. Appl. Phys. 99, 063708 (2006).

[16] D. M. Hausmann and R. G. Gordon, J. Cryst. Growth 249, 251 (2003).

[17] Jin-Bo Chengb, Ai-Dong Li, Qi-Yue Shao, Hui-Qin Ling, Di Wu,Yuan Wang, Yong-Jun Bao, Mu Wang, Zhi-Guo Liu, Nai-Ben Ming, Applied Surface Science 233 91–98 (2004).

[18] K. Kukli, M. Ritala, V. Pore, M. Leskelä, T. Sajavaara, R. I. Hegde, D. C. Gilmer, P. J. Tobin, A. C. Jones, and H. C. Aspinall, Chem. Vap. Deposition, 12, 158–164 (2006).

[19] M. Nieminen, M. Putkonen and L. Niinisto, Appl. Surf. Sci. 174, 155 (2001).

[20] W. He, D. S. H. Chan, S. J. Kim, Y. S. Kim, S. T. Kim and B. J. Cho, J. Electrochem. Soc. 155, G189 (2008).

[21] T. Wang and J. G. Ekerdt, Chem. Mat. 21, 3096 (2009).

[22] T. Wang and J. G. Ekerdt, Chem. Mat. 22, 3798 (2010).

Chapter 5

BAND ALIGNMENT OF ZINC OXIDE AS A CHANNEL LAYER IN A GATE STACK STRUCTURE GROWN BY PLASMA ENHANCED ATOMIC LAYER DEPOSITION

5.1 Abstract

A gate stack structure with a thin ZnO layer between an oxidized Si(100) surface and an alloyed hafnium and lanthanum oxide (HfO_2-La_2O_3) layer was prepared by plasma enhanced atomic layer deposition (PEALD) at ~ 175 °C. High resolution electron microscopy indicated an amorphous structure of the deposited layers. The electronic properties were characterized with x-ray and ultraviolet photoemission spectroscopy. A significant amount of excess oxygen was observed in the as-deposited ZnO and (HfO_2-La_2O_3) layers. A helium plasma post-deposition treatment can partially remove the excess oxygen in both layers. The band alignment of this structure was established for an *n*-type Si substrate. A valence band offset of 1.5 ± 0.1 eV was measured between a thin ZnO layer and a SiO_2 layer. The valence band offset between HfO_2-La_2O_3 (11% HfO_2 and 89% La_2O_3) and ZnO was almost negligible. The band relationship developed from these results demonstrates confinement of electrons in the ZnO film as a channel layer for thin film transistors.

5.2 Introduction

Many applications are considering flexible displays based on transparent thin film transistors (TFTs). However, conventional TFTs prepared with

hydrogenated amorphous silicon (a-Si:H) as the active channel layer material are limited by a low mobility less than 1.0 cm^2/Vs [1]. Alternatively, transparent semiconductor materials such as zinc oxide have been proposed for the channel layer. ZnO is a semiconductor material with a direct band gap of 3.4 eV at room temperature [2], and a room temperature mobility of 10~100 $cm^2/V{\cdot}s$ [3, 4]. As-grown, undoped, ZnO films typically exhibit *n*-type semiconductor characteristics with an electron concentration from 10^{17} to 10^{21} cm^{-3}. [5, 6] This high carrier concentration has been attributed to defects such as zinc interstitials or oxygen vacancies. [7, 8]

Atomic layer deposition (ALD) has been considered as a promising approach for ZnO film deposition for TFTs. ALD is a self-limiting process, where growth is achieved by alternatively pulsing precursors into the deposition chamber. [9, 10] The advantages of ALD include conformal coating, thickness uniformity, and composition and stoichiometry control. High mobility zinc oxide thin films have been successfully grown by thermal ALD at temperatures ranging from 200 to 350 °C. [11-13]. Recently, low temperature (100~200 °C) thermal ALD growth of ZnO has also reported. [14]

TFT's in flexible transparent displays require a process temperature less than 180 °C, and plasma enhanced atomic layer deposition (PEALD) has been considered to achieve a ZnO deposition temperature in the range of 25~120 °C. Diethyl zinc (DEZn) and dimethyl zinc (DMZn) have been employed as precursors for this process, and PEALD ZnO thin films have exhibited mobilities of 1.0 to 6.0 $cm^2/V{\cdot}s$ [15, 16]. In PEALD, the activated oxygen species generated

by the plasma can significantly reduce the deposition temperature and produce a denser film with potentially lower defect concentration. In order to minimize the effects of the defects and excess species, studies up to now have focused on high temperature deposition or post deposition annealing. [17-19] Neither process is appropriate for flexible substrates. Thus, incorporation of ZnO into a TFT process requires low temperature processes, and in this study we employ PEALD growth and a low temperature treatment process as a possible approach.

For TFT device structures, it is necessary to understand the band alignment of ZnO and appropriate dielectrics. In this study, an ultrathin ZnO film was prepared as an interlayer between an alloyed HfO_2-La_2O_3 layer and an oxidized Si substrate. This alloyed HfO_2-La_2O_3 high-k dielectric has advantageous properties of high dielectric constant ~14 and an amorphous structure with a low leakage current. [20] High resolution electron microscopy has confirmed the amorphous structure of the deposited films. The band relations for HfO_2- La_2O_3, ZnO and the oxidized *n*-type Si substrate were then determined from *in situ* photoemission measurements. The results are also sensitive to internal electric fields and interfacial charge transfer which can occur during growth.

5.3 Experiment

The experiments are accomplished *in-situ* using an integrated ultrahigh vacuum (UHV) system. This system involves a linear ~20 m UHV transfer line chamber with a base pressure of 5×10^{-10} Torr that connects different process and characterization chambers, which enables *in situ* measurement without

introducing contamination. In this study, the following systems are used: remote oxygen plasma for cleaning, remote helium plasma for film treatment, plasma enhanced atomic layer deposition for HfO_2-La_2O_3 and ZnO growth, X-ray photoelectron spectroscopy (XPS) for core level analysis, and ultraviolet photoelectron spectroscopy (UPS) for valence band spectra.

The substrates used in this study are ambient oxidized *n*-type, phosphorous doped, Si (100) wafers with a resistivity of 0.05-0.09 Ω·cm. Prior to loading the substrates into the vacuum chamber, the wafers were ultrasonically cleaned in acetone and methanol for 15 min for each process, and dried in ultrahigh-purity nitrogen gas. After transfer into the UHV system, the Si(100) surfaces were cleaned and oxidized by a remote oxygen plasma process. The plasma exposure conditions were as follows: substrate at room temperature, 60 mTorr oxygen pressure, gas flow of 10 standard cubic centimeters per minute (sccm), and rf power of 30W to excite the plasma. The remote oxygen plasma can effectively remove hydrocarbon contamination and passivate the Si surface with a thin SiO_2 layer [21]. After *in-situ* cleaning, the sample was annealed at 500℃ for 5 minutes for defect reduction and removal of adsorbed oxygen. The surfaces were then characterized by XPS and UPS.

The oxide films were deposited using a custom computer-controlled PEALD system at a growth temperature of ~ 175 °C. The base pressure of the chamber was 1.0×10^{-8} Torr from the turbo-drag pump. After the 0.1 s precursor pulse, nitrogen gas was introduced for 10 s to purge excess precursor. After the nitrogen purge, oxygen was introduced into the chamber 6 s before the plasma

excitation, and the plasma was sustained by rf-power for another 8 s. Subsequently, the chamber was pumped for 2 s and purged by nitrogen gas for 8 s before the next growth cycle. The pressure in the chamber during deposition was controlled by a throttle valve to a value of 100 mTorr. The stainless steel bubbler containing the Zn precursor (dimethyl zinc, DMZn) was cooled to -17.2 ˚C during deposition. For growth of the hafnium and lanthanum oxides, the Hf precursor (tetrakis(ethylmethylamino)hafnium(IV)) and La precursor (tris(isopropylcyclopenta-dienyl)lanthanum) were heated to 48 ˚C and 168 ˚C, respectively. The chamber and gas lines were heated to ~100 ˚C to avoid precursor condensation. The remote oxygen plasma was excited with ~200 W of 13.56 MHz rf-power applied to a helical copper coil wound around a 32 mm diameter quartz tube that opens toward the sample. The post-deposition He plasma treatment was excited with 30 W for 5 min. with a He gas flow rate of 90 sccm, and the chamber pressure was maintained at ~60 mTorr. The remote plasma excitation (without sample bias), results in the sample being exposed to free radicals, excited molecules and a low density of ions. A representative sample was observed in cross-section geometry using a JEOL JEM 4000EX high-resolution electron microscope operated at 400 keV.

The sample was characterized by XPS and UPS after each processing step. XPS characterization was performed at a base pressure of 6×10^{-10} Torr using the 1253.6 eV Mg Kα line of a VG XR3 source and a VG microtech Clam II analyzer operated at a resolution of 0.1 eV. The films for XPS analysis were less than 5 nm thick, and our prior studies have established that charging effects can be neglected

because of tunneling to the conducting Si substrate. [22] Ultraviolet photoemission spectra are obtained at a base pressure of 8×10^{-10} Torr using the He I line at 21.2 eV and a VSW 50 mm mean radius hemispherical analyzer and VSW HAC 300 controller operated at an electron energy resolution of 0.15 eV. A negative 6.00 V bias was applied to the substrate to overcome the work function of the analyzer.

5.4 Results and discussion

The *in-situ* experiments consisted of the following deposition and treatment process: 1) remote oxygen plasma cleaning of the Si substrate, 2) PEALD growth of a ~1.5 nm zinc oxide film, 3) 5 min. He plasma treatment, 4) PEALD growth of a ~2 nm of HfO_2-La_2O_3 film, 5) 5 min. He plasma treatment. *In-situ* XPS and UPS measurements were employed after each processing step, and the spectra are shown in Figs. 5.1- 5.4. The XPS observation "windows" were set for the Si 2p, O 1s, Zn 2p, La 3d, Hf 4f and C 1s core levels.

5.4.1 Oxidized Si substrate

The Si substrate was processed with an oxygen plasma and then annealed in vacuum at 500 °C for 5 minutes. A prior study has established that the SiO_2 layer is ~1.0nm thick. [23] The sample was then transferred in UHV to chambers for the XPS and UPS measurements. The XPS scans of the Si 2p core level are shown in Fig. 5.1. The XPS binding energies of the Si 2p (Si and SiO_2), along with those of Zn 2p 3/2, La 3d 5/2 and Hf 4f 7/2 are summarized in Table 5.1. The initial Si 2p peaks are at 99.7 and 103.6 eV, respectively, corresponding to bulk Si near the surface and the SiO_2 layer of the oxidized Si. Prior studies have

established that the Si 2p core level is 98.8 eV below the valence band maximum (VBM) [23]. For the doped *n*-type Si wafer, the Fermi level is at 0.9-1.0 eV above the VBM. Therefore, the initial *n*-type Si substrate displays a flat band condition as the Si 2p peak is at 99.7 eV (98.8 + 0.9 eV). After ZnO deposition, the Si bulk and SiO_2 related peaks shifted to lower binding energies of 99.5 and 103.0 eV, respectively. However, after the He plasma treatment, the Si peaks shifted back to 99.7 and 103.5 eV, respectively. After the 2 nm HfO_2-La_2O_3 deposition, the Si peak corresponding to bulk Si shifted to a lower binding energy of 99.6 eV, and after the He plasma treatment, it shifted back to 99.7 eV. The shifts in the Si bulk feature are attributed to a change of the band bending in the Si substrate, and the differential shifts between the Si substrate and the Si oxide features are attributed to an electric potential across the SiO_2 layer.

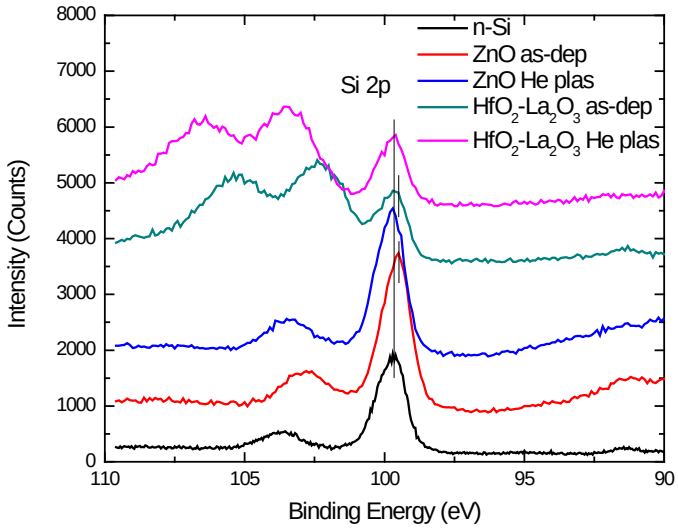

Figure 5.1 X-ray photoemission spectra of the Si 2p peaks for the oxidized *n*-type Si(100) substrate. The curves are for the oxidized Si (100) substrate, as-deposited

ZnO on the Si substrate, He plasma treated ZnO film, as-deposited HfO_2-La_2O_3 on ZnO, and He plasma treated HfO_2-La_2O_3 film.

5.4.2 1.5 nm ZnO

After characterization of the Si substrate, a ~1.5 nm thick ZnO film was deposited using 6 PEALD growth cycles with a rate of 0.25 nm/cycle. The XPS and UPS measurements followed the growth. The film was then treated using a He plasma, which was again followed with XPS and UPS scans. The XPS spectra of the Zn 2p 3/2 core level are shown in Fig. 5.2. The initial as-deposited Zn 2p 3/2 peak was located at 1021.2 eV, but after the He plasma treatment the peak shifted to a higher binding energy of 1022.2 eV. Similarly, after capping by the HfO_2-La_2O_3 layer, the Zn 2p 3/2 peak shifted back to 1021.0 eV. After the He plasma treatment, the peak shifted to a higher binding energy of 1021.9 eV.

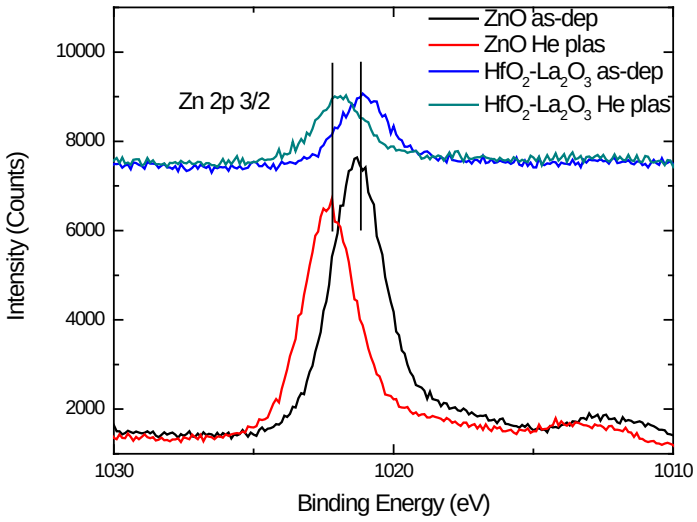

Figure 5.2 X-ray photoemission spectra of the Zn 2p 3/2 peaks for the oxidized *n*-type Si(100) substrate. The scans are for the oxidized Si (100) substrate, as-

deposited ZnO, He plasma treated ZnO film, as-deposited HfO_2-La_2O_3, and He plasma treated HfO_2-La_2O_3 film.

In our previous work, a mechanism of photon-induced desorption of the excess oxygen species was proposed to explain this phenomenon. [20] During a remote oxygen plasma ALD deposition, excess oxygen may be incorporated in the film which can then accept negative charges. The negative charges in the ZnO will induce positive charges in the depletion region of the Si substrate. We suggest that the charges in the ZnO will reside near the ZnO/SiO_2 interface due to the presence of the electric field. This charge distribution produces an electric field largely across the SiO_2 layer. In the band diagram, it results in upward band bending in the Si and band tilting in the SiO_2 layer, shown schematically in Fig. 5.3 (a). The UV photons generated in the He plasma can penetrate through the film, and induce desorption of the excess oxygen. The process leads to recovery of the flat band condition as shown in Fig. 5.3 (b), consistent with the binding energy shift to higher values observed from the XPS measurements.

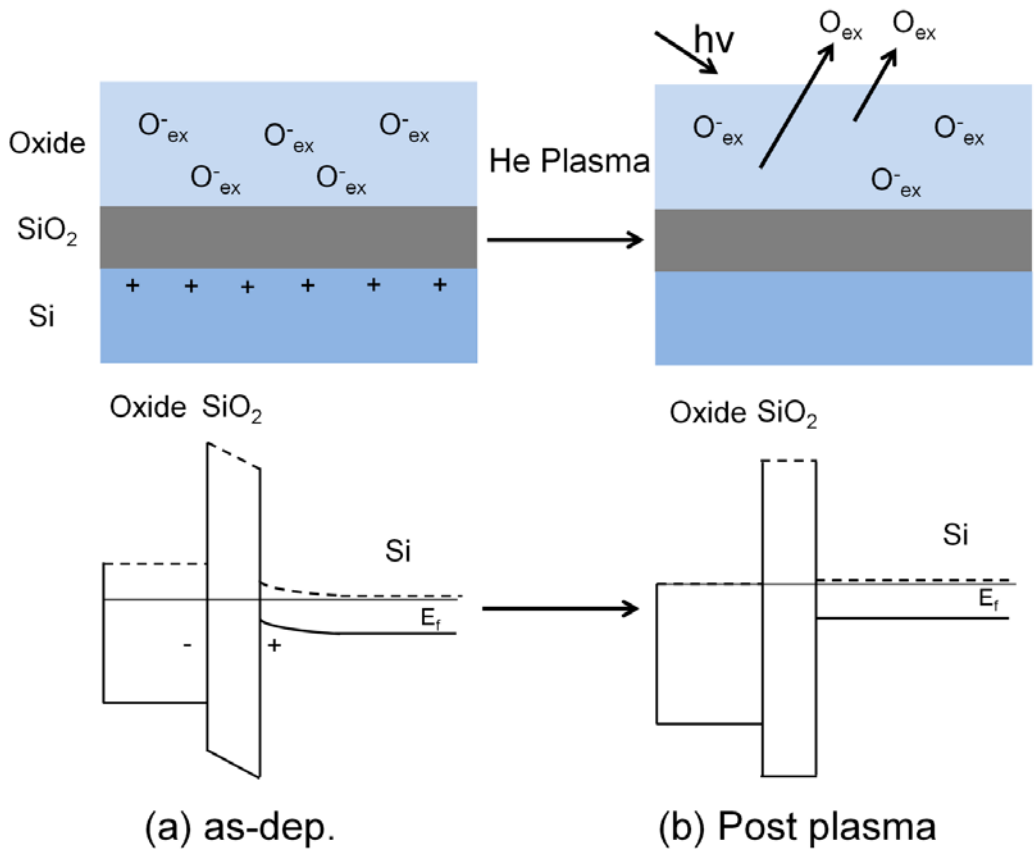

Figure 5.3 Schematic of the proposed mechanism for oxygen desorption induced by the He plasma process: (a) excess oxygen is incorporated in the as-deposited oxide film and (b) oxygen is desorbed from the film during ultraviolet light (UV) illumination generated from the He plasma. The band alignment diagram shows the band shifts before and after He plasma treatment.

5.4.3 2 nm HfO_2-La_2O_3

The PEALD system was employed to deposit a ~2 nm HfO_2-La_2O_3 alloyed film on the ZnO layer using six cycles of 1 HfO_2 step followed by 3 La_2O_3 steps. The relative concentration of HfO_2 and La_2O_3 in the alloyed films can be controlled by the ratio of the number of HfO_2 and La_2O_3 cycles. For this alloyed film, the relative concentration determined by XPS was 11% HfO_2 and

89% La_2O_3. The HfO_2-La_2O_3 alloyed films exhibit an amorphous structure without crystalline grains which is contrasted to the nanocrystalline structure typically observed for pure HfO_2. [20] After the HfO_2-La_2O_3 deposition, the sample was again treated by the helium plasma process to remove excess oxygen.

Each step of the process was characterized with XPS and UPS. The XPS spectra of the La 3d, Hf 4f and C 1s core levels are shown in Fig. 4. For the as-deposited film, the La 3d 5/2 peak was located at 833.9 eV, and after He plasma treatment, the peak shifted to 835.1 eV (shown in Fig. 5.4(a)). The peaks at ~ 837 eV and 856 eV are the La 3d satellite peaks which are observed in dielectric films. [24] Similarly, the Hf 4f 7/2 peak was at 16.4 eV for the as-deposited film, and after He plasma treatment, the peak shifted to 17.4 eV. The peak shifts are attributed to charge transfer during processing, as shown in Fig. 5.3. After the initial PEALD deposition, the excess oxygen acquires a negative charge which produces an electric field across the oxide and upward band bending in the Si. After the He plasma treatment, the plasma-generated UV light enhances desorption of the excess oxygen, leading to a flat band condition. The observed peak shifts are also consistent with the Zn 2p peak shifts.

Fig. 5.4(c) shows the C 1s peaks during the process. The feature normally associated with adventitious surface carbon at 284 eV is hardly evident. However, a feature at ~ 294 eV became evident after deposition of the HfO_2-La_2O_3 layer. This peak is interpreted as partially oxidized carbon, which has been attributed to the formation of $La_2O_2CO_3$ during the growth of La oxide. [25] This oxidized carbon peak also shifted to higher binding energy after the He plasma treatment.

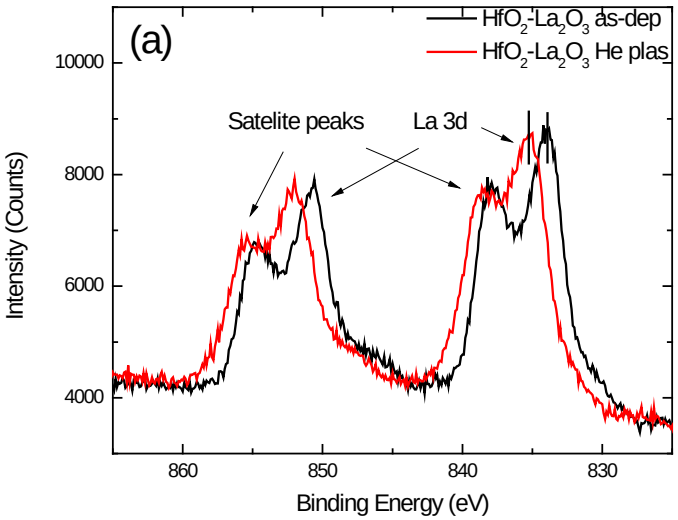
(a)
HfO2-La2O3 as-dep
HfO2-La2O3 He plas
Satelite peaks
La 3d
Intensity (Counts)
Binding Energy (eV)
10000
8000
6000
4000
860
850
840
830

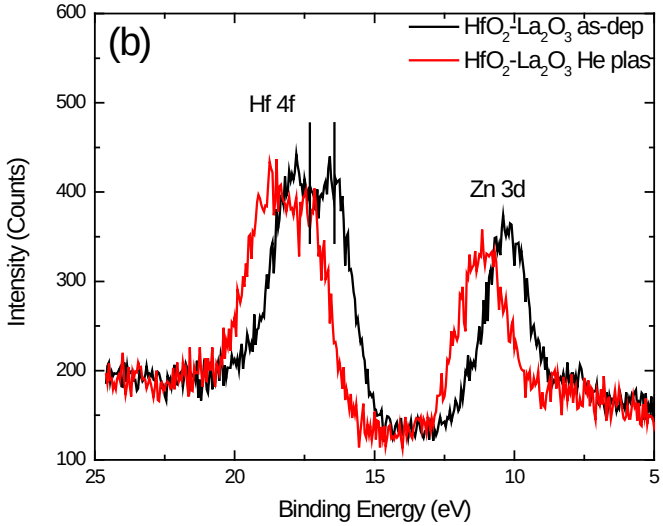
(b)
HfO2-La2O3 as-dep
HfO2-La2O3 He plas
Hf 4f
Zn 3d
Intensity (Counts)
Binding Energy (eV)
600
500
400
300
200
100
25
20
15
10
5

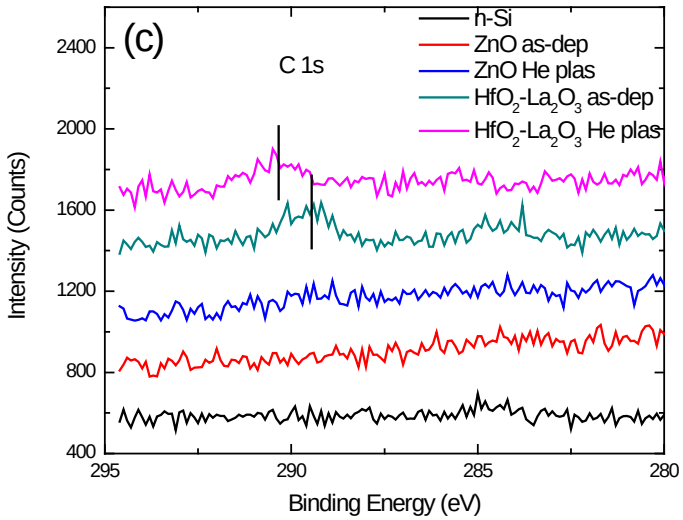

Figure 5.4 X-ray photoemission spectra of (a) La 3d peaks, (b) Hf 4f peaks, and (c) C 1s peaks. The curves are for the oxidized Si (100) substrate, as-deposited ZnO, He plasma treated ZnO film, as-deposited HfO_2-La_2O_3, and He plasma treated HfO_2-La_2O_3 film.

5.4.4 Ultraviolet photoemission spectra

The ultraviolet photoemission spectra for the cleaned, oxidized substrate, after ZnO deposition, and after the HfO_2-La_2O_3 deposition are shown in Fig. 5.5. The UPS spectrum of the initial clean SiO_2 layer on an *n*-type Si substrate typically shows the valence band maximum (VBM) at 5.5 eV below the Fermi level. The valence band offset between Si and SiO_2 is then 4.5 eV for the *n*-type Si substrate, which agrees with previous results [26]. These results are consistent with a low interface state density and negligible band bending for the *n*-type substrate. For the ZnO film, the front cutoff of the UPS spectra indicates the valence band maximum which is at 4.0 eV and 3.0 eV below the Fermi level

before and after the He plasma treatment, respectively. After the 2.0 nm HfO_2-La_2O_3 layer deposition, the front cutoff of the UPS spectra is at 2.8 eV and 4.0 eV below the Fermi level before and after He plasma treatment, respectively. The VBM shift is again attributed to the He plasma treatment effect.

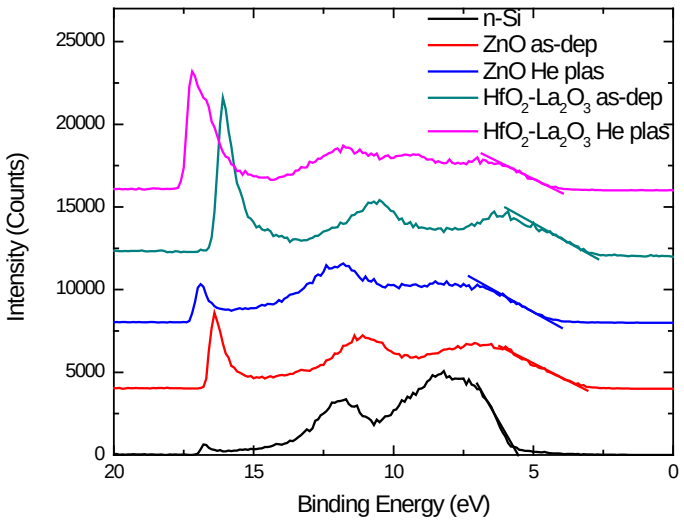

Figure 5.5 Ultraviolet photoemission spectra of the oxidized Si (100) substrate, as-deposited ZnO, He plasma treated ZnO film, as-deposited HfO_2-La_2O_3, and He plasma treated HfO_2-La_2O_3 film. The straight lines indicate the position of the VBM.

5.4.5 Transmission electron microscopy

Figure 5.6 displays a cross-sectional high resolution electron micrograph of the sample structure. The total thickness of the oxide layers is ~4.5 nm. The HfO_2-La_2O_3 layer is evident as the the upper ~2.0 nm layer. The contrast of the HfO_2-La_2O_3 layer is uniform, and the HfO_2-La_2O_3/ZnO interface is sharp as is the SiO_2/Si interface. However, the interface of ZnO/SiO_2 is not evident due to the

low contrast difference between ZnO and SiO_2. There is no evidence of crystalline order or domains in any of the oxide layers. The results indicate an amorphous structure with sharp interfaces without evidence of intermixing.

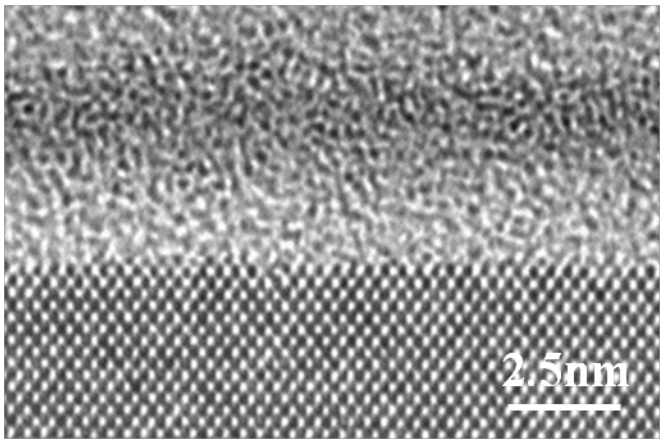

Figure 5.6 Cross sectional high-resolution electron micrograph of the HfO_2-La_2O_3/ZnO/SiO_2 structure on *n*-type Si.

5.4.6. Band alignment schematics

Figure 5.7 shows diagrams of the band alignment for the stacked structure during processing. The initial cleaned oxidized Si substrate displays a flat band condition, shown in Fig. 5.7(a). After ZnO deposition, the SiO_2 band is tilted upwards, shown in Fig. 5.7(b). The valence band offset between ZnO and SiO_2 can be determined using the following expression:

$$VBO= (E_{2p3/2}^{ZnO} - E_{VBM}^{ZnO}) - (E_{2p}^{SiO2} - E_{VBM}^{SiO2}) - \Delta1(E_{2p3/2}^{ZnO} - E_{2p}^{SiO2}) - \Delta2(SiO_2)$$

where $(E_{2p3/2}^{ZnO} - E_{VBM}^{ZnO})$ is the Zn 2p3/2 core level to the VBM of ZnO, $(E_{2p}^{SiO2} - E_{VBM}^{SiO2})$ is the Si 2p core level to the VBM of SiO_2, $\Delta1(E_{2p3/2}^{ZnO} - E_{2p}^{SiO2})$ is the energy separation between the Zn 2p3/2 of ZnO and Si 2p of SiO_2,

and $\Delta 2(SiO_2)$ is the half value of the electrical potential across the SiO_2 layer. The electrical potential across the SiO_2 layer can be calculated as 0.8 eV, based on the Si 2p peak shift of ~ 0.6 eV and the substrate Si 2p peak shift of ~ 0.2eV. From Table 5.1, the VBO of ZnO and SiO_2 is calculated as 1.5 eV. After He plasma treatment, the bands return to a flat band condition as the Si 2p peaks return to their initial position for the cleaned Si substrate, shown in Fig. 5.7(c). The VBO of ZnO and SiO_2 is the difference between the VBM of ZnO and SiO_2 which, as measured by UPS, is ~ 1.5 (5.5 - 4.0) eV. This value is consistent with the 1.5 eV value, deduced from the XPS measurements.

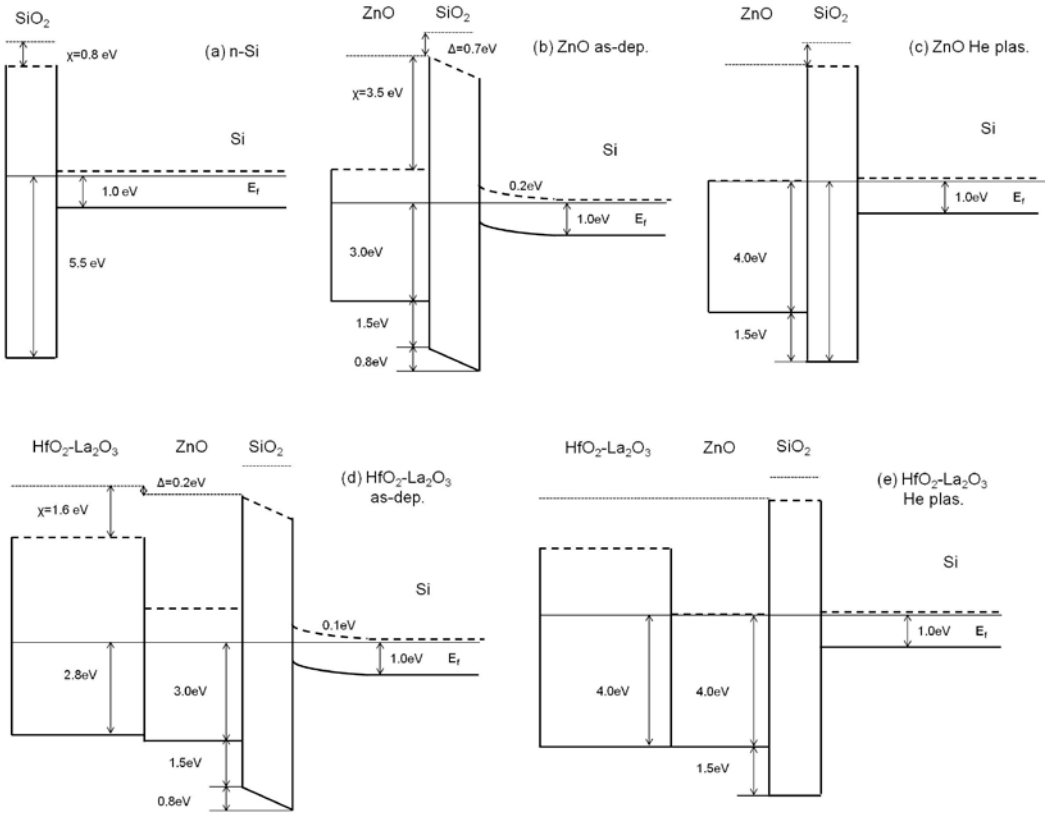

Figure 5.7 Band alignment diagram of (a) the oxidized Si (100) substrate, (b) as-deposited ZnO on the oxidized Si substrate, (c) He plasma treated ZnO film, (d)

as-deposited HfO_2-La_2O_3 on ZnO, and (e) He plasma treated HfO_2-La_2O_3 film. Dashed lines are used to represent the conduction band minimum of the oxides which are deduced from reported values of the band gap. Horizontal distances approximately represent the experimental film thickness except for the depletion region in the Si which is compressed as indicated.

Table 5.1: XPS of Si 2p (Si and SiO_2), Zn 2p, La 3d, Hf 4f core levels, and valence band maximum (VBM) relative to the Fermi level, in eV.

	Si 2p (Si)	Si2p (SiO2)	Zn 2p 3/2	La 3d 5/2	Hf 4f 7/2	VBM
n-Si	99.7	103.6	/	/	/	5.5
ZnO as-dep.	99.5	103.0	1021.2	/	/	3.0
ZnO He plas.	99.7	103.5	1022.2	/	/	4.0
HfO_2-La_2O_3 as-dep.	99.6	/	1021.0	833.9	16.4	2.8
HfO_2-La_2O_3 He plas.	99.7	/	1021.9	835.1	17.4	4.0

After HfO_2-La_2O_3 layer deposition, the Si 2p and Zn 2p 3/2 peaks shift to lower binding energy, indicating an electric potential across the SiO_2 layer and band bending in the Si substrate, shown in Fig. 5.7(d). After the He plasma treatment, the Si 2p peak shifts back to a flat band condition. The Zn 2p 3/2, La 3d 5/2 and Hf 4f 7/2 also shift ~ 1 eV to higher binding energy, which is also consistent with the return to flat bands in the Si. The results indicate that there is

almost no offset between the valence bands of the HfO_2-La_2O_3 and ZnO films. In addition, the vacuum levels of the HfO_2-La_2O_3 and ZnO are almost aligned. The reported values of the band gaps are 8.9 eV for SiO_2 and 3.4 eV for ZnO [2]. However, we suggest that the actual band gap of this ultrathin amorphous ZnO film may be larger. A report of ZnO film grown by MOCVD at 200 °C using DMZn as the precursor shows a band gap of 4.0 eV, which was attributed to disorder and nanocrystallinity. [27] Moreover, ZnO film grown by PEALD at l00 °C shows no preferred growth orientation. [28] We also assume 6.0 eV for the band gap of the HfO_2-La_2O_3 alloyed film since the band gap of both HfO_2 and La_2O_3 are ~6.0 eV. [29] It is noted that the CBM of the oxides has been deduced based on the reported band gaps of the materials: 8.9 eV for SiO_2, 4.0 eV for ZnO and 6.0 eV for the HfO_2-La_2O_3 alloyed film. Since these are deduced values, the CBM levels are shown as dashed lines in the figures.

The electron affinity (EA) model can predict the band offset of two materials, which presumes two materials align vacuum levels at the interface. A deviation from the EA prediction can be described as an interfacial dipole. Consequently, the interfacial dipole is often described as the difference between the vacuum levels at the interface of the two adjoining materials. Experimentally this can be determined from the photoemission results using:

$$\Delta Dipole = (h\nu - W^{SiO2}) - (h\nu - W^{ZnO}) - VBO^{SiO2/ZnO} = W^{ZnO} - W^{SiO2} - VBO^{SiO2/ZnO}$$

where hν=21.2 eV is the He I photon energy, W represents the width of UPS spectra (W for SiO_2 is 11.5 eV, ZnO is 13.7 eV, and HfO_2-La_2O_3 is 13.7 eV, respectively). Here (hν –W) is the energy of the vacuum level relative to the VBM, and $VBO^{SiO2/ZnO}$ is the SiO_2/ZnO valence band offset. Using this expression, the experimental results indicate a value of 0.7 eV for the ZnO/SiO_2 interfacial dipole. Similarly, the HfO_2-La_2O_3/ZnO interfacial dipole is essentially zero, since the HfO_2-La_2O_3 and ZnO films show the same UPS spectral width and a negligible band offset. This result is displayed in Fig. 5.8, where the vacuum levels of the HfO_2-La_2O_3 and ZnO films are aligned, with a negligible interface dipole, which indicates that the electron affinity model can describe the HfO_2-La_2O_3/ZnO band offset. For the ZnO/SiO_2 interface, a 0.7 eV interfacial dipole is determined, which indicates the electron affinity model is limited for that interface.

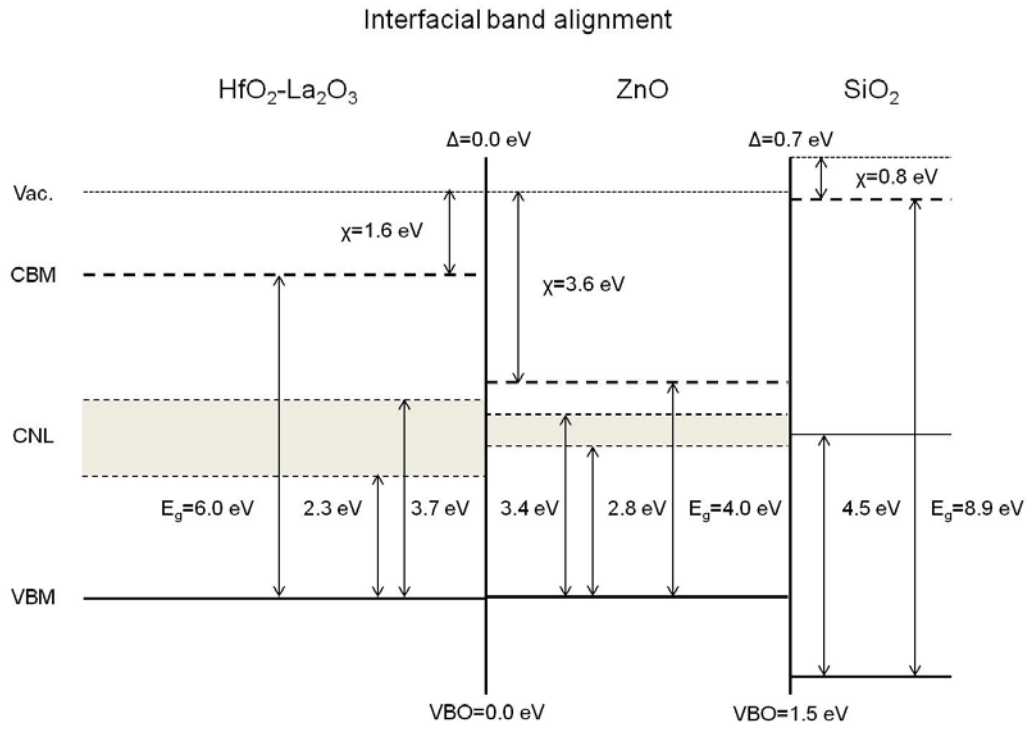

Figure 5.8 Interfacial band alignment diagram of the HfO_2-La_2O_3/ZnO/SiO_2 stack structure at a flat band condition. The VBM and Vac. Level are determined from the experiments, the CBM are from the band gap, and the CNL are from theoretical reports [29-32].

For most heterostructures, interface bonding leads to charge transfer and an interface dipole. For dielectric interfaces a model has been developed by Robertson and Mönch which presumes that the charge will transfer to align the charge neutrality levels (CNL) at the interface. [29,30] The CNLs of HfO_2, La_2O_3 and SiO_2 are calculated as 3.7 eV, 2.3 eV, [29] and 4.5 eV [31] respectively. The CNL of zincblende and wurtzite ZnO has been calculated as 3.6 eV [32] and 3.4 [31], respectively. Alternatively, Mönch employed an empirical model and determined the CNL of ZnO as 2.8 eV [30]. The CNLs of the materials are

displayed in Fig. 5.8. For ZnO a band from 2.8 to 3.4 eV is employed and for HfO_2-La_2O_3 a band from 2.3 to 3.7 eV is indicated. It is evident that the CNL model is capable of describing this structure. However, experimental uncertainties due to the nanocrystalline and alloyed structure of the films and the different theoretical values limit a more detailed analysis at this time.

5.5 Conclusions

A gate stack structure has been deposited at low temperature by PEALD consisting of an HfO_2-La_2O_3 alloyed oxide layer (11% HfO_2 and 89% La_2O_3) and an ultra thin ZnO layer on an oxidized Si substrate. After PEALD growth, excess oxygen is present in the HfO_2-La_2O_3 alloyed film and the ZnO film, and can be partially removed by a helium plasma treatment for each film. TEM micrographs indicated an amorphous structure of the deposited films. The band alignment for this gate stack structure was deduced from *in situ* XPS and UPS spectra. A valence band offset of 1.5 ± 0.1 eV was measured between the ultrathin ZnO layer and the SiO_2 layer. After He plasma treatment, the structure exhibits low interface charge density and flat band conditions. After deposition of the HfO_2-La_2O_3 alloyed oxide capping layer, the valence band offset between the HfO_2-La_2O_3 and ZnO is almost negligible. The band alignment diagrams also show charge transfer during each step of the film growth and processing. The band diagram for this gate stack structure indicates that conduction band electrons can be confined in a ZnO channel layer, demonstrating the potential for application in TFT transistors for display devices.

REFERENCES

[1] K. Nomura, H. Ohta, A. Takagi, T. Kamiya, M. Hirano, and H. Hosono, Nature, Vol 432, 488 (2004).

[2] Mang A, Reimann K and Rubenacke St, Solid State Commun. 94, 251 (1995).

[3] P. F. Carcia, R. S. McLean, and M. H. Reilly, Appl. Phys. Lett. 88, 123509 (2006).

[4] E. Guziewicz, M. Godlewski, T. Krajewski, Ł. Wachnicki, A. Szczepanik, K. Kopalko, A. Wójcik-Głodowska, E. Przeździecka, W. Paszkowicz, E. Łusakowska, P. Kruszewski, N. Huby, G. Tallarida, and S. Ferrari, J. Appl. Phys. 105, 122413 (2009).

[5] S. Keun Kim, C. H. Hwang, S. H. Ko Park, and S. J. Yun, Thin Solid Films 478, 103 (2005).

[6] S. H. Ko Park, C. S. Hwang, H. S. Kwack, J. H. Lee, and H. Y. Chu, Electrochem. Solid-State Lett. 9, G299 (2006).

[7] K.G. Saw, K. Ibrahim, Y.T. Lim, M.K. Chai, Thin Solid Films 515, 2879 (2007).

[8] G. Neumann, Curr. Top. Mater. Sci. 7, 143 (1981).

[9] M. Leskela and M. Ritala, Thin Solid Films 409, 138 (2002).

[10] T. Suntola, Thin Solid Films 216, 84 (1992).

[11] A. Wójcik, M. Godlewski, E. Guziewicz, R. Minikayev, and W. Paszkowicz, J. Cryst. Growth 310, 284 (2008).

[12] Vesa Lujala, Jarmo Skarp, Markku Tammenmaa, Tuomo Suntola, Appl. Surf. Sci. 82/38, 34 (1994).

[13] S.J. Lim, Soonju Kwon, H. Kim, Thin Solid Films, 516, 1523 (2008).

[14] E. Guziewicz, I. A. Kowalik, M. Godlewski, K. Kopalko, V. Osinniy, A. Wójcik, S. Yatsunenko, E. Łusakowska, W. Paszkowicz, and M. Guziewicz, J. Appl. Phys. 103, 033515 (2008).

[15] Y. Kawamura, N. Hattori, N. Miyatake, M. Horita, and Y. Uraoka, Jpn. J. Appl. Phys. 50, 04DF05 (2011).

[16] P.C. Rowlette, C.G. Allen, O.B. Bromley, Amy E. Dubetz, and C. A. Wolden, Chem. Vap. Deposition, 15, 15–20 (2009).

[17] P. K. Park, J. S. Roh, B. H. Choi, and S. W. Kang, Electrochem. Solid-State Lett. 9, F34 (2006).

[18] J. S. Park, H. S. Park, and S. W. Kang, J. Electrochem. Soc. 149, C28 (2002).

[19] Y. Won, S. Park, J. Koo, S. Kim, J. Kim, and H. Jeon, Appl. Phys. Lett. 87, 262901 (2005).

[20] F. Tang, C-Y. Zhu, D. J. Smith, and R.J. Nemanich, J. Vac. Sci. Technol. A30, 01A147 (2012).

[21] T. Yasuda, Y. Ma, S. Habermehl, and G. Lucovsky, J. Vac. Sci. Technol. B 10, 1844 (1992).

[22] C-Y. Zhu, M. Kaur, F. Tang, X. Liu, D.J. Smith and R.J. Nemanich, submitted to J. Appl. Phys.

[23] C.C. Fulton, G. Lucovsky, and R.J. Nemanich, J. Vac. Sci. Technol. B20, 1726 (2002).

[24] A. J. Signorel and R. G. Hayes, Phys. Rev. B8, 81 (1973).

[25] M. Nieminen, M. Putkonen, and L. Niinisto, Appl. Surf. Sci. 174, 155 (2001).

[26] J.W. Keister, J.E. Rowe, J.J. Kolodziej, H. Niimi, T.E. Madey, and G.Lucovsky, J. Vac. Sci. Technol. A 17, 1250 (1999).

[27] S. T. Tan, B. J. Chen, X. W. Sun, W. J. Fan, H. S. Kwok, X. H. Zhang and S. J. Chua, J. Appl. Phys. 98, 013505 (2005).

[28] Yumi Kawamura, Mai Tani, Nozomu Hattori, Naomasa Miyatake, Masahiro Horita, Yasuaki Ishikawa, and Yukiharu Uraoka, Jpn. J. Appl. Phys. 51, 02BF04 (2012).

[29] J. Robertson, J. Vac. Sci. Technol. B 18, 1785 (2000).

[30] W. Mönch, J. Appl. Phys. 109, 113724 (2011).

[31] J. Robertson and B. Falabretti, J. Appl. Phys. 100, 014111, (2006).

[32] W. Mönch, Appl. Phys. Lett. 86, 162101 (2005).

Chapter 6

BAND ALIGNMENT OF VANADIUM OXIDE BETWEEN TWO HAFNIUM OXIDE LAYERS AS A CONFINED WELL STRUCTURE ON SILICON

6.1 Abstract

Vanadium oxide (VO_2) is a narrow vanadium dioxide (VO_2) is a small band gap material that undergoes a metal-insulator phase transition (MIT) at ~343 K due to increasing temperature and evidence of an electric field induced transition at T< 343 K. In this study we prepare a sandwich type gate structure consisting of two ~1.5 nm hafnium oxide (HfO_2) layers with a ~2.0 nm VO_2 interlayer all grown on oxidized n-type silicon substrate. Electrinic properties of the sample were characterized by x-ray, as well as ultraviolet photoelectron spectroscopy after each layer of the structure was grown. The band alignment of each step of growth was analyzed. The valence band offset for the SiO_2/HfO_2 interface is measured as 0.7 eV, and the valence band offset of the HfO_2/VO_2 interface is measured as 3.4 eV.

6.2 Introduction

Vanadium dioxide (VO_2) is a narrow band gap material (Eg = 0.7eV) [1], with a well known Metal to Insulator Transition (MIT) property. This MIT transition can be affect by the temperature change, [1,2] strain[3] and electric field. [4-8]The insulator to metal transition temperature for VO_2 is ~70°C (343K), [1,2] with an abrupt three order magnitude change of resistivity. This transition

temperature can be affected by the strain on the VO_2 and substrate. Some studies of VO_2 on TiO_2 show that the transition temperature can be as low as 300K due to the strains. [3] Recently, people also found that the MIT transition can be achieved by applying an external electric field without temperature changes. [4-8] This critical electric field for MIT transition is ~10^7 V/m. The large resistivity change and abrupt MIT of VO_2, makes it a strong candidate for a variety of optical and electrical switching applications. [9,10]

To develop efficient charge storage or switching devices based on the electronic properties of VO_2, we need to understand the band alignment of VO_2 relative to dielectric interfaces and the Si substrate. In this study, we have prepared a thin VO_2 layer as an interlayer inserted between two layers of the high-k dielectric material (HfO_2), and oxidized *n*-type Si substrates. The measurements on *n*-type substrates explore charge transfer between the layers. Hafnium oxide (HfO_2) is one of the most used high-k gate dielectric materials with a dielectric constant of 20-25 and band gap of 5.6 eV[11]. In this structure the VO_2 layer is able to accept charge through tunneling from the substrate. With the high-k layers an applied gate voltage would control the potential of the VO_2 layer relative to the substrate. The band relations for HfO_2, VO_2, and the oxidized *n*-type Si substrate are determined from *in-situ* photoemission measurements, and the interfacial charge transfer during the growth is discussed.

6.3 Experiment

The experiments were accomplished *in-situ* using an integrated ultrahigh vacuum (UHV) system. This system involves a linear ~20 m long UHV transfer

line chamber with a base pressure of 5×10^{-10} Torr that connects different process and characterization chambers. In this study, the following systems are used: remote oxygen plasma for cleaning, reactive electron beam deposition system for HfO_2 and VO_2 growth, X-ray photoelectron spectroscopy (XPS) for core level analysis, and ultraviolet photoelectron spectroscopy (UPS) for valence band spectra. The sample is transferred between each chamber by a sample cart in the UHV transfer line without exposing to air.

The samples are grown on 25mm dia. *n-type*, phosphorous doped, (100) silicon wafers with a resistivity of 0.05-0.09 Ω·cm. Before loading into the UHV chamber, wafers are cleaned in an ultrasonic acetone bath for 15 min, an ultrasonic methanol bath for another 15 min., and dried in ultra high purity nitrogen gas. After transfer into the UHV system, the Si(100) surfaces are cleaned and oxidized by a remote oxygen plasma. The plasma exposure conditions are as follows: substrate at room temperature, 60 mTorr oxygen pressure, gas flow of 10 standard cubic centimeters per minute (sccm), and rf power of 30W to excite the plasma. The remote oxygen plasma can effectively remove hydrocarbon contamination and passivate the Si surface with a thin SiO_2 layer [12]. After *in-situ* cleaning, the sample was annealed at 500°C for 5 min. for defect reduction and removal of adsorbed oxygen. The surfaces were then characterized by XPS and UPS.

The VO_2 and HfO_2 films were deposited in the reactive electron beam deposition system which has a base pressure of 7×10^{-9} Torr. A 1.5 nm HfO_2 film was directly deposited onto the cleaned Si wafer at room temperature with an

oxygen pressure of 2×10^{-6} Torr. A 2 nm thick VO_2 film was deposited onto the 1.5 nm HfO_2 layer at 550 ºC with an oxygen gas pressure of 6×10^{-4} Torr. Another 1.5 nm HfO_2 film was directly deposited over the VO_2 layer at room temperature with an oxygen pressure of 2×10^{-6} Torr. For each layer a growth rate of 0.01 nm/s was maintained with a quartz crystal thickness rate meter.

The sample was characterized by XPS and UPS at each step. XPS characterization is performed at a base pressure of 6×10^{-10} Torr using the 1253.6 eV Mg Kα line of a VG XR3E2 dual anode source and a VG microtech Clam II analyzer operated at a resolution of 0.1 eV. The resolution of the analyzer was determined from the full width at half maximum (FWHM) of a gold 4f 7/2 spectral peak to be approximately 1.0 eV; however, through curve fitting, the centroid of spectral peaks can be resolved to ± 0.1 eV. Ultraviolet photoemission spectra are obtained at a base pressure of 8×10^{-10} Torr using the He I line at 21.2 eV and a VSW 50 mm mean radius hemispherical analyzer and VSW HAC 300 controller operated at an electron energy resolution of 0.15 eV. A negative 4.00 V bias was applied to the substrate to overcome the work function of the analyzer.

6.4 Results

The *in-situ* experiments consisted of the following process: 1) remote oxygen plasma cleaning of *n*-type Si substrate followed by a 5min 500°C annealing, 2) XPS and UPS characterization, 3) deposition of ~1.5 nm of hafnium oxide, 4) XPS and UPS characterization, 5) deposition of ~2.0 nm vanadium oxide, 6) XPS and UPS characterization, 7) deposition of ~1.5 nm of hafnium oxide, 8) XPS and UPS characterization. The results of XPS and UPS spectra of

each step are shown in Figs. 6.1- 6.4. The XPS observation "windows" were set for the Si 2p, Hf 4f, O 1s and V 2p core levels. The carbon XPS peaks were below the detection limit before and after deposition.

6.4.1 Si substrate with native oxide layer

The Si 2p core level is shown in Fig. 6.1. The initial SiO_2 layer thickness can be determined from the ratio of the bulk (~99 eV) and SiO_2 (~104 eV) Si peaks. The SiO_2 thickness was determined using the following equation [13]: $t_{ox} = \lambda_{SiO2} \ln \{[(1/\beta) (I_{SiO2}^{exp}/ I_{Si}^{exp})] + 1\}$, where λ_{SiO2} is the attenuation length of the Si 2p photoelectrons in SiO_2, $\beta = (I_{SiO2}^{\infty}/ I_{Si}^{\infty})$ is the ratio of the Si 2p intensity from thick SiO_2 and a Si wafer, and $I_{SiO2}^{exp}/ I_{Si}^{exp}$ is the measured ratio of normal incident XPS Si 2p intensities. For our XPS instrument configuration, the analyzer is normal to the sample. We take λ_{SiO2} to be 2.8±0.02 nm, an average from five references [14-18], and β to be 0.83[18]. With these values and the measured intensities ratio, the thickness of the initial SiO_2 layer on the Si wafer is determined to be 0.8 ± 0.1 nm.

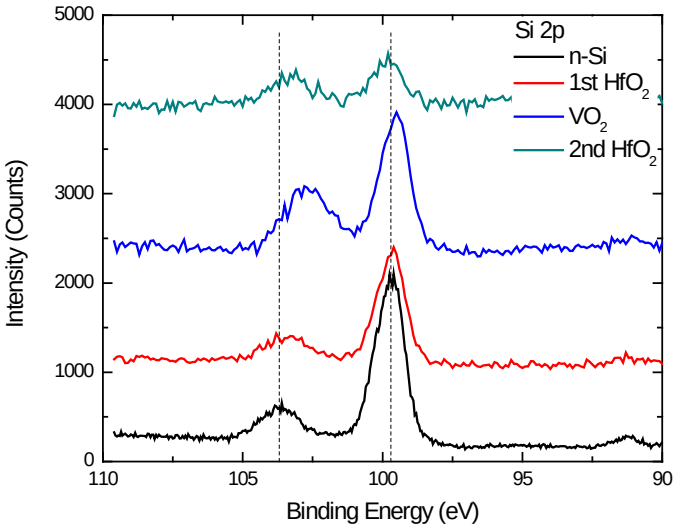

Figure 6.1 X-ray photoemission spectra of Si 2p peaks for (a) plasma oxidized *n*-type Si(100) sample. The curves are for the oxidized Si substrate, after deposition of the first HfO_2 layer on Si, after deposition of VO_2 interlayer and after deposition of second HfO_2 layer.

The XPS binding energies of the Si 2p, O 1s, V 2p3/2 and Hf 4f 7/2 are summarized in Table 6.1. The initial Si 2p peaks are at 99.7 and 103.7 eV, respectively, corresponding to bulk Si near the surface and the SiO_2 layer of the oxidized Si. Results have established that the Si 2p core level is 98.8eV below the valence band maximum (VBM) [19]. For the heavily doped *n*-type Si wafer, the Fermi level is at 0.9-1.0eV above the VBM. Therefore, the initial *n*-type Si substrate displays a flat band condition as the Si 2p peak is at 99.7 eV (98.8 + 0.9 eV). After first 1.5 nm HfO_2 layer deposition, the Si bulk and SiO_2 related 2p peaks shift to lower binding energies of 99.6 and 103.5, respectively. After 2.0

nmVO_2 layer deposition, the Si bulk and SiO_2 related peaks are shifted to lower binding energies of 99.5 and 102.8 eV, respectively. After second 1.5 nm HfO_2 layer deposition, the Si peaks shift back to 99.7 and 103.4 eV, respectively. The shifts in the Si bulk feature are attributed to a change of the band bending in the Si substrate, and the differential shifts between the Si substrate and Si oxide features are attributed to an electric potential across the SiO_2 layer.

Table 6.1. XPS of Si 2p (Si and SiO_2), O 1s, V 2p 3/2, Hf 4f 7/2 core levels, and valence band maximum (VBM) relative to the Fermi level, in eV, for HfO_2/VO_2//HfO_2/oxidized *n*-type Si(100). Values have an uncertainty of ± 0.1 eV.

	Si 2p (eV)		O 1s (eV)	V 2p3/2 (eV)	Hf 4f7/2 (eV)	VBM (eV)
Process	Si bulk	SiO_2	Main			
Substrate	99.7	103.7	532.6	/	/	5.5
1.5nm HfO_2	99.6	103.5	531.2	/	18.3	4.5
2.0nm VO_2	99.5	102.8	530.2	515.5	17.2	0.8
1.5nm HfO_2	99.7	103.4	531.0	/	18.0	4.2

6.4.2 HfO_2 layers

Two HfO_2 layers were deposited on the sample with 1.5 nm thick for each layer. The first layer was deposited directly on the *n*-type Si substrate with native oxide. The second layer was deposited on the top of the VO_2 interlayer. Fig. 6.2 presents the Hf XPS 4f peaks as evidence of the HfO_2 layers. For the first 1.5 nm

HfO_2 layer on *n*-type Si, the Hf 4f 7/2 peak is located at 18.3 eV. As the VO_2 interlayer was deposited, the Hf 4f 7/2 peakis located at 17.2 eV. When the second 1.5 nm HfO_2 layer was deposited on top of the VO_2 interlayer, the Hf 4f 7/2 peak is located at 17.9 eV.

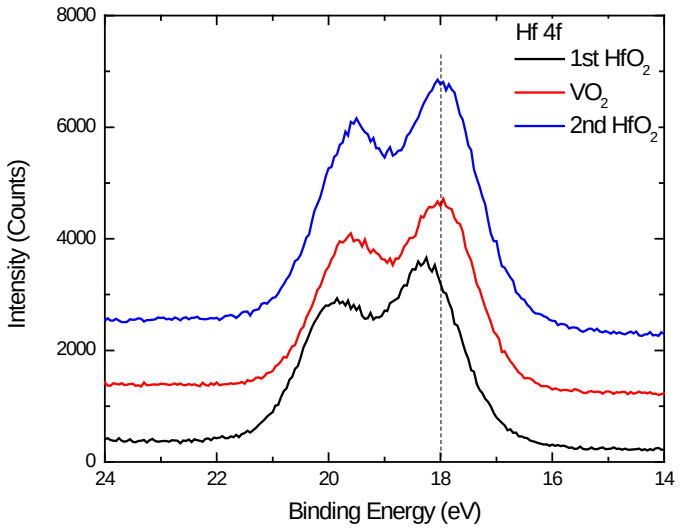

Figure 6.2 X-ray photoemission spectra of Hf 4f peaks for the deposition of the first HfO_2 layer on Si, after deposition of VO_2 interlayer and after deposition of second HfO_2 layer.

6.4.3 2.0 nm VO_2 layer

A 2.0 nm thick VO_2 interlayer was deposited between two HfO_2 layers. The O 1s and V 2p core levels are shown in Fig. 6.3. The peak around 530~533 eV is the O 1s peak. The signal of this O 1s peak is contributed by the all the oxides on the top of sample. However, the Main peak position is mostly contributed by the top oxide layer at the each step of growth. For the Si substrate, the peak at 532.6 eV is the O 1s signal of the oxygen in the SiO_2 layer. After the

first HfO_2 layer, the O 1s peak at 531.2 eV is mostly due to oxygen in the HfO_2. After VO_2 deposition, the peak at 530.2 eV is attributed to the O 1s signal corresponding to the VO_2 layer. After the second HfO_2 capping layer, the O 1s peak at 531.0 is mostly due to oxygen in the second HfO_2 layer. After the initial 2.0nm VO_2 deposition, the V 2p3/2 peak is located at 515.5 eV. After the HfO_2 deposition, the V 2p3/2 peak is broadened in the range of 513~515 eV, which may be due to the extraction of oxygen from the VO_2 layer during HfO_2 deposition. The V 2p3/2 peak at 513.4 eV may be due to other vanadium oxides [20] or vanadium-hafnium interface oxides. The peaks at 522 eV are the satellite peaks of O 1s, which are due to the satellite lines of non-monochromatic Mg X-ray source.

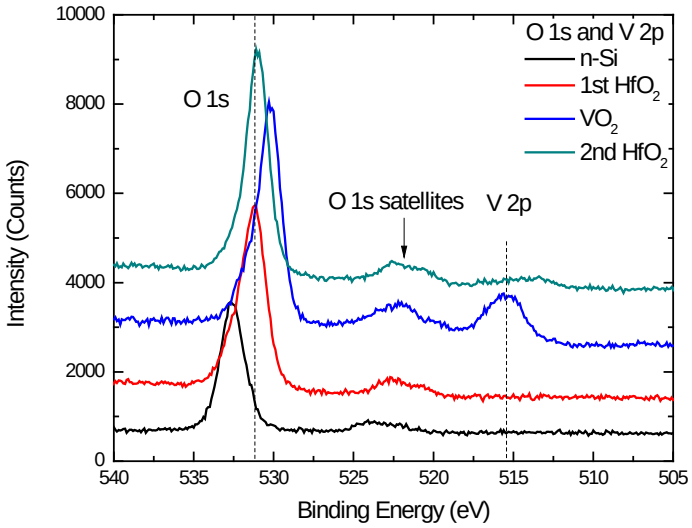

Figure 6.3 X-ray photoemission spectra of O 1s and V 2p peaks for the oxidized Si substrate, after deposition of the first HfO_2 layer on Si, after deposition of VO_2 interlayer and after deposition of second HfO_2 layer.

6.4.4 Ultraviolet photoemission spectra

The ultraviolet photoemission spectra of the cleaned, oxidized substrate, after first layer of HfO_2 deposition, after VO_2 deposition, and after second layer of HfO_2 deposition are shown in Fig. 6.4. The UPS spectrum of the initial clean SiO_2 layer on n-type Si substrates shows the valence band maximum (VBM) at 5.5 eV below the Fermi level. The valence band offset between Si and SiO_2 is then 4.5 eV for the n-type Si substrate, which agrees with previous results for the Si-SiO_2 band offset [21]. This result is consistent with a low interface state density and negligible band bending for the Si substrate. After the first 1.5 nm HfO_2 layer deposition, the front cutoff of the UPS spectrum indicates the valence band maximum relative to the Fermi level at 4.5 eV. For the VO_2 film, the V 3d peak is close to the Fermi level, and the cutoff of this peak gives the valence band maximum at 0.8 eV below the Fermi level. After the second 1.5 nm HfO_2 layer deposition, the front cutoff of the UPS spectrum indicates the valence band maximum relative to the Fermi level at 4.2 eV.

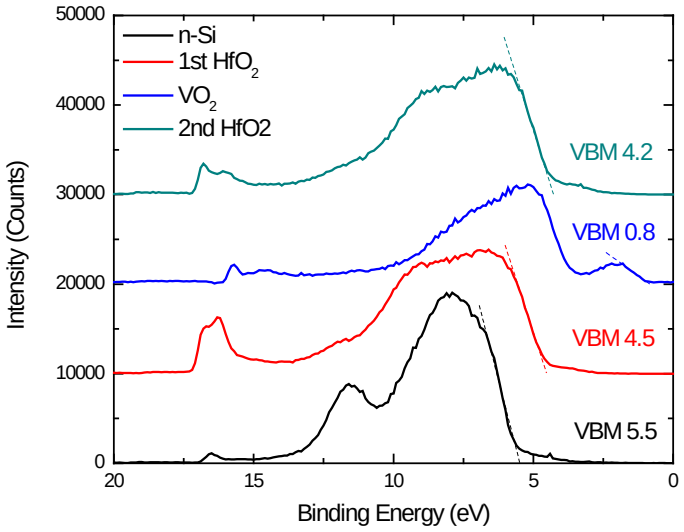

Figure 6.4 Ultraviolet photoemission spectra of the oxidized Si substrate, the first as-deposited HfO_2 layer on Si, after deposition of VO_2 interlayer and after deposition of second HfO_2 layer.

6.5 Discussion

Figure 6.5 shows diagrams of the band alignment for the stacked structure during processing. As shown in the Fig It is noted that the CBM for all of the oxides are deduced from the reported values of the band gap, and the CBM are shown as dashed lines in the figures. The initial cleaned oxidized Si substrate displays a flat band condition, shown in Fig. 6.5(a). After first 1.5 nm HfO_2 deposition, the SiO_2 band is tilted upwards, shown in Fig. 6.5(b). It is presumed that there is no significant electric field across the HfO_2 layer. The valence band offset between HfO_2 and SiO_2 can be determined using the following expression:

$$VBO= (E_{4f7/2}^{HfO2} - E_{VBM}^{HfO2}) - (E_{2p}^{SiO2} - E_{VBM}^{SiO2}) - \Delta1(E_{4f7/2}^{HfO2} - E_{2p}^{SiO2}) - \Delta2(SiO_2), \quad (6.1)$$

where ($E_{4f7/2}^{HfO2}$ – E_{VBM}^{HfO2}) is the Hf 4f7/2 core level to the VBM of HfO_2, (E_{2p}^{SiO2} – E_{VBM}^{SiO2}) is the Si 2p core level to the VBM of SiO_2, $\Delta 1(E_{4f7/2}^{HfO2}$ – $E_{2p}^{SiO2})$ is the energy separation between the Hf 4f7/2 of HfO_2 and Si 2p of SiO_2, and $\Delta 2(SiO_2)$ is the half value of the electrical potential across the SiO_2 layer. Based on the Si 2p peak of SiO_2 shift of ~ 0.2 eV and the substrate Si 2p peak shift of ~ 0.1eV, the electrical potential across the SiO_2 layer can be calculated as 0.2 (2 × (0.2 – 0.1)) eV. From Table 1, the VBO of HfO_2 and SiO_2 is calculated as 0.7 eV.

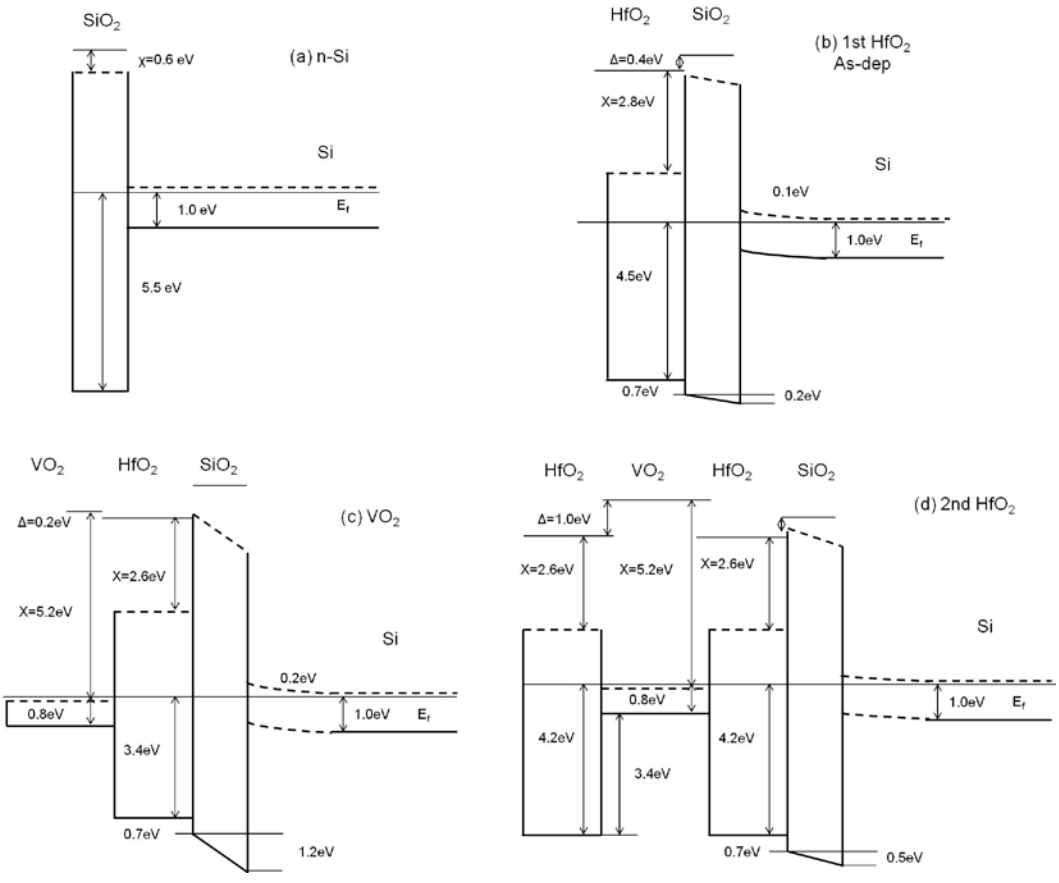

Figure 6.5 Band alignment of the oxidized Si substrate, after deposition of the first HfO_2 layer on Si, after deposition of VO_2 interlayer and after deposition of

second HfO_2 layer. Dashed lines are used to represent the conduction band minimum of the oxides which are deduced from reported values of the band gap. Distances approximately represent the experimental film thickness except the depletion region in the Si which is compressed as indicated.

After VO_2 layer deposition, the Si 2p and Hf 4f 7/2 peaks shift to lower binding energy, indicating an electric potential across the SiO_2 layer and band bending in the Si substrate, shown in Fig. 6.5(c). After second HfO_2 layer deposition, the Si 2p and Hf 4f 7/2 peak shifts approaching to the band condition of initial HfO_2 layer deposition, shown in Fig. 6.5(d).The valence band offset of HfO_2/VO_2 can be deduce from the band alignment schematics, which is 3.4 eV. This result is consistent with our previous study [22]. However, in the Fig. 6.5(c), the band offset of VO_2/HfO_2 shows around 2.6 eV. This difference may be due to the processing sequence. We suggest that the VO_2/HfO_2 interface after the high temperature growth of the VO_2 layer on the first layer HfO_2 may be different than the HfO_2/VO_2 interface after the room temperature growth of the second HfO_2 layer. During high temperature deposition of the VO_2 layer, a fraction of the oxygen in first HfO_2 layer may be extracted into VO_2 film. When the second HfO_2 layer was deposited on the VO_2 layer at room temperature, the oxygen may diffuse back the first HfO_2 layer and compensate the oxygen deficiency of that layer.

For most heterostructures, interface bonding leads to charge transfer and an interface dipole. The interfacial dipole is often described as the difference

between the vacuum levels at the interface of the two adjoining materials. Experimentally this can be determined from the photoemission results using:

$$\Delta Dipole = (h\nu - W^a) - (h\nu - W^b) - VBO^{a/b} = W^b - W^a - VBO^{a/b}, \quad (6.2)$$

For dielectric interfaces a model has been developed by Robertson and Mönch which presumes that the charge will transfer to align the charge neutrality levels (CNL) at the interface. [23,24] The CNLs of HfO_2 and SiO_2 are calculated as 3.7 eV [23] and 4.5 eV [25] respectively. Thus, the predicted value of band offset between HfO2 and SiO2 is 0.8 eV, which is very similar to our measured value 0.7 eV. It indicates the CNL model can describe this system.

6.6 Conclusions

A quantum well structure has been prepared with an ultra thin VO_2 layer between 2 layers of HfO_2 on oxidized Si substrates. The films were developed by reactive e-beam deposition on oxidized *n*-type Si substrates. The band alignment for this gate stack structure was deduced from *in-situ* XPS and UPS spectra. A band offset of 0.7 ± 0.1 eV was measured between the 1.5 nm HfO_2 layer and the SiO_2 layer, which is comparable to the value predicted by CNL model. After the VO_2 interlayer and the HfO_2 capping layer deposition, the band offset between the HfO_2 and VO_2 is 3.4 ± 0.1 eV. The band diagram for this quantum well structure shows a confined-well band structure, demonstrating the potential for charge storage for the embedded VO_2 layer.

REFERRENCES

[1] C. N. Berglund and H.J. Guggenheim, Phys. Rev. 185, 1022-1033 (1969).

[2] F.J. Morin, Phys. Rev. Lett. 3, 34-36 (1959).

[3] K. Nagashima, T. Yanagida, H. Tanaka, and T. Kawai, J. Appl. Phys. 101, Art Number 026103-3 (2007)

[4] H-T. Kim, B.-G Chae, D.-H. Youn, G. Kim, and K.-Y. Kang, Appl. Phys. Lett. 86, 242101-3 (2005).

[5] H-T. Kim, Y.-W. Lee, B.-J. Kim B.-G Chae, S.-J. Yun, K.-Y. Kang, K.-J. Han K.-J. Yee, and Y.-S. Lim, Phys. Rev. Lett. 97, 266401-4 (2006).

[6] C. Ko and S. Ramanathan, Appl. Phys. Lett. 93, Art Number 252101-3(2008)

[7] G. Stefanovich, A. Pergament, D. Stefanovich, J. Phys.: Condens. Matter 12, 8837-45 (2000).

[8] G. Gopalakrishnan, D. Ruzmetov, S. Ramanathan, J. Mater. Sci. 44, 5345-53 (2009).

[9] S. Hormoz, S. Ramanathan, Solid-State Electronics 54, 654-659 (2010).

[10] A.L. Pergament, P.P. Boriskov, A.A. Velichko, N.A. Kuldin, J. Phys. Chem. Solids 71, 874-879(2010).

[11] G.D. Wilk, R.M. Wallace, J.M. Anthony, J. Appl. Phys, 89, 5243 (2001).

[12] T. Yasuda, Y. Ma, S. Habermehl, and G. Lucovsky, J. Vac. Sci. Technol. B 10, 1844 (1992).

[13] D.A. Cole, J.R. Shallenberger, S.W. Novak, R.L. Moore, M.J. Edgell, S.P. Smith, C.J. Hitzman, J.F. Kirchhoff, E. Principe, W. Nieveen, F.K. Huang, S.Biswas, and K. Jones, J. Vac. Sci. Technol. B 18, 440-444 (2000).

[14] D. Rob and M. Maier, Fresenius J. Anal. Chem. 333, 488 (1989).

[15] M. F. Hochella and A. F. Carim, Surf. Sci. Lett. 197, L260 (1988).

[16] F. Yano, A. Hiraoka, T. Itoga, H. Kojima, K. Kanehori, and Y. Mitsui, J. Vac. Sci. Technol. A 13, 2671 (1995).

[17] Z.H. Lu, J.P. McCaffrey, B. Brar, G.D. Wilk, R.M. Wallace, L.C. Feldman, and S.P. Tay, Appl. Phys. Lett. 71, 2764 (1997).

[18] J. R. Shallenberger, D. A. Cole and S. W. Novak, J. Vac. Sci. Technol. A 17, 1086 (1999).

[29] C.C. Fulton, G. Lucovsky, and R.J. Nemanich, J. Vac. Sci. Technol. B20, 1726 (2002).

[20] J. Mendialdua, R.Casanova, and Y. Barbaux, J. Electron Spectrosc. Relat. Phenom. 71, 249 (1995).

[21] J.W. Keister, J.E. Rowe, J.J. Kolodziej, H. Niimi, T.E. Madey, and G.Lucovsky, J. Vac. Sci. Technol. A 17, 1250 (1999).

[22] C-Y. Zhu, M. Kaur, F. Tang, X. Liu, D.J. Smith and R.J. Nemanich, submitted to J. Appl. Phys.

[23] J. Robertson, J. Vac. Sci. Technol. B 18, 1785 (2000).

[24] W. Mönch, J. Appl. Phys. 109, 113724 (2011).

[25] J. Robertson and B. Falabretti, J. Appl. Phys. 100, 014111, (2006).

Chapter 7

SUMMARY AND FUTURE WORK

7.1 Summary

The research described in this dissertation has involved the following topics: a) Thin oxide film growth by plasma enhanced atomic layer deposition (PEALD) and molecular beam deposition (MBD). High dielectric constant materials HfO_2 and La_2O_3 which were grown as the dielectrics in a gate stack structure. Conducting oxide materials VO_2 and ZnO which were grown as the conducting layer in a gate stack structure. b) Characterization of gate stack structures with X-ray photoelectron spectroscopy (XPS) and ultraviolet photoelectron spectroscopy (UPS), and interfacial charge distribution was discussed based on the analysis of XPS and UPS spectra. Band alignment schematics are developed for these gate stack structures, and two band alignment models for semiconductor heterostructures, based on the electron affinity (EA) model and the charge neutrality level (CNL) model were discussed for these gate stack structures.

A gate stack structure was prepared with a HfO_2 capping layer and an ultra thin VO_2 interlayer on oxidized Si substrates. The 2nm thick films were grown by oxide molecular bean deposition on oxidized *n*- and *p*-type substrates. The TEM analysis confirmed the layer structure and indicated sharp interfaces without evidence of interdiffusion. The band alignment for this gate stack structure was deduced from *in-situ* XPS and UPS spectra. The valence band offset between an ultra thin VO_2 layer and the SiO_2 layer is measured to be 4.0 ± 0.1 eV. After the

HfO_2 capping layer deposition, only small changes in the band alignment are observed. The valence band offset between the HfO_2 and VO_2 is measured to be 3.4 ± 0.1 eV. According to the CNL model, the valence band offset of HfO_2/SiO_2 is expected to be 0.8 eV without a VO_2 interlayer. The relative band offset between the HfO_2 and SiO_2 with a VO_2 interlayer is 0.7 ± 0.1 eV which is comparable to the predicted value without a VO_2 inter-layer. This result shows the CNL model can describe the structure. The results also show charge transfer to the VO_2 during growth on the *n*-type substrate. The band diagram for this gate stack structure shows a confined-well band structure, demonstrating the potential for charge storage for the embedded VO_2 layer.

For the dielectric layer, we also expand pure Hf oxide to pure La oxide which is another popular high-k material. In the chapter 4, three high-k material, pure Hf oxide, pure La oxide, and alloyed Hf-La oxide films were developed by using remote-plasma atomic layer deposition (RPALD). The growth conditions were investigated at growth temperatures ranging from ~80°C to ~250 °C and different alloy composition. The relative composition and atomic bonding structures of the film were determined by *in-situ* X-ray photoelectron spectroscopy (XPS). Atomic force microscopy (AFM) and transmission electron microscopy (TEM) were implemented to characterize the morphology and crystalline structure.

For low temperature Hf oxide growth, The XPS results indicated a significant amount of excess oxygen species was observed in the deposited film. These excess oxygen species may be induced by the oxygen plasma processing

during growth. We established that a He plasma post deposition treatment can partially remove the excess oxygen. In addition, the pure Hf oxide films show a surface morphology with protruding islands over a smooth surface which reflects the crystallized nature of the Hf oxide domains. In order to suppress the crystallization of the Hf oxide and carbon contamination of the La oxide, the Hf-La oxide film was grown by PEALD. XPS, TEM and AFM results indicated that the Hf-La oxide films showed an amorphous or disordered structure with no evidence of nanocrystalline domains. Carbon residue in the alloyed film is also reduced compared with that of the La oxide film. Finally, the electrical properties of the deposited films were characterized by capacitance-voltage (C-V) and current-voltage (I-V) measurement. The I-V curves show that the alloyed Hf-La oxide films have a higher break down field than that of pure Hf oxide films.

With the achievement of high quality high-k dielectrics (HfO_2-La_2O_3), the research was extended to new channel layer materials. ZnO was considered as a channel layer material and integrated into a gate stack structure with an alloyed HfO_2-La_2O_3 (11% HfO_2 and 89% La_2O_3) layer. These thin films were prepared by plasma enhanced atomic layer deposition (PEALD). High resolution electron microscopy indicated an amorphous structure of the deposited layers. The electronic properties were characterized with *in-situ* x-ray and ultraviolet photoemission spectroscopy. A significant amount of excess oxygen was also observed in the as-deposited ZnO and (HfO_2-La_2O_3) layers. A helium plasma post-deposition treatment can partially remove the excess oxygen in both layers. Furthermore, the band alignment of this structure was established for an *n*-type Si

substrate. A valence band offset of 1.5 ± 0.1 eV was measured between a thin ZnO layer and a SiO_2 layer. The valence band offset between HfO_2-La_2O_3 and ZnO was almost negligible. The band relationship developed from these results demonstrates confinement of electrons in the ZnO film as a channel layer for thin film transistors.

The studies of the gate stack structure of HfO_2/VO_2 on Si substrate, employed a modified multilayer structure. This confined well structure was prepared with an ultra thin VO_2 layer between two HfO_2 layers on oxidized Si substrates. The films were developed by reactive e-beam deposition on oxidized *n*-type Si substrates. The band alignment for this gate stack structure was deduced from *in-situ* XPS and UPS spectra. A band offset of 0.7 ± 0.1 eV was measured between the 1.5 nm HfO_2 layer and the SiO_2 layer, which is comparable to the value predicted by the CNL model. After the VO_2 interlayer and the HfO_2 capping layer deposition, the band offset between the HfO_2 and VO_2 is 3.4 ± 0.1 eV, which is consistent with previous results discussed in chapter 3. The band diagram for this confined well structure shows both electrons and holes can be confined in the VO_2 layer. The results demonstrate this confined well structure has potential for applications for charge storage in the embedded VO_2 layer.

7.2 Future work

7.2.1 Alloyed HfO_2-SiO_2 dielectrics

Currently, HfO_2 is one of the most studied among the high-k material candidates. However, one problem for pure HfO_2 is the formation of nanocrystalline domains, which results in a high leakage current. This problem

can be mitigated by alloying HfO_2 with other oxides. In our previous study, we reported that HfO_2 alloyed with La_2O_3 is an approach to address this problem. [1] This alloyed hafnium lanthanum oxide has an amorphous structure without obvious crystallized grains. I-V measurements show that this uniform amorphous alloyed oxide film has a lower leakage current than that of a pure hafnium oxide film. However, La_2O_3 can absorb water and carbon dioxide when exposed to air, which leads to the formation of LaO(OH) and carbonate features. [2, 3] An alternate approach is to prepare HfO_2 alloyed with SiO_2 for the gate dielectric insulator, [4, 5] as SiO_2 does not readily absorb water and CO_2. This structure is more compatible with current semiconductor technology. Besides maintaining a low leakage current, it is also required that the transistor gate dielectric insulator exhibits a band alignment that can block both holes and electrons. This requires a wide band gap of material, and HfO_2 has a band gap of 5.7 eV and SiO_2 has a band gap of 8.9 eV. Both materials are suitable candidates for this band alignment requirement. The film also exhibits a low density of electronically active defects (bulk and interface), and the interface is stable for the required thermal process. The first part of this proposed project is to employ plasma enhanced ALD to achieve a high quality HfO_2-SiO_2 dielectrics for TFTs.

7.2.2 Alumina Zinc oxide and vanadium oxide for thin film transistor

The interest in future flexible displays based on and transparent thin film transistor (TFT) has significantly increased. However, traditional TFT's based on amorphous silicon (a-Si) as the active channel layer material has several limitations including a low mobility below 1.0 cm^2/Vs [6]. Recently, transparent

semiconductor materials such as zinc oxide have been proposed as a channel layer material as an alternative to a-Si. ZnO is a wide band gap semiconductor material. At room temperature, crystalline ZnO has a mobility of ~100 cm^2/Vs [7] which is much higher than that of a-Si. In addition, zinc oxide thin films can be successfully grown even at a temperature of 100 °C and below [8]. In our previous study, ZnO films were grown by PEALD and integrated into gate stack structure. Recently, aluminum doped ZnO (AZO) has been considered as a new conducting transparent oxide, which has the potential to replace ITO in some applications. The resistivity of AZO can be below 10^{-3} Ω*cm [9-11], which is lower than that of undoped ZnO 10^5Ω*cm [10]. Another metal-like oxide is vanadium dioxide (VO_2). Vanadium dioxide (VO_2) is a narrow band gap material (Eg = 0.7eV) [12], with a well known Metal to Insulator Transition (MIT). At room temperature, VO_2 shows insulating characteristics. When VO_2 is heated above ~70°C (343K), the insulator to metal transition occurs, [12, 13] with an abrupt three order of magnitude change of resistivity. Recently, research has indicated that the MIT can be achieved by applying an external electric field at a constant temperature. [14-18] We propose that we can control the current passing through this VO_2 channel layer by applying a gate voltage.

REFERRENCES

[1] Fu Tang, Chiyu Zhu, David J. Smith, and Robert J. Nemanich, J. Vac. Sci. Technol. A, Vol. 30, No. 1, (2012).

[2] A.M. De Asha, J.T.S. Critchley, R.M. Nix, Surface Science 405, 201–214, (1998).

[3] M. Suzuki, M.Kagawa, Y. Syono and T. Hirai, J. Cryst. Growth, 112, 621-627 (1991).

[4] Yoshihide Senzaki, Seung Park, Hood Chatham, and Lawrence Bartholomew, Wesley Nieveen, J. Vac. Sci. Technol. A 22(4), (2004).

[5] Mohammad Shahariar Akbar, S. Gopalan, H.-J. Cho, K. Onishi, R. Choi, R. Nieh, C. S. Kang, Y. H. Kim, J. Han, S. Krishnan, and Jack C. Lee, Appl. Phys. Lett., Vol. 82, No. 11, (2003).

[6] K. Nomura, H. Ohta, A. Takagi, T. Kamiya, M. Hirano, and H. Hosono, Nature 432, 488 (2004).

[7] E. Guziewicz, M. Godlewski, T. Krajewski, Ł. Wachnicki, A. Szczepanik, K. Kopalko, A. Wójcik-Głodowska, E. Przeździecka, W. Paszkowicz, E. Łusakowska, P. Kruszewski, N. Huby, G. Tallarida, and S. Ferrari, J. Appl. Phys. 105, 122413 (2009).

[8] A. Wójcik, M. Godlewski, E. Guziewicz, R. Minikayev, and W. Paszkowicz, J. Cryst. Growth 310, 284 (2008).

[9] O. Bamiduro, H. Mustafa, R. Mundle, R. B. Konda, and A. K. Pradhan, Appl. Phys. Lett. 90, 252108 (2007).

[10] Yumin Kim, Woojin Lee, Dae-Ryong Jung, Jongmin Kim, Seunghoon Nam, Hoechang Kim, and Byungwoo Park, Appl. Phys. Lett. 96, 171902 (2010).

[11] Tadatsugu Minami, Semicond. Sci. Technol. 20 S35–S44 (2005).

[12] C.N. Berglund and H.J. Guggenheim, Phys. Rev. 185, 1022 (1969).

[13] F.J. Morin, Phys. Rev. Lett. 3, 34-36 (1959).

[14] H-T. Kim, B.-G Chae, D.-H. Youn, G. Kim, and K.-Y. Kang, Appl. Phys. Lett. 86, 242101-3 (2005).

[15] H-T. Kim, Y.-W. Lee, B.-J. Kim B.-G Chae, S.-J. Yun, K.-Y. Kang, K.-J. Han K.-J. Yee, and Y.-S. Lim, Phys. Rev. Lett. 97, 266401-4 (2006).

[16] C. Ko and S. Ramanathan, Appl. Phys. Lett. 93, Art Number 252101-3 (2008).

[17] G. Stefanovich, A. Pergament, D. Stefanovich, J. Phys.: Condens. Matter, 12, 8837-45 (2000).

[18] G. Gopalakrishnan, D. Ruzmetov, S. Ramanathan, J. Mater. Sci. 44, 5345-53 (2009).

[19] S. Hormoz, S. Ramanathan, Solid-State Electronics, 54, 654-659 (2010).

[20] A.L. Pergament, P.P. Boriskov, A.A. Velichko, N.A. Kuldin, J. Phys. Chem. Solids 71, 874-879 (2010).

REFERENCES

A.M. De Asha, *et al.*, Surface Science 405, 201–214 (1998).

O. Bamiduro, *et al.*, Appl. Phys. Lett. 90, 252108 (2007).

J. Bardeen, Phys.Rev. 71, 717 (1947).

L. Belau, *et al.*, J. Vac. Sci. Technol. B 26, 2225 (2008).

C.N. Berglund, *et al.*, Phys. Rev. 185, 1022 (1969).

S. Biermann, *et al.*, Phys. Rev. Lett. 94, 026404 (2005).

P. F. Carcia, *et al.*, Appl. Phys. Lett. 88, 123509 (2006).

A. Cavelleri, *et a,*. Phys. Rev. Lett. 87, 237402 (2001).

J. P. Chang, *et al.*, Appl. Phys. Lett., Vol. 79, No. 23, 3 December (2001).

Jin-Bo Chengb, *et al.*, Applied Surface Science 233 91–98 (2004).

S. Choi, *et al.*, J. Korean Phys. Soc. 44, 35 (2004).

D.A. Cole, *et al.*, J. Vac. Sci. Technol. B 18, 440-444 (2000).

M. Copel, *et al.*, Appl. Phys. Lett. 76, 436 (2000).

C. B. Drake. J. Vac. Sci. Tech. 13, 761 (1976).

C. Driemeier, *et al.*, J. Appl. Phys. 102, 024112 (2007).

C. C. Fulton, *et al.*, J. Vac. Sci. Technol. B20, 1726 (2002).

C. C. Fulton, *et al.*. Appl. Phys. 99, 063708 (2006).

S. M, George, *et al.*, J. W. J. Phys. Chem., 100, 13121 (1996).

G. Gopalakrishnan, *et al.*, J. Mater. Sci. 44, 5345-53 (2009).

E. Guziewicz, *et al.*, J. Appl. Phys. 103, 033515 (2008).

E. Guziewicz, *et al.*, J. Appl. Phys. 105, 122413 (2009).

D. M. Hausmann, *et al.*, J. Cryst. Growth 249, 251 (2003).

M.W. Haverkort, *et al.*, Phys. Rev. Lett. 95, 196404 (2005).

W. He, *et al.*, J. Electrochem. Soc. 155, G189 (2008).

V. Heine, Phys. Rev. 138A, 1689 (1965).

S. B. S. Heil, *et al.*, Appl. Phys. Lett., 89, 131505 (2006).

M. F. Hochella, *et al.*, Surf. Sci. Lett. 197, L260 (1988).

S. Hormoz, *et al.*, Solid-State Electronics, 54, 654-659 (2010).

Y. Kawamura, *et al.*, Jpn. J. Appl. Phys. 50, 04DF05 (2011).

Y. Kawamura, *et al.*, Jpn. J. Appl. Phys. 51, 02BF04 (2012).

J.W. Keister, *et al.*, J. Vac. Sci. Technol. A 17, 1250 (1999).

S. Keun Kim, *et al.*, Thin Solid Films 478, 103 (2005).

H-T. Kim, *et al.*, Appl. Phys. Lett. 86, 242101-3 (2005).

H-T. Kim, *et al.*, Phys. Rev. Lett. 97, 266401-4 (2006).

S. Keun Kim, *et al.*, Thin Solid Films 478, 103 (2005).

Yumin Kim, *et al.*, Appl. Phys. Lett. 96, 171902 (2010).

H. Kind, *et al.*, Adv. Mater. 14, 158 (2002).

A. I. Kingon, *et al.*, Nature 406, 1032 (2000).

C. Ko, *et al.*, Appl. Phys. Lett. 93, Art Number 252101-3 (2008).

Koji Kousge, J. Phys. Chem. Solids Pergamon Press, 28, 1613-1621 (1967).

K. Kukli, *et al.*, Chem. Vap. Deposition, 12, 158–164 (2006).

E. Langereis, *et al.*. Appl. Phys. Lett., 89, 081915 (2006).

B. H. Lee, *et al.*, Org. Electron. 9, 1146 (2008).

S. Lee, *et al.*, Phys. Status Solidi A-Appl. Mat. 207, 1845 (2010).

M. Leskela, *et al.*, Thin Solid Films 409, 138 (2002).

J. W. Lim, *et al.*, Electrochem. Solid-State Lett., 7, F45 (2004).

S. J. Lim, *et al.*, Thin Solid Films, 516, 1523 (2008).

Y.S. Lin, *et al.*, Appl. Phys. Lett., Vol. 81, No. 11, 9 September (2002).

R. Lopez, *et al.*, Appl. Phys. Lett. 79, 3161 (2001).

Z.H. Lu, *et al.*, Appl. Phys. Lett. 71, 2764 (1997).

Vesa Lujala, *et al.*, Appl. Surf. Sci. 82/38, 34 (1994).

A. Mang, *et al.*, Solid State Commun. 94, 251 (1995).

J. Mendialdua, *et al.*, J. Electron Spectrosc. Relat. Phenom. 71, 249 (1995).

Tadatsugu Minami, Semicond. Sci. Technol. 20 S35–S44 (2005).

W. Mönch, Phys. Rev. Lett. 58, 1260 (1986).

W. Mönch, J. Appl. Phys. 80, 5076 (1996).

W. Mönch, Appl. Phys. Lett. 86, 162101 (2005).

W. Mönch, J. Appl. Phys. 109, 113724 (2011).

Gorden E. Moore, Electronics, Vol. 38, No. 8, April 19, (1965).

F.J. Morin, Phys. Rev. Lett. 3, 34 (1959).

K. Nagashima, *et al.*, J. Appl. Phys. 101, Art Number 026103-3 (2007).

G.S. Nadkarni, *et al.*, Thin Solid Films, 105, 115-129 (1983).

G. Neumann, Curr. Top. Mater. Sci. 7, 143 (1981).

M. Nieminen, *et al.*, Appl. Surf. Sci. 174, 155 (2001).

K. Nomura, *et al.*, Nature 432, 488 (2004).

S. Ormoz, *et al.*, Solid State Electronics 54, 654-659 (2010).

J. S. Park, *et al.*, J. Electrochem. Soc. 149, C28 (2002).

P. K. Park, *et al.*, Electrochem. Solid State Lett. 9, F34 (2006).

S. H. Ko Park, *et al.*, Electrochem. Solid-State Lett. 9, G299 (2006).

A.L. Pergament, *et al.*, J. Phys. Chem. Solids 71, 874-879(2010).

M. Ritala, *et al.*. Thin Solid Films, 225, 288 (1993).

D. Rob, *et al.*, Fresenius J. Anal. Chem. 333, 488 (1989).

J. Robertson, J. Vac. Sci. Technol. B, 18, 1785 (2000).

J. Robertson, Eur. Phys. J. Appl. Phys. 28, 265 (2004).

J. Robertson, Rep. Prog. Phys. 69, 327–396 (2006).

J. Robertson, *et al.*, J. Appl. Phys. 100, 014111, (2006).

P.C. Rowlette, *et al.*, Chem. Vap. Deposition, 15, 15–20 (2009).

K.G. Saw, *et al.*, Thin Solid Films 515, 2879 (2007).

S. Sayan, *et al.*, Appl. Phys. Lett. 80, 2135 (2002).

Yoshihide Senzaki, *et al.*, J. Vac. Sci. Technol. A 22(4), (2004).

Mohammad Shahariar Akbar, *et al.*, Appl. Phys. Lett., Vol. 82, No. 11, (2003).

J. R. Shallenberger, *et al.*, J. Vac. Sci. Technol. A 17, 1086 (1999).

A. J. Signorel, *et al.*, Phys. Rev. B8, 81 (1973).

S. Song, *et al.*, Appl. Phys. Lett. 92, 263109 (2008).

G. Stefanovich, *et al.*, J. Phys.: Condens. Matter 12, 8837-45 (2000).

G. Stefanovich, *et al.*, J. Mater. Sci. 44, 5345-53 (2009).

T. Suntola, Thin Solid Films 216, 84 (1992).

M. Suzuki, *et al.*, J. Cryst. Growth, 112, 621 (1991).

S. T. Tan, *et al.*, J. Appl. Phys. 98, 013505 (2005).

F. Tang, *et al.*, J. Vac. Sci. Technol. A, 30, 01A147 (2012).

S. Tanuma, *et al.*, Surf. Interface Anal., 17, 911 (1991).

J. Tersoff, Phys. Rev. Lett. 52, 465 (1984).

J. Tersoff, Phys. Rev. B 30, 4874 (1984).

J. Tersoff, Phys. Rev. B 32, 6968 (1985).

R. M. Wallace, *et al.*, Crit. Rev. Solid State Mater. Sci. 28, 231 (2003).

T. Wang, *et al.*, Chem. Mat. 21, 3096 (2009).

T. Wang, *et al.*, Chem. Mat. 22, 3798 (2010).

G. D. Wilk, *et al.*, J. Appl. Phys. 89, 5243 (2001).

A. Wójcik, *et al.*, J. Cryst. Growth 310, 284 (2008).

Y. Won, *et al.*, Appl. Phys. Lett. 87, 262901 (2005).

A. Yamada, *et al.*, M. Appl. Surf. Sci., 112, 216 (1997).

F. Yano, *et al.*, J. Vac. Sci. Technol. A 13, 2671 (1995).

T. Yasuda, *et al.*, J. Vac. Sci. Technol. B 10, 1844 (1992).

Yee-Chia Yeo, *et al.*, J. Appl. Phys, 92, 7266 (2002).

E. B. Yousfi, *et al.*, Appl. Surf. Sci., 153, 223 (2000).

M. C. Zeman, *et al.*, J. Appl. Phys. 99, 023519 (2006).

C-Y. Zhu, *et al.*, submitted to J. Appl. Phys.